Aus der Klinik und Poliklinik für Radiologie
Klinikum der Ludwig-Maximilians-Universität München
Direktor: Prof. Dr. med. Jens Ricke

MRI-Based Radiation-Induced Pneumonitis Assessment in MRI-Guided Radiotherapy of Lung Tumors

Dissertation
zum Erwerb des Doktorgrades der Naturwissenschaften (Dr. rer. nat.)
an der Medizinischen Fakultät der
Ludwig–Maximilians–Universität zu München

vorgelegt von
Rabea Christina Klaar
aus
Bad Tölz

2025

Mit Genehmigung der Medizinischen Fakultät
der Ludwig-Maximilians-Universität München

Betreuer:	Prof. Dr. Guillaume Landry
Zweitgutachter:	Prof. Dr. Guido Böning
Dekan:	Prof. Dr. med. Thomas Gudermann
Tag der mündlichen Prüfung:	27. November 2025

Eidesstattliche Versicherung

Klaar, Rabea Christina

Name, Vorname

Ich erkläre hiermit an Eides statt,

dass ich die vorliegende Dissertation mit dem Titel

MRI-Based Radiation-Induced Pneumonitis Assessment in MRI-Guided Radiotherapy of Lung Tumors

selbständig verfasst, mich außer der angegebenen keiner weiteren Hilfsmittel bedient und alle Erkenntnisse, die aus dem Schrifttum ganz oder annähernd übernommen sind, als solche kenntlich gemacht habe und nach ihrer Herkunft unter Bezeichnung der Fundstelle einzeln nachgewiesen habe.

Ich erkläre des Weiteren, dass die hier vorgelegte Dissertation nicht in gleicher oder in ähnlicher Form bei einer anderen Stelle zur Erlangung eines akademischen Grades eingereicht wurde.

München, den 15. Dezember 2025	Rabea Klaar
Ort, Datum	Unterschrift

LMU LUDWIG-MAXIMILIANS-UNIVERSITÄT MÜNCHEN

Dekanat Medizinische Fakultät
Promotionsbüro

Confirmation of congruency between printed and electronic version of the doctoral thesis

Klaar, Rabea Christina

name, first name

I hereby declare that the electronic version of the submitted thesis, entitled:

MRI-Based Radiation-Induced Pneumonitis Assessment in MRI-Guided Radiotherapy of Lung Tumors

is congruent with the printed version both in content and format.

Munich, December 16, 2025 — Place, Date

Rabea Klaar — Signature doctoral candidate

Contents

List of Abbreviations

2D	**T**wo **D**imensional
3D	**T**hree **D**imensional
ART	**A**daptive **R**adio**t**herapy
AUC	**A**rea **U**nder The **C**urve
bSSFP	**B**alanced **S**teady-**S**tate **F**ree **P**recession
CT	**C**omputed **T**omography
CTCAE	**C**ommon **T**erminology **C**riteria for **A**dverse **E**vents
DIR	**D**eformable **I**mage **R**egistration
DOF	**D**egrees **o**f **F**reedom
DSC	**D**ice **S**imilarity **C**oefficient
FID	**F**ree-**I**nduction **D**ecay
FFT	**F**ast **F**ourier **T**ransform
Fx	**F**raction
GRE	**Gr**adient **E**cho
GTV	**G**ross **T**umor **V**olume
HASTE	**H**alf-Fourier **A**cquisition **S**ingle-Shot **T**urbo Spin **E**cho
HD95	**95**% **H**ausdorff **D**istance
Linac	**Lin**ear **Ac**celerator
MI	**M**utual **I**nformation
MLC	**M**ulti-**L**eaf **C**ollimator
MRI	**M**agnetic **R**esonance **I**maging
MRgRT	**M**agnetic **R**esonance Image-**G**uided **R**adio**t**herapy
MSE	**M**ean **S**quared **E**rror
NCI	**N**ational **C**ancer **I**nstitute
NMR	**N**uclear **M**agnetic **R**esonance
NSCLC	**N**on-**S**mall **C**ell **L**ung **C**ancer
NuFD	**N**on-**U**niform **F**ourier **D**ecomposition
NuFFT	**N**on-**U**niform **F**ast **F**ourier **T**ransform
OARs	**O**rgans **A**t **R**isk
PET	**P**ositron **E**mission **T**omography
PTV	**P**lanning **T**arget **V**olume
RILF	**R**adiation-**I**nduced **L**ung **F**ibrosis

RF	**R**adio**f**requency
ROC	**R**eceiver **O**perating **C**haracteristic Curve
ROI	**R**egion-**O**f-**I**nterest
RP	**R**adiation-Induced **P**neumonitis
RT	**R**adio**t**herapy
SCLC	**S**mall **C**ell **L**ung **C**ancer
SE	**S**pin **E**cho
SPECT	**S**ingle **P**hoton **E**mission **C**omputed **T**omography
TE	**E**cho **T**ime
TR	**R**epetition **T**ime
V20	**V**olume receiving more than **20** Gy

List of Publications

Original Publications

The following two original publications are subject of this cumulative dissertation in accordance with the promotion regulation for natural sciences of the Medical Faculty of Ludwig-Maximilians-University Munich.

Klaar, R., Rabe, M., Gaass, T., Schneider, M.J., Benlala, I., Eze, C., Corradini, S., Belka, C., Landry, G., Kurz, C. & Dinkel, J. (2023). Ventilation and perfusion MRI at a 0.35 T MR-Linac: feasibility and reproducibility study. *Radiation Oncology*, 18(1), 58.

Klaar, R., Rabe, M., Stüber, A.T., Hering, S., Corradini, S., Eze, C., Marschner, S., Belka, C., Landry, G., Dinkel, J. & Kurz, C. (2024). MRI-based ventilation and perfusion imaging to predict radiation-induced pneumonitis in lung tumor patients at a 0.35 T MR-Linac. *Radiotherapy and Oncology*, 199(8), 110468.

Additional Publications

I contributed to the following publication as a co-author while pursuing my dissertation at the Medical Faculty of Ludwig-Maximilians-University Munich.

Benlala, I., **Klaar, R.**, Gaass, T. Macey, J., Bui, S., De Senneville B. D., Berger, P., Laurent, F., Dournes, G. & Dinkel, J. (2023). Non-Contrast-Enhanced Functional Lung MRI to Evaluate Treatment Response of Allergic Bronchopulmonary Aspergillosis in Patients With Cystic Fibrosis: A Pilot Study. *Journal of Magnetic Resonance Imaging.* 59(3), 909-919.

Contributions to Conferences

Klaar, R., Rabe, M., Gaass, T., Schneider, M.J., Benlala, I., Corradini, S., Eze, C., Belka, C., Landry, G., Kurz, C. & Dinkel, J. Ventilation and Perfusion Imaging at a 0.35 T MR-Linac - Feasibility and Reproducibility Study. Poster presentation at *International Workshop on Pulmonary Functional Imaging* (2022), Hannover, Germany.

Klaar, R., Benlala, I., Gaass, T., Benkert, T., Benlala, I. & Dinkel, J. 3D-UTE Self-gated Ventilation resolved Imaging using a Stack-of-Spirals Sequence. Poster presentation at *ISMRM Workshop on Data Acquisition and Image Reconstruction* (2023), Sedona, Arizona, USA.

Klaar, R., Rabe, M., Gaass, T., Schneider, M.J., Benlala, I., Corradini, S., Eze, C., Belka, C., Landry, G., Kurz, C. & Dinkel, J. Ventilation and perfusion imaging at a 0.35 T MR-Linac – Feasibility and reproducibility study. Oral presentation at *ESTRO Annual Congress* (2023), Vienna, Austria.

Klaar, R., Rabe, M., Gaass, T., Schneider, M.J., Benlala, I., Corradini, S., Eze C., Belka, C., Landry, G., Kurz, C. & Dinkel, J. Feasibility and Reproducibility of Ventilation and Perfusion Imaging at a 0.35 T MR-Linac in Healthy Volunteers and Lung Cancer Patients. Poster presentation at *ISMRM Annual Congress* (2023), Toronto, Canada.

Klaar, R., Rabe, M., Gaass, T., Schneider, M.J., Benlala, I., Corradini, S., Eze C., Belka, C., Landry, G., Kurz, C. & Dinkel, J. Feasibility and Reproducibility of Ventilation and Perfusion Imaging at a 0.35 T MR-Linac in Healthy Volunteers and Lung Cancer Patients. Oral presentation in MR in RT Study Group at *ISMRM Annual Congress* (2023), Toronto, Canada.

Benlala, I., **Klaar, R.**, Gaass, T., Laurent, F., Dournes, G. & Dinkel, J. Non-contrast-Enhanced Functional Lung MRI to evaluate treatment response of ABPA in CF patients. Oral presentation by I. Benlala at *ESCR-ESTI Joint Meeting* (2023), Berlin, Germany.

Klaar, R., Rabe, M., Stüber, A.T., Corradini, S., Eze, C., Belka, C., Landry, G., Kurz, C. & Dinkel, J. Finding MR-based ventilation and perfusion parameters predictive of radiation-induced pneumonitis in lung cancer patients at a 0.35 T MR-linac. Oral presentation at *10th MR in RT Symposium* (2024), Rome, Italy.

Klaar, R., Rabe, M., Stüber, A.T., Corradini, S., Eze, C., Belka, C., Landry, G., Kurz, C. & Dinkel, J. Predicting radiation-induced pneumonitis using MR-based ventilation imaging at a 0.35 T MR-Linac. Poster discussion at *ESTRO Annual Congress* (2024), Glasgow, Scotland.

Klaar, R., Rabe, M., Stüber, A.T., Corradini, S., Eze, C., Belka, C., Landry, G., Kurz, C. & Dinkel, J. Using Ventilation and Perfusion MRI at a 0.35 T MR-Linac to Predict Radiation-Induced Pneumonitis in Lung Cancer Patients. Power Pitch and poster presentation at *ISMRM Annual Congress* (2024), Singapore.

Abstract

MR-Linacs are hybrid devices that combine linear accelerators (Linacs) for photon radiotherapy (RT) and a magnetic resonance imaging (MRI) scanner for radiation dose-free in-room imaging. Their introduction in clinical routine has revolutionized RT. Tumors in organs affected by breathing motion or daily anatomical changes as well as tumors located in bulk soft-tissue benefit from the excellent soft-tissue contrast and the real-time imaging provided by the integrated MRI-scanner. Especially patients suffering from lung tumors benefit from MRI-guided RT (MRgRT), as it enables the daily adaptation to inter-fractional anatomical changes and the additional real-time imaging permits a gated beam delivery to compensate for intra-fractional tumor motion and thus a precise dose delivery. This in turn allows to increase dose applied to the target, while decreasing the dose to the surrounding normal tissue. Despite these important advances to minimize radiation-induced normal tissue toxicities, radiation-induced pneumonitis (RP) and the later stage radiation-induced lung fibrosis (RILF) are still common complications occurring at the earliest about 2-3 months post-RT. RP cannot only result in long-term impairment, but can pose a serious health risk in severe cases, therefore identifying patients at risk and early detection of RP is crucial. Even though clinical and dosimetric parameters have been proposed with varying success, strong predictive parameters especially in the context of MRgRT are currently missing. Besides being an integral part in the treatment delivery, the integrated MRI-scanner allows to perform additional morphological, functional or other advanced imaging techniques developed at diagnostic MRI-scanners without extra costs or patient burden.

The aim of this thesis was to establish and investigate new MRI-based approaches for the prediction of RP directly after the treatment by exploiting the MR imaging possibilities of the MR-Linac and the automated radiation dose-free detection and visualization of RP at the follow-up stage using diagnostic MRI-scanners.

At first, a non-contrast enhanced functional lung MR imaging method based on 2D cine-MRI called non-uniform Fourier decomposition (NuFD), that has been successfully established at diagnostic scanners, was transferred to the low-field MR-Linac. The feasibility of the ventilation and perfusion imaging with this approach along with its potential integration into the clinical workflow was investigated in healthy volunteers. Due to the NuFD method's dependency on breathing ampli-

tude, which influences the intra-patient reproducibility of the functional maps over repeated scans, two normalization strategies were developed and their performance assessed to normalize scans employing different breathing maneuvers. This study successfully showed the validity of the NuFD method at a low-field MR-Linac in a clinical setting and both normalization strategies demonstrated a clear improvement in reproducibility compared to the uncorrected cases.
Following that, the NuFD method was integrated into a clinical study comprising the additional MR image acquisition required for the extraction of functional maps directly after at least the first and the last treatment fraction of lung tumor patients receiving MRgRT. Ventilation- and perfusion-based biomarkers were defined as change over the treatment in different lung regions and investigated regarding their potential to predict RP and compared to commonly used dosimetric parameters. In this study, it was demonstrated that the change in ventilation and perfusion over the treatment course have predictive qualities superior to the pure dosimetric parameters, enabling the identification of patients at risk of developing RP already directly after the end of treatment.
Lastly, to support the MRI-based RP prediction, the patients included in the previously mentioned study received a follow-up diagnostic MRI, including quantitative T_2-mapping, in addition to the standard-of-care computed tomography (CT) scan. Using the T_2-maps, parameters were defined based on the mean T_2 values in the high-dose region and their potential to automatically stratify patients into RP and non-RP patients evaluated. Furthermore, a voxel-based analysis was performed to develop an automated segmentation of the lung volume affected by RP to provide a first visualization of the RP extent. The T_2-based parameters revealed a strong ability to stratify patients and the T_2-based RP segmentation showed reasonable visual comparability with CT-based segmentation by a radiologist.
These studies represent important steps towards the clinical implementation of functional imaging during MRgRT and an MRI-based follow-up procedure after lung RT to identify patients at risk of developing RP early and to automatically detect RP. This has the potential to improve the patient care in the future.

Zusammenfassung

MR-Linacs sind hybride Geräte, die lineare Beschleuniger (Linacs) für die Photonenstrahlentherapie (RT) und einen Magnetresonanztomographie (MRT) Scanner für die strahlendosis-freie Bildgebung während der Behandlung kombinieren. Ihre Einführung in die klinische Routine hat die Strahlentherapie revolutioniert. Tumore in Organen, die durch Atembewegung oder tägliche anatomische Veränderungen beeinflusst werden, sowie Tumore in Körperregionen mit hohem Weichteilanteil profitieren von dem exzellenten Weichteilkontrast und der Echtzeit-Bildgebung ermöglicht durch den integrierten MRT-Scanner. Besonders Patienten mit Lungentumoren profitieren von der MRT-geführten Strahlentherapie (MRgRT), da sie die tägliche Anpassung an inter-fraktionellen anatomischen Veränderungen ermöglicht und die zusätzliche Echtzeit-Bildgebung eine gesteuerte Bestrahlung, um die intra-fraktionelle Tumorbewegung zu kompensieren, und daher eine präzise Dosisapplikation ermöglicht. Dies erlaubt die applizierte Dosis im Zielvolumen zu erhöhen, während die Dosis im umliegenden normalen Gewebe vermindert werden kann. Trotz dieser bedeutenden Fortschritte zur Minimierung der strahleninduzierten Toxizitäten im Normalgewebe, sind strahleninduzierte Lungenentzündungen (RP) und die zu einem späteren Zeitpunkt eintretende strahleninduzierte Lungenfibrose (RILF) immer noch häufig auftretende Komplikationen, die frühstens 2-3 Monate nach Bestrahlungsende auftreten. RP kann nicht nur in langfristigen Einschränkungen resultieren, sondern kann auch in schweren Fällen ein ernstzunehmendes Gesundheitsrisko darstellen, weshalb eine frühe Identifizierung von Risikopatienten und eine frühe Detektierung von RP entscheidend ist. Obwohl bereits klinische und dosimetrische Parameter mit unterschiedlichem Erfolg vergeschlagen wurden, sind stark prädiktive Parameter, speziell im Kontext der MRgRT, weiterhin fehlend. Zusätzlich zur in der klinischen Routine stattfindenden Bildgebung, erlaubt der integrierte MRT-Scanner die Aufnahme von weiteren morphologischen, funktionellen oder anderen fortschrittlichen Bildgebungstechniken, die an diagnostischen MRT-Scannern entwickelt wurden, ohne zusätzliche Kosten oder Belastung der Patienten.
Das Ziel dieser Arbeit war es neue MRT-basierte Ansätze für die Verhersage von RP direkt nach der Bestrahlung, durch die Ausnutzung der MRT-Bildgebungsmöglichkeiten am MR-Linac, und eine automatisierte strahlendosis-freie Feststellung und Visualisierung der RP in der Nachsorgephase zu etablieren und untersuchen.

Zunächst wurde eine nicht-Kontrast erhöhte funktionelle Lungen-MRT Bildgebungsmethode basierend auf 2D *cine*-MRT, gennant *non-uniform Fourier decomposition* (NuFD), die erfolgreich an diagnostischen Scannern etabliert wurde, auf einen Niederfeld MR-Linac übertragen. Die Umsetzbarkeit der Ventilations- und Perfusionsbildgebung mit diesem Ansatz und die potentielle Integration in den klinischen Ablauf wurde in gesunden Probanden untersucht. Aufgrund der Abhängigkeit der NuFD Methode von der Atemamplitude, welche die intra-Patienten Reproduzierbarkeit der funktionellen Bilder über wiederholte Aufnahmen beeinflusst, wurden zwei Normalisierungsstrategien entwickelt und bewertet, um wiederholten Messungen mit unterschiedlichen Atemmanövers zu normieren. Diese Studie zeigte erfolgreich die Validität der NuFD Methode an einem Niederfeld MR-Linac in einem kliniknahem Setting und beide Normalisierungsstrategien demonstrierten eine klare Verbesserung der Reproduzierbarkeit im Vergleich mit den nicht-korrigierten Fällen.
Darauffolgend wurde die NuFD Methode in eine klinische Studie integriert, die die zusätzliche MRT-Bildakquisition für die Extrahierung der funktionellen Ventilations- und Perfusions-Karten direkt nach mindestens der ersten und letzten Behandlungsfraktion der MRgRT von Patienten mit Lungentumoren beinhaltete. Ventilations- und Perfusions-basierte Biomarker wurden als Änderung über die Behandlung in verschiedenen Lungenregionen definiert und ihr Potential in der Vorhersage von RP untersucht und verglichen mit üblicherweise verwendeten dosimetrischen Parametern. In dieser Studie konnte gezeigt werden, dass die Änderung der Ventilation und Perfusion über die Bestrahlungsdauer prädiktive Qualitäten besitzen, welche die der dosimetrischen Parameter übersteigt und dadurch eine Identifizierung von Risikopatienten direkt nach Bestrahlungsende erlaubt.
Zuletzt, um die MRT-basierte RP Voraussage zu unterstützen, erhielten die Patienten, die in die vorhergenannten Studie eingeschlossen wurden, zusätzlich zu der Computer Tomographie (CT) als Standard Nachsorge-Bildgebung, ein diagnostisches Nachsorge MRT inklusive quantitativer T_2-Kartierung. Mithilfe dieser T_2-Karten wurden Parameter basierend auf mittleren T_2-Werten in Regionen mit hoher Dosis definiert und deren Potential zur Patientenstratifizierung in RP und nicht-RP Patienten evaluiert. Zusätzlich wurde eine voxel-basierte Analyse durchgeführt, um eine automatisierte Segmentierung des von RP befallenen Lungengewebes zu entwickeln, welche eine erste Visualisierung des RP Ausmaßes liefert. Die T_2-basierten Parameter zeigten ein starkes Vermögen die Patienten zu stratifizieren und die T_2-basierte RP Segmentierung demonstrierte eine vielversprechende visuelle Vergleichbarkeit mit der CT-basierten Segmentierung vorgenommen durch einen Radiologen.
Diese Studien stellen wichtige Schritte in Richtung der klinischen Implementierung von funktioneller Bildgebung während MRgRT and eine MRT-basierte Nachsorge nach der Lungen Strahlentherapie dar, um Risikopatienten für die Entwicklung von RP früh zu identifizieren und die RP automatisch zu detektieren. Dies hat das Potential die Patientenversorgung in der Zukunft zu verbessern.

1 | Introduction

Lung cancer is one of the most common cancer types in females and males and is a leading cause of cancer-related deaths [1–3]. In addition to being a primary cancer site, the lungs are the second most frequent site for the development of metastasis with pulmonary lesions being detected in 20-54% of metastatic extra-thoracic malignancies [4]. In patients with non-resectable tumors, radiotherapy (RT) plays a major role in curative and palliative treatment and is even considered standard-of-care in non-small cell lung cancer (NSCLC) stage I and II as well as pulmonary oligometastases [5, 6]. Especially the clinical establishment of stereotactic body radiation therapy (SBRT) for extracranial targets fostered this development [7]. The SBRT concept of delivering large doses to the target in a few treatment sessions, but limiting the normal tissue surrounding the target subjected to high doses is especially relevant for lung RT, due to the lung's high radiosensitivity [8]. One of the main requirements for the use of SBRT, particularly in lung lesions, is exact patient positioning and tumor localization to allow for accurate and precise dose delivery [7]. As exact lung tumor localization is hampered by breathing motion and in some cases even by the heartbeat, the need for real-time imaging during the treatment arose [9]. This problem has been addressed with the introduction of image-guided radiotherapy using X-rays together with implanted metal fiducial markers [10], ultrasound [11] or optical/thermal surface imaging [12] for real-time imaging and a gated beam delivery. Moreover, anatomical changes between treatment sessions are compensated for with daily treatment plan adaptation using volumetric information from computed tomography (CT) [13] or cone-beam computed tomography (CBCT) [14]. Additionally, the integration of magnetic resonance imaging (MRI) scanners into linear accelerators (Linacs) to form so-called MR-Linacs, has opened up even more opportunities in terms of magnetic resonance image-guided radiotherapy (MR-gRT). Apart form being ionizing radiation-free, MRI offers high soft-tissue contrast, which is advantageous in many treatment sites in the thorax and abdomen such as lung, pancreas and liver [15].

After the theoretical ground work was laid by Isidor Rabi, Edward Purcell and Felix Bloch regarding the magnetic properties of certain atomic nuclei that formed the research field of nuclear magnetic resonance (NMR), Paul Lauterbur was the first to make use of the NMR concepts to image objects, which later became known as MRI [16]. Since then, MRI has evolved as one of the pillars of diagnostic radi-

ology [17]. In addition to anatomical and morphological imaging, MRI allows to retrieve information and generate contrast beyond pure anatomy and morphology such as, diffusion-weighted imaging (DWI) to assess the body's micro-architecture and molecular function [18], magnetic resonance (MR) spectroscopy for metabolic imaging [19], functional imaging [20] or quantitative imaging using the tissue specific signal relaxation times (T_1, T_2, $T_{1\rho}$) [21]. Due to the lung's low proton density and its many air-tissue interfaces that cause susceptibility artifacts and thus fast signal decay, lung MRI is challenging [22]. Despite this, quantitative and functional MRI have been of great interest in lung research over the years. Quantitative MRI mapping in general and in particular T_2-mapping has been shown to aid in the characterization and differentiation between lung disease patterns and the detection of inflammation [23–25]. Similarly, research interest in functional imaging, i.e., the assessment of lung ventilation or air flow and/or lung perfusion or blood flow, has grown over the recent years. To obtain information on lung perfusion, typically a gadolinium-based contrast agent is intraveneously administered and the dilution of the contrast agent traced [26]. For the retrieval of regional ventilation information, many techniques rely on the inhalation of hyperpolarized noble gases such as helium ^{3}He and xenon ^{129}Xe, aerosols of gadolinium-based contrast agents [27], fluorinated (^{19}F) gases or oxygen [28]. However, the process of hyperpolarization is expensive and, due to the need for dedicated equipment, not easily integrable into the clinical workflow. Furthermore, the administration of gadolinium-based contrast agents is critical in certain patients [29]. Therefore, non-contrast enhanced functional imaging techniques have been developed that not only decrease the hardware requirements, but also the patient burden. Several methods have been successfully introduced over the years that are based on time-resolved cine image acquisition in free-breathing such as Fourier decomposition (FD) [30] or its extension non-uniform Fourier decomposition (NuFD) [31], phase-resolved functional lung (PREFUL) imaging [32] or self-gated non-contrast-enhanced functional lung (SENCEFUL) imaging [33]. All of these techniques utilize the correlation between signal intensity and lung density that was first proposed by Zapke et al. [34]. Using dedicated sequences with high sampling rates to capture the cardiac cycle allows to not only retrieve signal intensities introduced by breathing-related lung parenchymal density changes, but also intensity changes due to blood flow induced by the heartbeat.

As the MRI-system is integrated in the MR-Linac and can be operated separately from the Linac, MR imaging on the system is not limited to the images required for RT, but has already been shown to be feasible for the acquisition of, e.g., DWI [35], T_1- and T_2-Mapping [36], dynamic contrast-enhanced perfusion MRI [37], $T_{1\rho}$-mapping [38] and oxygen-enhanced MRI [39]. As this additional imaging is performed in treatment position and easily integrable into the clinical workflow, opportunities to use the additionally acquired images for treatment planning [40], treatment plan adaptation [41] or treatment response monitoring [42] have opened up. Another motivation for additional (functional) imaging is to use the obtained image information to develop models that would allow to predict treatment outcomes or adverse

events. Especially the latter is relevant in lung RT, where radiation-induced lung toxicities such as the early stage radiation-induced pneumonitis (RP) or late stage radiation-induced lung fibrosis (RILF) are, despite all advances towards precise dose delivery to the tumor and the efforts towards normal tissue sparing, still a common complication with reported incidences of 12-17% after MRgRT [43].
As RP is diagnosed at the earliest around 2-3 months after the end of RT and can result in severe long-term impairment such as fibrosis, efforts have been made to identify biomarkers predicting its occurrence. Dosimetric parameters such as the mean lung dose (MLD) or the lung volume (without the target volume) receiving more than 20 Gy (V20) have been considered as risk factors and introduced to serve as dose constraints in the treatment planning stage. However, both parameters showed good to limited predictive qualities in different studies [44–46]. Therefore, the research focus shifted towards the definition and investigation of function-based parameters extracted from pre-RT 4D-CT ventilation imaging [47], single photon emission computed tomography (SPECT) perfusion [46] as well as positron emission tomography (PET) ventilation and/or perfusion imaging [48, 49]. Dose parameters accounting for functional information before the start of RT such as the mean dose to highly functioning lung volume and the highly functioning lung volume receiving more than 20 Gy have been demonstrated to be predictive in most studies, but the acquisition of this functional data requires the application of additional radiation dose, the administration of radioactive compounds and/or to bring and setup the patient to a different device, which in turn increases the patient burden. As these problems are overcome by the MR-Linac with its integrated MRI-scanner, the motivation for this thesis was to investigate the possibility of transferring non-contrast enhanced functional imaging using the NuFD technique from diagnostic MRI-scanners to a low-field MR-Linac. This would allow repeated and comparable combined ventilation and perfusion imaging and the identification of MRI-function-based parameters predictive of RP. Furthermore, since (RP) patients have to undergo repeated follow-up CT imaging after the end of RT, a diagnostic MRI-based approach using T_2-mapping is presented as an outlook towards an ionizing dose-free and automated way for stratification of RP and non-RP patients and early visual assessment of the RP-affected lung volume. Such an approach could eventually replace the gold-standard CT-imaging in this context, reducing patient exposure.

The structure of this thesis is as follows: After a brief introduction into the basic principles of NMR and MRI, the MRI techniques specifically used in this thesis are explained. The concepts of photon RT in general and of MRgRT in particular are described along with background of lung specific radiation-induced toxicities. The background and theory section is concluded by an explanation of the theory behind image registration and the data analysis/statistics tools used in this thesis. Following the background section, the two publications are presented along with an additional project concerning the MRI-based follow-up assessment of lung tumor patients post-RT. The last part of the thesis is comprised by conclusions and an outlook.

2 | Background and Theory

This chapter introduces the basic theoretical concepts of the imaging and radiation treatment techniques along with post-processing and analysis approaches applied in this thesis. In Section 2.1, the principles of NMR are described, followed by an introduction into MRI in Section 2.2. Advanced MRI techniques that find application in later chapters of this thesis are explained in Section 2.3. The fundamentals of photon RT and MRgRT are presented in Sections 2.4 and 2.5. Background regarding possible radiation-induced lung toxicities is given in Section 2.6. Image registration as a necessary post-processing approach and statistical data analysis concepts are introduced in Sections 2.7 and 2.8, respectively.

2.1 Nuclear Magnetic Resonance

In this section, the theoretical background of NMR is given, starting with the introduction of nuclear spin and its magnetic moment in Section 2.1.1, followed by the concept of macroscopic magnetization in Section 2.1.2 and the radiofrequency excitation in Section 2.1.3. The Bloch equations empirically describing the temporal evolution of magnetization and the relaxation processes are explained in Section 2.1.4. The section ends with a description of the two essential signal generation approaches that find application in MRI in Section 2.1.5. A more detailed description of the concepts introduced in this section are given in, e.g., [50–53], which served as references for the following section.

2.1.1 Nuclear Spin and Magnetic Moment

Atoms consist of a specific number of protons and neutrons forming the nucleus and a certain number of electrons surrounding it. As the name suggests, NMR is concerned with the nucleus and its magnetic properties, which depend on the composition of the protons and neutrons, as their individual intrinsic spins form the nuclear spin [52]. Atomic nuclei with a non-equal number of protons and neutrons possess an intrinsic quantized nuclear spin $\boldsymbol{I}$. The quantization of the spin or intrinsic angular momentum was initially demonstrated for electrons in a famous experiment by Stern and Gerlach in 1920, but later in other experiments also derived for proton spins

[51]. The magnitude of the nuclear spin is quantized by multiples of the reduced Planck constant $\hbar$:

$$|\boldsymbol{I}| = \sqrt{I(I+1)}\hbar \tag{2.1}$$

as well as the magnitude of the nuclear spin along a direction $n_I = x, y, z$:

$$I_{n_I} = m_I \hbar, \tag{2.2}$$

where I and m_I are quantum numbers. The possible values for I are restricted to positive integer and half-integer numbers, while the $2I+1$ different m_I values range between $-I, -I+1, ..., I-1, I$.
For a non-zero nuclear spin, the magnetic moment $\boldsymbol{\mu}$ is described by:

$$\boldsymbol{\mu} = \gamma \boldsymbol{I} \tag{2.3}$$

with the gyromagnetic constant γ that is specific for every nucleus (for the proton ^{1}H: $\gamma = 26.752 \times 10^7 \frac{\text{rad}}{\text{Ts}}$). Using the quantum mechanical description and the operator expressions of the nuclear spin $\hat{\boldsymbol{I}} = \left(\hat{I}_x, \hat{I}_y, \hat{I}_z\right)$, Equations 2.1 and 2.2 reformulate to the eigenvalue equations:

$$\begin{aligned} \hat{\boldsymbol{I}}^2 \left|I, m_I\right\rangle &= I(I+1)\hbar^2 \left|I, m_I\right\rangle \\ \hat{I}_{n_I} \left|I, m_I\right\rangle &= m_I \left|I, m_I\right\rangle, \end{aligned} \tag{2.4}$$

with the eigenfunctions $|I, m_I\rangle$.

Nuclear Spins in an External Magnetic Field

Without any external fields, a nuclear state with spin I is $(2I+1)$-fold degenerated. The application of an external magnetic field $\boldsymbol{B} = B_0 \boldsymbol{e}_{n_B}$ along the direction $n_B = x, y, z$ given by the unit vector $\boldsymbol{e}_{n_B}$ and the resulting interactions between the nuclear magnetic moment and the magnetic field are in quantum mechanics described by a Hamilton operator $\hat{\boldsymbol{H}}$ [53]:

$$\hat{\boldsymbol{H}} = -\boldsymbol{\mu}\boldsymbol{B}. \tag{2.5}$$

Using Schrödinger's equation, described by:

$$\hat{\boldsymbol{H}} \left|I, m_I\right\rangle = E_m \left|I, m_I\right\rangle, \tag{2.6}$$

the eigenvalues of the interactions in a magnetic field and therefore the energy levels are given by:

$$E_{m_I} = -\gamma \hbar m_I B_0. \tag{2.7}$$

Due to dependency of Equation 2.7 on the quantum number m_I, the nuclear spin states are no longer degenerated and the difference between discrete neighboring energy levels computes to [54]:

$$\Delta E_{m_I} = E_{m_I} - E_{m_I - 1} = \gamma \hbar B_0, \tag{2.8}$$

which is commonly known as the nuclear Zeeman effect. Using the Planck relation:

$$\Delta E = \hbar\omega, \tag{2.9}$$

stating that the energy of electromagnetic radiation, that needs to be absorbed or emitted by a particle to transfer to a upper or lower discrete energy level, is proportional to its frequency ω and Equation 2.8, the resonance frequency is defined by:

$$\omega_L = \gamma B_0. \tag{2.10}$$

Equation 2.10, also known as Larmor equation, describes the resonance or Larmor frequency necessary for the nuclei to absorb energy and is a key concept for NMR and MRI. According to the MRI conventions, the static magnetic field $\boldsymbol{B_0}$ used in the following is assumed to point along the z-direction, i.e., $\boldsymbol{B}_0 = B_0\boldsymbol{e}_z$.

2.1.2 Macroscopic Magnetization

In a sample consisting of a number of atomic nuclei N_{nuclei}, e.g., the human body, each nucleus possesses an intrinsic spin angular momentum with a specific direction or so-called spin polarization axis. Without the presence of an external magnetic field, each spin polarization axis points in a different direction, as visualized in Figure 2.1 (A), and the distribution of the magnetic moments is isotropic, thus no macroscopic magnetization is observed. This situation changes with the application of the external magnetic field, as introduced in Section 2.1.1. Assuming thermal equilibrium between the nuclei in a sample and their surroundings at room temperature ($k_BT \gg \gamma\hbar B_0$), the occupation probability p_{m_I} for each energy level is given by the Boltzmann distribution [53]:

$$p_{m_I} = \frac{\exp\left(-\gamma\hbar m_I B_0/k_BT\right)}{\sum_{m=-I}^{I} \exp\left(-\gamma\hbar m B_0/k_BT\right)} \tag{2.11}$$

with the Boltzmann constant k_B and the temperature T. Using Equation 2.11 and the formula for the expectation value with mixed states, the macroscopic magnetization M_0 is computed to:

$$M_0 = -N_{\text{nuclei}} \sum_{m=-I}^{I} p_{m_I} \cdot \langle m| \mu_z |m\rangle \approx \frac{N_{\text{nuclei}}\gamma^2\hbar^2 I(I+1)}{3k_BT} B_0 \tag{2.12}$$

using the approximation for high temperatures as mentioned above. The non-zero macroscopic magnetization means, that the nuclear spin angular momentum directions partially align with an external magnetic field as shown in Figure 2.1 (B).

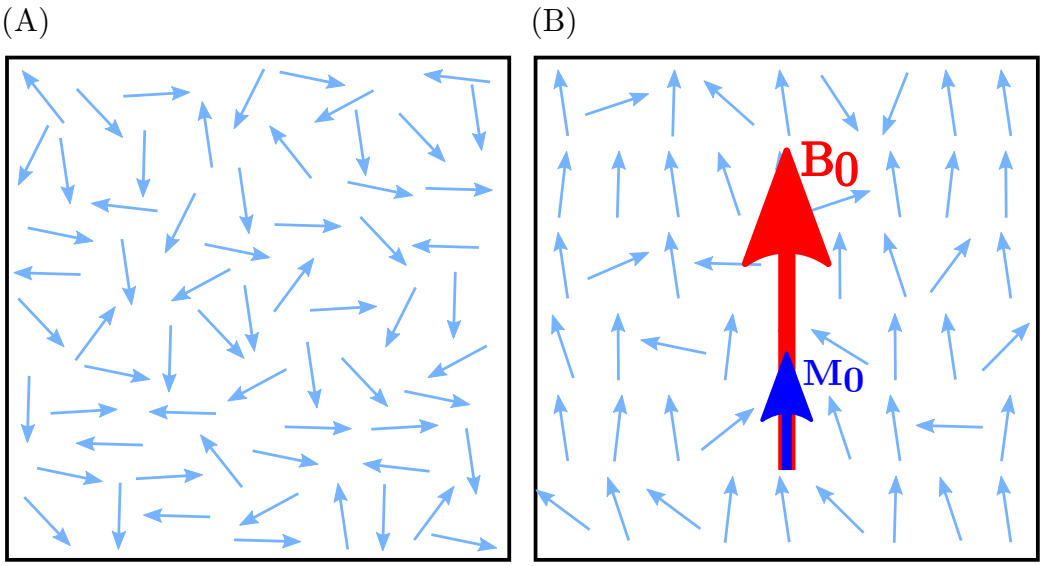

FIGURE 2.1: **Nuclear spin polarizations.** The nuclei in a sample, for simplicity indicated by the light-blue arrows, each possess a spin angular momentum that can point in any direction if no external magnetic field is present (A). With the application of an external magnetic field B_0 (red arrow), the directions of the spin angular momentum partially point along the direction of the magnetic field (B) and are no longer isotropic resulting in a non-zero macroscopic magnetization M_0 (blue arrow). Adapted from [55].

Temporal Evolution of Magnetization

In a more generalized setting, where a temporally changing external magnetic field $\boldsymbol{B}(t)$ is applied to the nuclear spins in a sample, the macroscopic magnetization vector $\boldsymbol{M}$ is given by the sum of the individual expectation values of the magnetic moment of each nuclei [53]:

$$\boldsymbol{M} = \sum_{i=1}^{N_{\text{nuclei}}} \langle \boldsymbol{\mu}_i \rangle. \tag{2.13}$$

With Equation 2.13, the Heisenberg equation and making use of the commutative property of angular momentum operators, the temporal evolution of the macroscopic magnetization's expectation value can be derived as:

$$\frac{\mathrm{d}\boldsymbol{M}(t)}{\mathrm{d}t} = -\frac{i}{\hbar}\left[\boldsymbol{M}, \hat{\boldsymbol{H}}\right] = \boldsymbol{M}(t) \times \gamma \boldsymbol{B}(t), \tag{2.14}$$

which shows that $\boldsymbol{M}(t)$ precesses around $\boldsymbol{B}(t)$ with the Larmor frequency ω_L (Equation 2.10) in case of a constant, external magnetic field. The equilibrium of the magnetization ($\frac{\mathrm{d}\boldsymbol{M}(t)}{\mathrm{d}t} = 0$) is reached if $\boldsymbol{M} \parallel \boldsymbol{B}$.

2.1.3 Radiofrequency Excitation

As the macroscopic magnetization along the external magnetic field direction is very small compared to the external field, a second radiofrequency (RF) magnetic field $\boldsymbol{B}_1(t)$ perpendicular to $\boldsymbol{B}_0$ is necessary to eventually measure the magnetization:

$$\boldsymbol{B}_1(t) = B_1(\cos(\omega_1 t), \sin(\omega_1 t), 0) \tag{2.15}$$

with B_1 and ω_1 being the magnitude and the frequency of $\boldsymbol{B}_1(t)$, respectively. Inserting Equation 2.15 into the temporal evolution of the magnetization given in Equation 2.14, gives:

$$\frac{\mathrm{d}\boldsymbol{M}(t)}{\mathrm{d}t} = \gamma \boldsymbol{M}(t) \times (B_1 \cos(\omega_1 t), B_1 \sin(\omega_1 t), B_0). \tag{2.16}$$

A common approach to simplify this description is to perform a transform from the initial, resting coordinate system (x, y, z) to a coordinate system (x', y', z') that rotates around the z-axis with ω_1. With this, Equation 2.16 simplifies to:

$$\frac{\mathrm{d}\boldsymbol{M'}(t)}{\mathrm{d}t} = \gamma \boldsymbol{M'}(t) \times (B_1, 0, B_0 - \omega_1/\gamma) = \gamma \boldsymbol{M'}(t) \times \boldsymbol{B}_{\text{eff}} \tag{2.17}$$

illustrating that the magnetization in the rotating reference frame $\boldsymbol{M'}(t)$ precesses around an effective magnetic field $\boldsymbol{B}_{\text{eff}}$. If the resonance condition is full-filled, meaning $\omega_1 = \omega_L = \gamma B_0$, the z-component of $\boldsymbol{B}_1$ vanishes and the magnetization is flipped into the x-y-plane.
The angle between the magnetization in the reference frame $\boldsymbol{M'}(t)$ and the z'-axis, the so-called flip angle α_{Flip}, depends on the magnitude of the RF-field and the duration of the RF-field pulse t_1:

$$\alpha_{\text{Flip}} = \gamma B_1 t_1, \tag{2.18}$$

which converts into an integral over time in case of an RF-pulse with modulated amplitude:

$$\alpha_{\text{Flip}} = \gamma \int_0^{t_1} B_1(t)\, \mathrm{d}t. \tag{2.19}$$

2.1.4 Bloch Equations and Relaxation

Based on Equation 2.13, after excitation with an RF-pulse ($\boldsymbol{B}_1$-field) the macroscopic magnetization is assumed to precess unperturbed under a given flip angle α_{Flip} around the z-axis. Due to interactions of the individual spins with other spins as well as with their the environment, the components M_x and M_y, that combine to the commonly called transversal magnetization M_{T} ($\boldsymbol{M}_{\text{T}} = M_x \boldsymbol{e}_x + M_y \boldsymbol{e}_y$), decay to zero over time, while the commonly called longitudinal component along the

constant field $\boldsymbol{B}_0$, M_z or M_L, approaches the equilibrium state M_0. This observation was included as extension to Equation 2.13 by Felix Bloch to form the Bloch equations [56]:

$$\begin{aligned}\frac{\mathrm{d}M_x}{\mathrm{d}t} &= \gamma(\boldsymbol{M}\times\boldsymbol{B}_0)_x - \frac{M_x}{T_2}\\ \frac{\mathrm{d}M_y}{\mathrm{d}t} &= \gamma(\boldsymbol{M}\times\boldsymbol{B}_0)_y - \frac{M_y}{T_2}\\ \frac{\mathrm{d}M_z}{\mathrm{d}t} &= \gamma(\boldsymbol{M}\times\boldsymbol{B}_0)_z - \frac{M_z - M_0}{T_1},\end{aligned} \tag{2.20}$$

where T_1 is introduced as spin-lattice relaxation time of M_L and T_2 as the spin-spin relaxation time of M_T.

Spin-Lattice Relaxation

Even though the term "lattice" was introduced in the early days of NMR, where crystals were the primary subject, this type of relaxation describes the interactions between the nuclear spins and their surroundings regardless of the aggregate state of the sample. Due to thermal motion of the atoms and molecules in a sample, the electrons and nuclei of these particles introduce rapidly fluctuating magnetic fields on a microscopic level. As some of these magnetic fields fluctuate with the Larmor frequency of the nuclear spins, transitions between energy levels are induced according to the Zeeman effect. Over time, this process drives the recovery of equilibrium magnetization M_0 along the static magnetic field. Finding a solution for the Bloch equations (Equation 2.20), allows to describe the temporal evolution of the longitudinal magnetization $M_\mathrm{L} = M_z$ after an RF excitation pulse with $\alpha_\mathrm{Flip} = 90°$ [51]:

$$M_\mathrm{L}(t) = M_0\left(1 - \exp\left(\frac{-t}{T_1}\right)\right). \tag{2.21}$$

An example of this temporal evolution is visualized for three different tissue types with different T_1 times in Figure 2.2 (A). A formal derivation of the relaxation phenomenon can be found in [57].

Spin-Spin Relaxation

The spin-spin relaxation or more generally T_2 relaxation consists of several mechanisms contributing to the decay of the transversal magnetization M_T. Apart from the previously described spin-lattice interactions that not only influence the longitudinal, but also the transversal magnetization, as the affected nuclear spins stop contributing to the M_T, one additional process are the spin-spin interactions without energy exchange. Immediately after the RF-pulse excitation, the nuclear spins precess with the same frequency and phase around the axis of the static magnetic field. The fluctuating microscopic magnetic fields that occur due to the thermal motion also contribute to the net magnetic field that a nuclear spin experiences, resulting in a slightly different angular frequency of affected spins. Over time, these differences

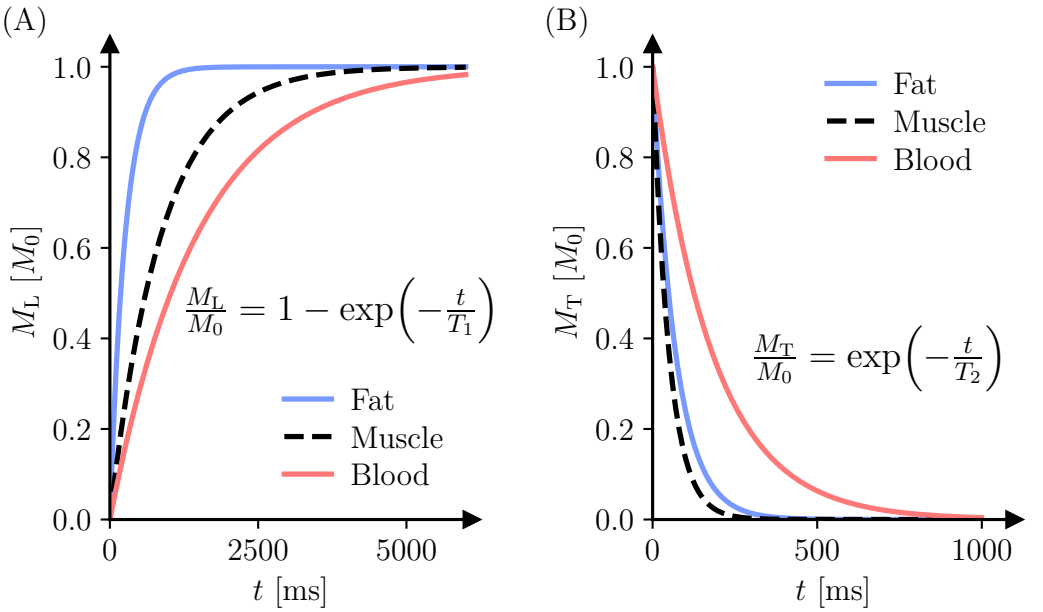

FIGURE 2.2: **T_1 and T_2 relaxation.** In Subfigure (A), the T_1 relaxation or the recovery of the longitudinal magnetization M_L after a $\alpha_{Flip} = 90°$ RF excitation pulse is shown for fat and muscle tissue as well as blood. Subfigure (B), similarly, depicts the T_2 relaxation or the decay of the transversal magnetization M_T after an 90° RF-pulse. Own figure.

in precession frequency cause the build-up of a random phase difference between the spins until a total loss of the initial phase coherence and a decay of the transversal magnetization M_T. With the Bloch equations in Equation 2.20, the temporal evolution of the transversal magnetization M_T after a 90° RF-pulse is found to be [51]:

$$M_T(t) = M_0 \exp\left(\frac{-t}{T_2}\right). \tag{2.22}$$

An exemplary decay of the transversal magnetization for three different tissue types and their corresponding T_2 times is displayed in Figure 2.2 (B).

Free Induction Decay and T_2^* Relaxation

In addition to the T_2 relaxation time that describes the loss of phase coherence due to internal microscopic magnetic fields, there exists another dephasing mechanism with the corresponding relaxation time constant T_2' that is caused by local inhomogeneities of the static magnetic field $\boldsymbol{B}_0$ or by magnetic field gradients generated on interfaces of tissue with different magnetic susceptibilities. The T_2' time is in most cases much shorter compared to T_2 and therefore usually the dominating mechanism causing the loss of the transversal magnetization as observed in the free induction decay (FID),

the temporal evolution of M_T immediately after the RF-pulse as shown in Figure 2.3. Mathematically, T_2^* is considered a combination of the spin-spin relaxation effects (T_2) and the local field inhomogeneities, introduced by the magnetic field and the sample, corresponding to the relaxation time T_2' [58]:

$$\frac{1}{T_2^*} = \frac{1}{T_2} + \frac{1}{T_2'}. \tag{2.23}$$

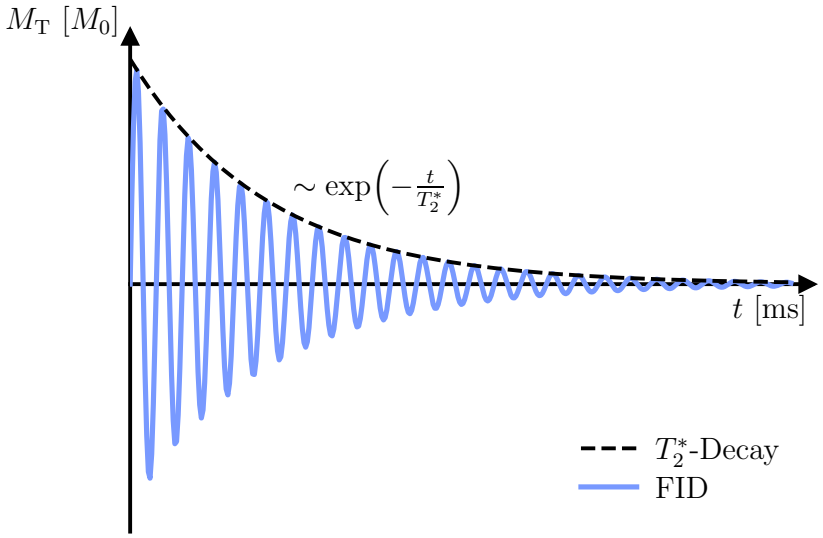

FIGURE 2.3: **Free induction decay (FID).** The decay of the transversal magnetization M_T (free induction decay), starting directly after the radiofrequency excitation, is induced by a combination of spin-spin interactions (described by the T_2 relaxation) and inhomogeneities of the static magnetic field (T_2') and follows a damped oscillation. Own figure.

2.1.5 Spin and Gradient Echo

One of the essential concepts of NMR, that also forms the basis of MRI signal generation and sequence development, is the formation of echoes. Even though more complex strategies have been introduced to achieve the echo formation, e.g., Hahn echo and stimulated echo, the two basic mechanisms, namely the spin echo (SE) and the gradient echo (GRE) still serve as the basis to characterize different MRI sequences.

Spin Echo

The key to the formation of a spin echo is the reversibility of the spin dephasing due to $\boldsymbol{B}_0$-field inhomogeneities. Based on this, the procedure to generate a spin echo is as

follows [59, 60]: The macroscopic magnetization that points along the direction of the static $\boldsymbol{B}_0$ (along the z-axis), is tipped into the transversal plane using a $\alpha_{\text{Flip}} = 90°$ RF-pulse (perpendicular to $\boldsymbol{B_0}$ (in the x-y-plane)) where the initially phase coherent spins start to dephase and the transversal magnetization starts to decay in the free induction decay (with T_2^*). The application of a second RF-pulse with a flip angle of $\alpha_{\text{Flip}} = 180°$ changes the precession or dephasing direction of the spins, leading to a rephasing of the spins and a recovery of the transversal magnetization. Even though the 90°-180° flip angle scheme is considered the basic spin echo, the flip angles of both RF-pulses can be set to arbitrary values to form a spin echo. For simplicity, the 90°-180° scheme was used here. A sketch of the basic spin echo formation is given in Figure 2.4. The temporal evolution of M_{T} in case of a spin echo formation

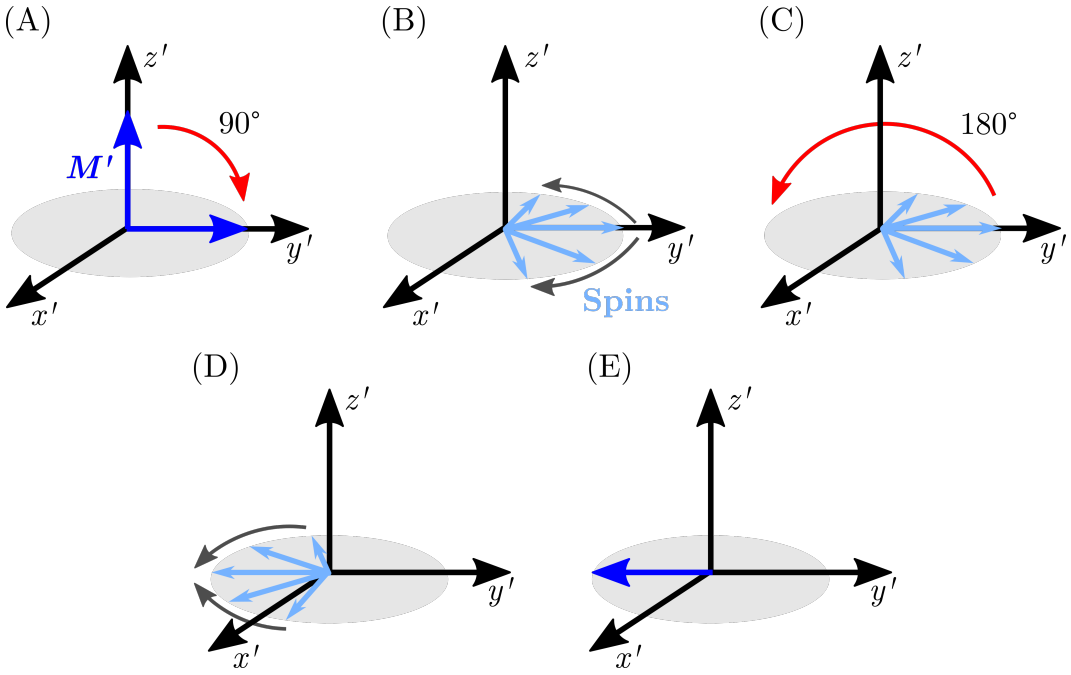

FIGURE 2.4: **Spin echo generation.** After the 90° RF-pulse, the macroscopic magnetization (blue arrow) pointing along the static magnetic field direction (z'-axis) is tipped into the transversal plane (Subfigure (A)), the spins (light-blue) pointing in the transversal direction start to dephase (B). Applying an additional 180° RF pulse (C), results in a rephasing of the transversal spins (D) and the regain of the (macroscopic) transversal magnetization. Adapted from [51].

is visualized Figure 2.5 (A).

Gradient Echo

The fundamental idea of the gradient echo formation, namely the generation/recovery of transversal magnetization, is the same as for the SE. Instead of using an addi-

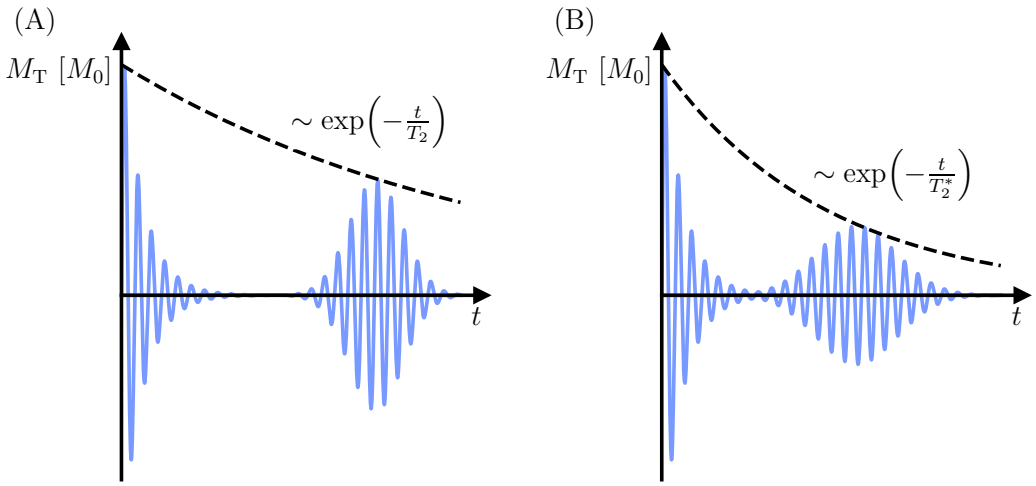

FIGURE 2.5: **Spin echo and gradient echo.** The evolution of the transversal magnetization over time, starting from the RF excitation to the echo formation. In Subfigure (A), the formation of a spin echo is visualized, where the magnetization amplitude decay is described by the tissue-specific T_2. In Subfigure (B), the formation of a gradient echo is displayed. In this case, the amplitude decay depends on the T_2^* relaxation time and therefore on both, the spin-spin interactions and inhomogeneities of the static magnetic field. Own figure.

tional 180° RF-pulse, the echo is formed by manipulating the magnetic field with magnetic field gradients. The procedure is as follows [61]: Similar to the SE, the magnetization along the z-axis is transferred into the x-y-plane by the application of a 90° RF-pulse. It has to be noted that the flip angle α_{Flip} can be set to an arbitrary value, but is for simplicity chosen to be 90°. A fast dephasing of the spins is achieved by applying a linear magnetic field gradient to perturbate the magnetic field. After a certain time, the inverse of the field gradient is applied, resulting in a rephasing and an echo formation of the transversal magnetization. A key difference between SE and GRE is that, while the SE is independent of T_2^* and is only influenced by T_2, due to inversion of dephasing caused by T_2', GRE is dependent on T_2^*. In Figure 2.5 (B), the gradient echo formation of the transversal magnetization is shown.

2.2 Magnetic Resonance Imaging (MRI)

Magnetic resonance imaging is one of the most common use cases of NMR described in Section 2.1, especially with its widespread application in the medical field. As the human body consists in large parts of water and therefore of hydrogen atoms (protons) with a non-zero nuclear spin ($I = \frac{1}{2}$), ^{1}H MRI ($\gamma = 26.752 \times 10^7 \frac{\text{rad}}{\text{Ts}}$) has developed into one of the main imaging techniques in the clinical routine. A typical MRI-scanner comprises the three main components: the static, homogeneous

magnetic field $\boldsymbol{B}_0$ that is either provided by a permanent magnet or is induced by a super-conducting coil; the radiofrequency field system that generates the $\boldsymbol{B}_1$-field perpendicular to the $\boldsymbol{B}_0$-field and thirdly the gradient system that allows to overlay magnetic field gradients in all spatial directions and thus serves the spatial encoding of acquired MR-signals. This section briefly covers the key concept of using the field gradients for spatial differentiation in Section 2.2.1, along with basic k-space sampling strategies in Section 2.2.3, MR image reconstruction in Section 2.2.4 and imaging sequences that found application in various parts of this thesis in Section 2.2.5.

2.2.1 Spatial Encoding

As explained in Section 2.1, placing an object or sample in a homogeneous and static $\boldsymbol{B}_0$-field causes the nuclear spins within the sample to align with and precess around the magnetic field direction, thereby building a macroscopic magnetization. The transversal component of this macroscopic magnetization is measurable after the application of time-dependent RF-pulses ($\boldsymbol{B}_1(t)$), as it introduces a voltage in the coil system used for read-out. The relationship between this complex acquired signal $S(t)$ and the complex transversal magnetization of the considered sample (examined body part) $\tilde{m}_\mathrm{T} = M_x + \mathrm{i}M_y$ at position $\boldsymbol{x}$ is given by [51]:

$$S(t) \propto \int_V \tilde{m}_\mathrm{T}(\boldsymbol{x}, t) \exp\left(-i\Omega t + i\Phi(\boldsymbol{x}, t)\right) \mathrm{d}V, \tag{2.24}$$

with V being the examined sample volume, Ω being the reference frequency and Φ being the accumulated phase of the spins up to a time t, due to the magnetic fields:

$$\Phi(\boldsymbol{x}, t) = \int_0^t \omega\big(\boldsymbol{x}, t'\big)\mathrm{d}t'. \tag{2.25}$$

The measured signal that is induced in the receiver coil of the MRI-scanner is therefore a sum of signal components covering the entire volume. In order to spatially differentiate between the different signal components, the whole volume is divided into equally spaced small volume elements (voxels). Using a gradient system consisting of three coils allows to superimpose the static $\boldsymbol{B}_0$-field with linear magnetic gradient fields $\boldsymbol{G}_a = G_a \boldsymbol{e}_a$ of strength G_a in all spatial dimensions $a = x, y, z$. This enables the introduction of a temporal and spatial dependency of the Larmor frequency. To voxel-wise spatially encode the MRI signal, typically gradient fields pointing along the z-direction (here defined as pointing along the $\boldsymbol{B}_0$), but whose strengths depend on the different spatial directions are applied before or during the signal acquisition [50].
Based on the resonance principle and the assumption of a homogeneous main magnetic field, all excited nuclear spins perform a precession with the Larmor frequency

$\omega_L = \gamma B_0$. Employing gradient fields along the spatial directions, the frequency at a position $\boldsymbol{x}$ changes to:

$$\omega(\boldsymbol{x}, t) = \gamma(B_0 + \boldsymbol{G}(t)\boldsymbol{x}) \tag{2.26}$$

with $\boldsymbol{G} = \boldsymbol{G}_x + \boldsymbol{G}_y + \boldsymbol{G}_z$ being the sum of the gradient fields in all spatial directions. Using Equation 2.26, the accumulated phase of the spins modifies to:

$$\Phi(\boldsymbol{x}, t) = \int_0^t \gamma(B_0 + \boldsymbol{G}(t)\boldsymbol{x}) = \omega_L t + \gamma \int_0^t \boldsymbol{G}(t')\boldsymbol{x}\,\mathrm{d}t'. \tag{2.27}$$

Using the definition of the spatial frequencies $\boldsymbol{k}(t)$:

$$\boldsymbol{k}(t) = \gamma \int_0^t \boldsymbol{G}(t')\,\mathrm{d}t', \tag{2.28}$$

allows to rewrite Equation 2.27 as:

$$\Phi(\boldsymbol{x}, t) = \omega_L t + \boldsymbol{k}(t)\boldsymbol{x}. \tag{2.29}$$

Applying Equation 2.29 and $\Omega = \omega_L$, the expression in Equation 2.24 reduces to:

$$S(t) \propto \int_x \int_y \int_z \tilde{m}_{\mathrm{T}}(\boldsymbol{x}, t) \exp\left(i\boldsymbol{k}(t)\boldsymbol{x}\right) \mathrm{d}x\mathrm{d}y\mathrm{d}z, \tag{2.30}$$

which results in the measured signal being proportional to a Fourier transform (FT):

$$S(\boldsymbol{k}(t)) \propto \mathcal{FT}(\tilde{m}_{\mathrm{T}}). \tag{2.31}$$

In order to spatially recover the transversal magnetization with the inverse FT, gradient fields have to be applied to measure the signal $S(\boldsymbol{k})$ at different spatial frequencies $\boldsymbol{k}$, i.e., to efficiently sample the so-called k-space (details given in Section 2.2.3) [51]. Due to the signal being only sampled at discrete spatial frequencies, it has to be kept in mind that the FT in Equation 2.31 consequently reduces to the discrete FT, which ultimately reduces the available spatial resolution. In order to sample the 3D k-space, two techniques, namely frequency encoding and phase encoding are utilized.

Frequency Encoding

As mentioned before, the application of a gradient field along a direction allows to introduce a spatial dependency of the precession frequency. This process is known as frequency encoding. Assuming only a single gradient, introducing frequency variations in x-direction, is applied along the z-direction ($G_{\mathrm{Freq}} = G_x^z$, the z-component of the gradient field $\boldsymbol{G}_x$), the precession frequency (Equation 2.26) changes to:

$$\omega(x, t) = \omega_L + \gamma G_{\mathrm{Freq}} x \tag{2.32}$$

and Equation 2.28 to:

$$k_x(t) = \gamma \int_0^t G_{\text{Freq}}\, \mathrm{d}t' = \gamma G_{\text{Freq}} t. \tag{2.33}$$

Consequently, discrete and uniformly spaced k-space points along the x-direction (k_x) are collected by measuring the signal at a constant rate during the application of a constant gradient G_{Freq} over time [51]. Each sampling point is considered one frequency encoding step. With this, the measured signal can be differentiated along the x-direction, but not along the y- and z-direction [51].

Phase Encoding

In order to achieve spatial encoding along the two remaining directions, an additional approach has to be utilized. Instead of influencing the precession frequency of the spins, in phase encoding, the phase $\varphi(\boldsymbol{x})$ of the precessing spins is varied [62]. By employing a gradient field, e.g., along the y-direction, i.e., $G_{\text{Phase}} = \boldsymbol{G}_y^z$ for a constant duration T_{Phase} before the signal acquisition, the accumulated phase (Equation 2.27) directly after the G_{Phase} application is:

$$\Phi(\boldsymbol{x}, t) = \omega_L t + \gamma \int_0^{T_{\text{Phase}}} G_{\text{Phase}}(t')\, y\, \mathrm{d}t' = \omega_L t + \gamma T_{\text{Phase}} G_{\text{Phase}} y \tag{2.34}$$

and consequently:

$$k_y = \gamma \int_0^{T_{\text{Phase}}} G_{\text{Phase}}(t')\, \mathrm{d}t = \gamma T_{\text{Phase}} G_{\text{Phase}}. \tag{2.35}$$

While the spins precess with a spatially dependent frequency (along x-direction) introduced by G_{Freq}, the spatially dependent phase variations (along y) due to G_{Phase} are constant along the frequency encoding axis (x). Thus, in order to encode along the y-direction, i.e., to differentiate between different voxels along the y-direction, the magnitude of the phase encoding gradient G_{Phase} has to be changed before each new signal echo. Each magnitude change of the phase encoding gradient is considered one phase encoding step.
For full 3D spatial encoding, a phase encoding gradient $G_{\text{Phase},2} = \boldsymbol{G}_z^z$, that introduces phase variations along the z-direction, is applied similarly to G_{Phase}.

2.2.2 Slice Selection

Apart from the spatial encoding within a defined region, the gradient fields also allow the selective excitation of a specific region or sub-volume within the examined sample. For this, a slice selective gradient field $G_{\text{Slice}} = \boldsymbol{G}_{a_{\text{Slice}}}^z$ is applied along a specified

direction a_{Slice} at the same time as the RF-pulse with finite bandwidth. With this, a 2D slice perpendicular to the direction of G_{Slice} is excited as the precession frequency becomes linearly dependent on the position along the G_{Slice}-axis:

$$\omega(a_{\text{Slice}}) = \omega_L + \gamma G_{\text{Slice}} a_{\text{Slice}}. \tag{2.36}$$

In order to uniformly excite a slice, e.g., along the z-direction ($a_{\text{Slice}} = z$) at the position z_{Slice} with a slice thickness of Δz, as shown in Figure 2.6, spanning from $z_{\text{Slice}} - \Delta z$ to $z_{\text{Slice}} + \Delta z$ and ideally only creating transverse magnetization within this region, the bandwidth BW of the RF-pulse needs to fulfill:

$$\text{BW} = \gamma G_{\text{Slice}}[(z_{\text{Slice}} + \Delta z) - (z_{\text{Slice}} - \Delta z)] = \gamma G_{\text{Slice}} \Delta z. \tag{2.37}$$

Consequently, the slice thickness Δz is given by:

$$\Delta z = \frac{\text{BW}}{\gamma G_{\text{Slice}}} \tag{2.38}$$

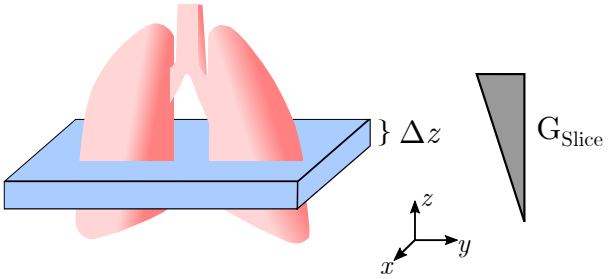

FIGURE 2.6: **Slice selection.** The application of a slice selective gradient G_{Slice} along the slice direction (here z-axis) allows the excitation of only the spins within a subvolume (slice) of thickness Δz. Inspired by [55].

2.2.3 *k*-Space Sampling Strategies

As already mentioned in Section 2.2.1, the measured signal $S(\boldsymbol{k}, t)$ and the magnetization $m(\boldsymbol{x}, t)$ are connected via a Fourier transform, meaning that they form a Fourier transform pair and that there is a relationship between the image, i.e., the transversal magnetization of the object in $\boldsymbol{x}$ space and the data, i.e., the acquired signal in $\boldsymbol{k}$ space. Therefore, in order to be able to sufficiently reconstruct the magnetization from the signal, the signal is to be acquired at a constant rate over a large number of discrete k-values. The number of k-space data points, written in matrix form in 2D $N_{\text{Freq}} \times N_{\text{Phase}}$, is given by the number of frequency encoding steps N_{Freq} and the number of different phase encoding gradient steps N_{Phase}. The extent of the traversed k-space, given by the maximal k-space point in x- and y-direction, $k_{x,\text{max}}$

and $k_{y,\max}$, determines the resolution of the reconstructed image [63]:
In x-direction:

$$\Delta x = \frac{1}{2k_{x,\max}} \tag{2.39}$$

In y-direction:

$$\Delta y = \frac{1}{2k_{y,\max}}. \tag{2.40}$$

Similarly, the distance between two k-space datapoints, Δk, dictates the extent of the object in physical space, known as the field-of-view (FOV) [63]:

$$\mathrm{FOV}_x = \frac{1}{\Delta k_x} \tag{2.41}$$

$$\mathrm{FOV}_y = \frac{1}{\Delta k_y}. \tag{2.42}$$

Depending on the application and its respective requirements, different strategies to sample the k-space are used. The most basic k-space sampling strategy or k-space trajectory is the cartesian trajectory (Figure 2.7 (A)), where each k_y line, i.e., N_{Freq} k_x points, is sampled after an RF-pulse excitation while keeping the frequency encoding gradient constant. After the acquisition of one k_y line, the phase encoding gradient is changed to sample the next line and a new RF-pulse is required. A slight derivation from this is the echo-planar imaging, where k-space trajectory follows a cartesian grid, but is continuously sampled after one RF excitation pulse using multiple echos. Apart from the cartesian strategies, non-cartesian strategies such as radial, as shown in Figure 2.7 (B) or spiral sampling exist and can be advantageous for certain applications due to their motion robustness and higher signal-to-noise ratio [63].

2.2.4 Image Reconstruction

As described in Section 2.2.1, the acquired signal is according to Equation 2.31 given by the FT of the magnetization of the scanned object and can be expressed by [63]:

$$S(\boldsymbol{k}) = \int_x \int_y \int_z M(\boldsymbol{x}, t) \exp\left(i\boldsymbol{k}(t)\boldsymbol{x}\right) \mathrm{d}x\mathrm{d}y\mathrm{d}z = \mathcal{FT}(M(\boldsymbol{x})). \tag{2.43}$$

In order to retrieve the actual MR image from the signal, which is given by the magnetization in each voxel $M(\boldsymbol{x})$ of the object, the inverse FT is calculated:

$$M(\boldsymbol{x}) = \mathcal{FT}^{-1}(S(\boldsymbol{k})). \tag{2.44}$$

Due to the fact that the signal is only sampled in a discrete fashion for discrete k-space datapoints (Section 2.2.3), only the discrete FT is calculated. In practice, this direct reconstruction approach is usually done by employing the fast Fourier

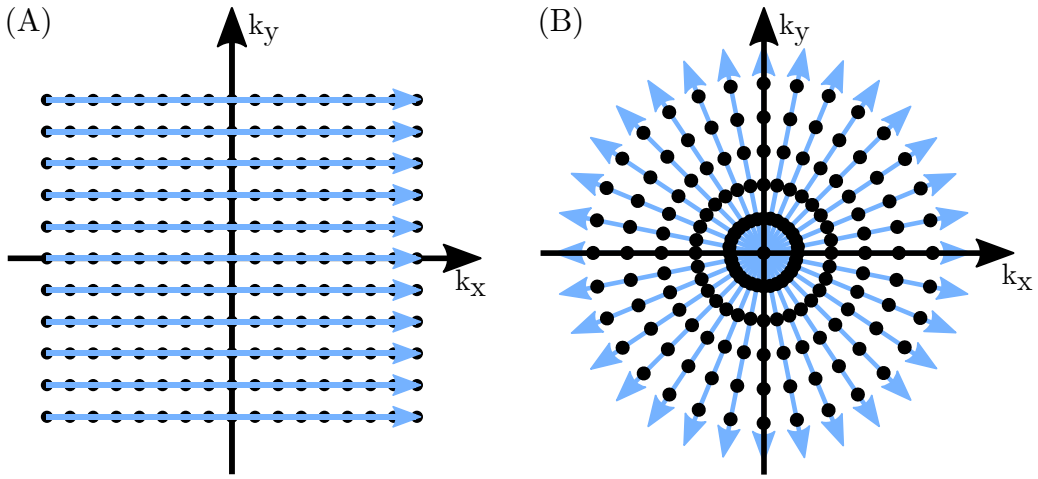

FIGURE 2.7: **Two exemplary *k*-space sampling strategies.** In Subfigure (A), a cartesian *k*-space sampling approach is depicted. Subfigure (B) illustrates radial sampling.

transform (FFT), which allows an efficient FT calculation for cartesian sampling [64]. In the case of non-cartesian sampling or undersampled data, either a direct approach using the non-uniform fast Fourier transform (NuFFT) or an indirect approach using iterative reconstruction can be utilized.
A more detailed description of image reconstruction approaches can be found in [63].

2.2.5 Imaging Sequences

Even though the basic signal acquisition and spatial encoding principle is similar in different applications, the main difference is in how RF-pulses are used to excite and prepare the nuclear spin system of the sample, which are know as different pulse or imaging sequences. The two main sequence categories are spin echo and gradient echo sequences that served as foundation for many sequence types that have been derived from these basic concepts. The selection of a particular sequence strongly depends on the application. One important factor that needs to be taken into consideration for the sequence selection for the imaging of a specific organ or body part is the image contrast, which is in turn influenced by the sequence parameters. Apart from the proton density present in the organ, dictating the signal amplitude, the echo time TE and the repetition time TR are two of the main influencing factors. TE describes the time between the center of the RF excitation pulse and the center of the signal echo, while TR is considered as the time between two consecutive RF excitation pulses.
Even though there exist mixed contrasts, it is typically differentiated between three basic contrasts or weightings [53]:

- **T_1-weighted:** Typically achieved by using short TR (TR $\ll T_1$) and short TE (TE $\ll T_2$).
- **T_2-weighted:** Typically achieved by using long TR and long TE
- **proton density-weighted:** Typically achieved by using long TR (TR $\geq T_1$) and short TE (TE $\ll T_2$)

Depending on the tissue composition in the imaged sample or body part and the respective T_1 and T_2 times of the tissue components, one contrast might be preferred over the other.

Spin Echo Sequence

The spin echo or SE sequence is one of the most basic MRI sequences and has been adapted for many different clinical applications over the years [65]. It utilizes the concept of rephasing after signal loss caused by static magnetic field inhomogeneities and susceptibility effects as described in Section 2.1.5. To acquire MR images from a formed SE, as shown in Figure 2.5 (A), gradient fields are required for spatial encoding and slice selection. A typical SE sequence diagram with cartesian k-space sampling is displayed in Figure 2.8. The start of the sequence and the beginning of a new repetition is the 90° excitation pulse and the simultaneously applied slice selection gradient. In order to compensate for the initial slice selective gradient and to rephase the spins, a rephasing gradient is subsequently applied with opposite polarity [66]. Along with the rephasing gradient, the pre-winding frequency encoding gradient and the phase encoding gradient are simultaneously employed to move the start of the k-space trajectory from the k-space center to the periphery [65, 67]. After the succeeding 180° refocusing pulse, during which the slice selective gradient is utilized again, the read-out frequency encoding gradient is applied to acquire the signal for the current k-space line. As the 180° pulse reverses the initial effect of the pre-winding gradient (frequency direction), the read-out gradient and the pre-winding gradient share the same polarity to ensure that the echo is formed at the mid-point of the read-out gradient (after TE), which coincides with the middle of the k-space line [65]. In order to sample the full k-space and consequently acquire the full MR image, this procedure has to be repeated for several phase encoding gradient strengths as the defined by the acquisition matrix.

Gradient Echo Sequence

Similar to SE sequences, gradient echo or GRE sequences are the basis for many sequences used in the clinical routine and are specifically important for applications where fast imaging is required [68]. As already mentioned in Section 2.1.5, in GRE imaging, a signal echo is formed without the need for a 180° refocusing pulse by a reversal of the read-out gradient using the signal from the excitation pulse that undergoes the FID [68]. Hence, the echo formation can be speeded up, but the GRE

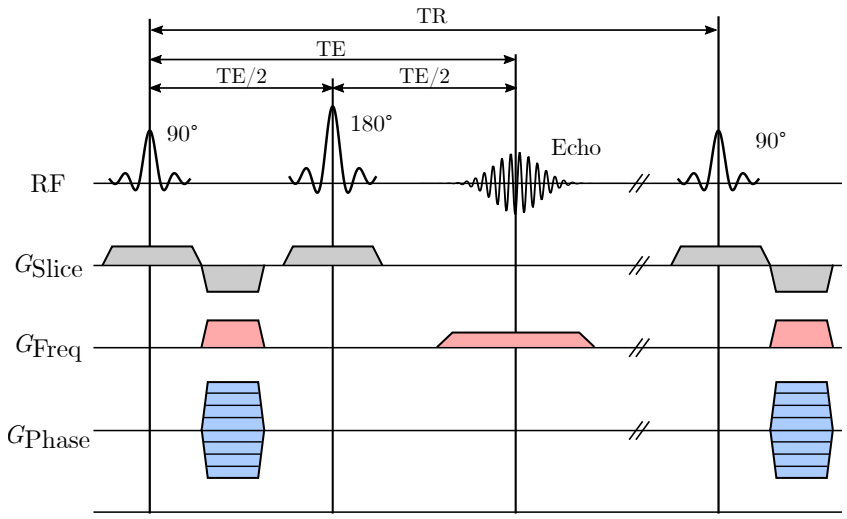

FIGURE 2.8: **Spin echo sequence.** The basic spin echo pulse sequence diagram consists of a 90° RF-pulse followed by a 180° refocusing RF-pulse that causes the echo formation at the echo time TE. The slice selective gradient G_{Slice}, the pre-winding frequency encoding gradient G_{Freq} and the phase encoding gradient G_{Phase} are typically applied simultaneously. After a second slice selective gradient with positive polarity is applied during the 180° refocusing pulse, the read-out gradient is employed during the echo generation before the spins are excited by the next 90° RF-pulse after the repetition time TR. For simplicity, the 90°-180° RF-pulse scheme used for this figure, but RF-pulses with arbitrary flip angles could be used instead. Adapted from [65].

echo amplitude is determined by the present T_2^*-decay. A basic GRE sequence pulse diagram is presented in Figure 2.9. Similar to the SE sequence diagram in Figure 2.8, the sequence and each repetition starts with the excitation pulse with a flip angle α_{Flip} along with the simultaneous application of the slice selection gradient, followed by the slice selective rephasing gradient together with the phase encoding gradient and the dephasing frequency encoding gradient that accelerates the magnetization decay. Applying the read-out gradient with opposite polarity to the dephasing gradient causes reversion of the spin dephasing and thus the acquisition of the formed GRE [61]. To acquire the full MR image, the process is again repeated for different phase encoding gradients.
While GRE imaging offers the possibility for fast imaging compared to SE imaging, GRE sequences are affected by susceptibility changes at air-tissue interfaces that result in local magnetic field inhomogeneities. These artifacts would be present as signal voids in the MR image [65].

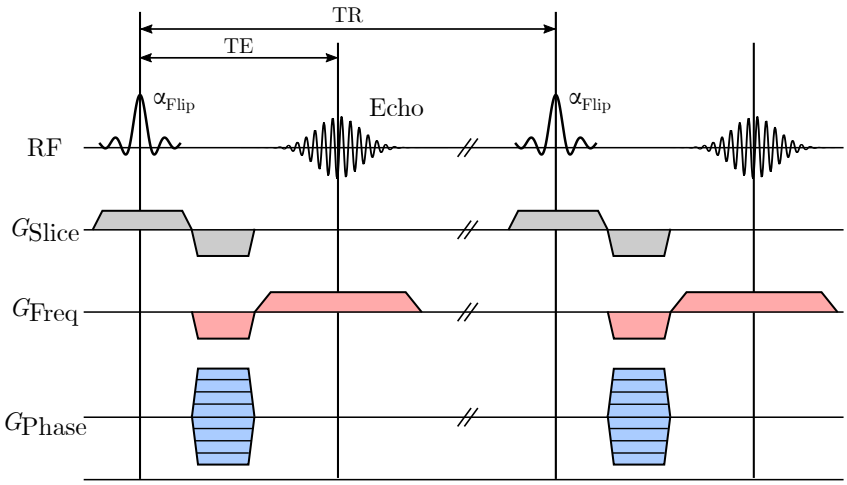

FIGURE 2.9: **Gradient echo sequence.** Instead of a 180° refocusing pulse as in the spin echo sequence, the basic gradient echo sequence comprises only a single RF-pulse with flip angle α_{Flip} per TR to form an echo after TE. After the application of the slice selective gradient G_{Slice} during the RF-pulse, the rephasing slice selective gradient is typically played at the same time as the dephasing frequency encoding gradient G_{Freq} and the phase encoding gradient G_{Phase}. The read-out gradient along the frequency encoding direction is utilized during the echo generation. Adapted from [69].

Balanced Steady-State Free Precession Sequence

A commonly used subtype of fast GRE sequences is the balanced steady-state free precession (bSSFP) sequence. Reducing the TR to accelerate the acquisition to a value below the T_2 of the tissue means that a full recovery of the longitudinal and the transversal magnetization is not possible. Hence, the equilibrium magnetization M_0 is not reached between two consecutive RF excitation pulses [68]. However, after a few RF pulses, the complex superposition of different longitudinal and transversial magnetization components approaches a steady-state, in which the "new" equilibrium magnetization M_{SS}, i.e., a stationary value in the amplitude, is reached [70]. Even though there exist other types of steady-state GRE sequences, in case of the bSSFP sequence, the net gradient moments over one TR, by definition, have to be "balanced" to zero. With this, all the available magnetization is efficiently reused for the signal generation, which in turn leads to a high signal-to-noise ratio (SNR) [68]. A basic bSSFP sequence diagram is illustrated in Figure 2.10. While the process from the first RF excitation pulse to the read-out of the echo is similar to the process described in the previous section for the basic GRE, additional gradients have to be applied in the bSSFP sequence to ensure that all gradient moments are balanced. After the application of the read-out gradient, the dephasing frequency encoding gradient is employed again simultaneously with a phase encoding gradient

of same amplitude as used prior to the read-out but with opposing polarity. At the same time, the slice selection for the next TR is prepared by applying the pre-phasing slice selective gradient followed by the slice selection gradient. Flip angle alternation between $+\alpha_{\text{Flip}}$ and $-\alpha_{\text{Flip}}$ in subsequent TRs has been shown to maximize the signal amplitude [70].
While different weightings are achievable with SE and GRE sequences, the bSSFP generates a combined T_2/T_1-weighting, which makes it ideal for cardiac imaging as well as functional or morphological imaging [70]. In general, the image contrast of a bSSFP sequence is, in addition to TE and TR, also influenced by the flip angle [68]. Despite its strong sensitivity to local field inhomogeneities or regional susceptibility differences that can result in so-called banding artifacts, the bSSFP sequence enables, due to short TR and TE, high temporal resolution and SNR imaging and is robust against motion and flow. It is therefore widely used for cine imaging [71].

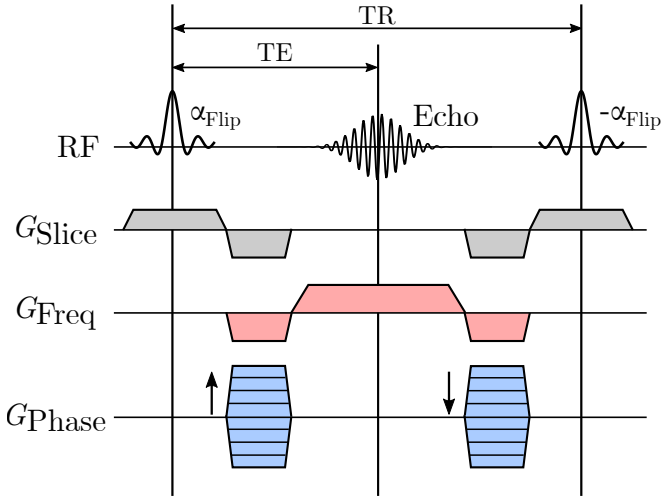

FIGURE 2.10: **BSSFP sequence.** A typical bSSFP sequence diagram with alternating RF pulses with flip angle α_{Flip} is depicted. All applied gradient fields, G_{Slice}, G_{Freq} and G_{Phase} are compensated within one TR in order to balance the magnetic gradient moment. Adapted from [70].

Turbo Spin Echo Sequences

One problem of the basic SE sequence is that the generation of a single echo from one RF excitation pulse for the read-out of a single line in k-space results in long scan times. To speed up the acquisition, fast or turbo spin echo (TSE) sequences have been developed that generate several SEs by the repeated application of 180° refocusing pulses after one single excitation pulse and the utilization of different phase encoding gradient strengths for each of the resulting echos [65]. Depending on whether multiple (multi-shot) or only one (single-shot) excitation pulse is employed to acquire the full MR-image, it is differentiated between fast SE and TSE sequences,

respectively. In order to decrease potential image blurring, caused by the strong echo intensity decay over the long echo train in single-shot TSE, the conjugate Fourier symmetry can be utilized in form of the half-Fourier scheme [65, 72]. A basic TSE sequence diagram is presented in Figure 2.11 (A), while subfigure (B) illustrates the half-Fourier scheme, where typically slightly more than half of the k-space is acquired. The single-shot cartesian acquisition is also known as echo-planar imaging.
Due to the resulting long TRs, the MR images acquired with TSE sequences show a pronounced T2-weighting [65].

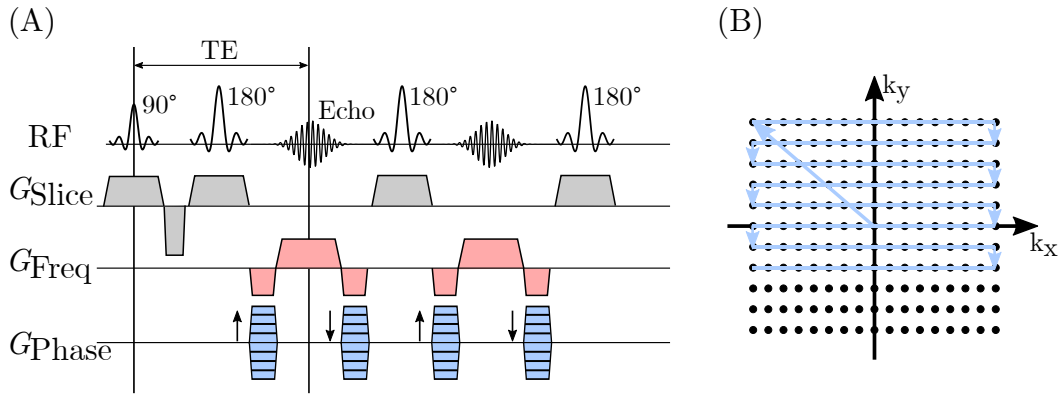

FIGURE 2.11: **HASTE sequence.** In Subfigure (A), the sequence diagram for a basic turbo spin echo sequence is shown, where the entire k-space is acquired after a single 90° RF-pulse, followed by a train of 180° refocusing RF-pulses. Subfigure (B) depicts the k-space acquisition scheme used for the half-Fourier acquisition single-shot turbo spin echo (HASTE) sequence, an echo-planar sampling strategy that utilizes phase-conjugate symmetry. Adapted from [73].

2.3 Advanced MRI Techniques

MRI offers, due to its versatility, not only opportunities regarding anatomical or morphological imaging but also quantitative and functional imaging. Even though there exist multiple methods and approaches, in the following, only two, the FD along with its extension non-uniform Fourier decomposition (NuFD) (Section 2.3.1) and T2-mapping (Section 2.3.2) are described as they found application in the generation of the results presented in this thesis.

2.3.1 Ventilation and Perfusion Imaging with Fourier Decomposition (FD)

Apart from morphological imaging, functional imaging to assess ventilation and perfusion plays an increasing role in lung imaging. In order to avoid the need for contrast agents such as gadolinium in dynamic contrast-enhanced MRI or inhalation of hyper-

polarized (noble) gases such as ^{3}He, ^{129}Xe and ^{19}F in non-proton-based lung imaging, the FD technique has been introduced as non-contrast-enhanced free-breathing alternative for 2D imaging.
During the breathing process, the lung or especially the lung parenchyma undergoes density changes. In inspiration, the external intercostal muscles, the abdominal muscles and a contraction of the diaphragm cause the volume of the thorax, the lung and the lung alveoli to increase with increasing air flow [30]. Concurrently, the density of the local lung parenchyma is decreased and increases again during expiration caused by contraction of the external intercostal muscles and relaxation of the diaphragm. As these periodic parenchymal density changes basically correspond to periodic proton density changes, this results in periodic changes of the measured MRI-signal intensity $S_V(t)$, mathematically described by [30, 74]:

$$S_V(t) = S_0 - A_V \cos^{2b_V}\left(\frac{\pi t}{\tau_V} - \varphi_V\right) \tag{2.45}$$

with S_0 being the baseline signal intensity, A_V the amplitude of the ventilation cycle, b_V the curve shape determining parameter, τ_V the period and φ_V the phase of the ventilation cycle.
In addition to the breathing-related signal changes, the signal in the lung is also periodically influenced by the heart beat. Using a bSSFP sequence (Section 2.2.5), these cardiac- or perfusion-related signal changes are caused by the so-called time-of-flight effect, which is also known as flow-related enhancement [75]. Due to subjecting the lung tissue/vessels to repeated RF-pulses without full recovery of the longitudinal magnetization, a steady state is reached in magnetization and the present spins are therefore partially saturated. The periodic inflow of blood into the imaging region from not excited regions, results in an inflow of unsaturated spins that are newly excited by the RF-pulses and therefore provide a higher signal. Considering both physiological processes, the observed signal intensity transforms from Equation 2.45 to:

$$S_{\text{total}}(t) = S_0 - A_V \cos^{2b_V}\left(\frac{\pi t}{\tau_V} - \varphi_V\right) + A_Q \sin^{2b_Q}\left(\frac{\pi t}{\tau_Q} - \varphi_Q\right) \tag{2.46}$$

with A_Q being the cardiac cycle's amplitude, b_Q the parameter determining the cardiac curve's shape as well as τ_Q and φ_Q being period and phase of the cardiac cycle. An exemplary signal curve based on Equation 2.46 is visualized in Figure 2.12 (A). With a typical breathing rate at rest of 9-24 breaths per minute (0.15-0.4 Hz) [76] and a heart rate of 60-90 beats per minute (1.0-1.5 Hz) [77], both processes occur on different time scales. Based on this, the basic idea of the FD method is to separate the signal contributions stemming from the breathing and the heartbeat from each other by means of Fourier analysis. For this, an image series is acquired in free-breathing with a sampling/imaging rate of at least double the frequency of the highest frequency component (Nyquist criterion) [30]. In order to allow for a voxel-wise analysis, the free-breathing image series requires deformable image registration,

explained in detail in Section 2.7.2, to ensure voxel alignment over the breathing cycle. After image registration, the voxel-wise signal over the examined time course is Fourier transformed to represent the acquired signal in terms of its frequency components as visualized in Figure 2.12 (B). As the full signal exceeds the representation as a single sinusoidal but consists of several sinusoidal components, harmonics corresponding to different Fourier coefficients are generated and observed in the Fourier spectrum as peaks with lower amplitude at integer multiples of the main frequency [30]. If the Nyquist criterium is not fulfilled and the sampling/imaging frequency is lower than the highest frequency component, harmonics of the cardiac signal are aliased into the spectrum.
The voxel-wise application of a signal filter allows signal separation into components corresponding to ventilation (Vent) and perfusion (Perf) that can be presented in respective maps showing the relative local parenchymal density changes (ventilation) and the relative pulsation of the blood (perfusion). The value in each voxel of the maps $\Gamma_{i,j}$ are calculated by summing the magnitude of the signal's fast Fourier transform ($\mathcal{FFT}(S_\Gamma)$) over the respective peak frequencies f_Γ with Γ =Vent, Perf:

$$\Gamma_{i,j} = \sum_{f_\Gamma} |\mathcal{FFT}(S_\Gamma)|. \tag{2.47}$$

The peak frequencies are determined from the FFT of the average signal over all lung voxels. With Equation 2.47, local, diseased lung regions with qualitatively lower density and/or lower blood pulsation with respect to the whole lung parenchyma are identifiable [31].

Non-uniform Fourier Decomposition

As the FD method depends on the spectral separation of the signal Fourier transforms and in turn the magnitude of the Fourier transform, signal frequency variations, due to, e.g., random irregular breathing or cardiac arrhythmia, over the acquisition period can lead to signal loss. One method that has been introduced to compensate for these frequency variations is the NuFD technique. The basic principle of the NuFD approach is to generalize the FD by using the NuFFT instead of the FFT. Using the NuFFT allows to calculate the frequency representation of non-equidistantly sampled signals. In the NuFD technique, this is utilized by converting the acquired signal $S_{\text{total}}(t_n)$ with potentially varying frequency into a virtual signal $\tilde{S}_{\text{total}}(\tilde{t}_n)$ with constant frequency, but (virtual) non-uniform sampling times $\tilde{t}_n$. The sampling intervals $\Delta\tilde{t}_n$ between the virtual sampling times for the n-th sampling time point are defined by [31]:

$$\Delta\tilde{t}_n = \Delta t \, \frac{f(t_n)}{f_{\text{mean}}} \tag{2.48}$$

with the uniform sampling intervals Δt and $f(t_n)$ being the instantaneous frequency at t_n and f_{mean} the mean over the instantaneous frequencies at the sampling time points t_n. Several methods such as short-term Fourier transform, wavelet or synchrosqueezed wavelet transform exist to find the time-frequency representation of a signal

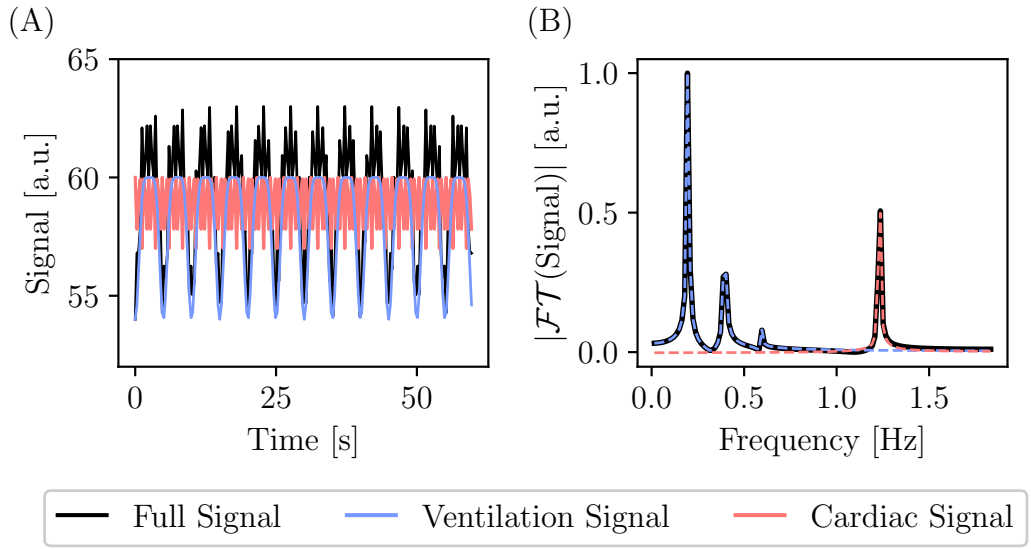

FIGURE 2.12: **Ventilation and perfusion signal.** Subfigure (A) shows the combined ventilation and perfusion signal simulated with Equation 2.46 (with $A_V = 6$, $b_V = 6$, $\tau_V = 5$, $A_Q = 3$, $b_Q = 4$, $\tau_Q = 0.8$, $\varphi_V = \varphi_Q = 0$) in black, along with the pure ventilation signal (light-blue) and perfusion signal (rose). In Subfigure (B), the magnitude of the frequency representations, i.e., the Fourier transform of the signals in (A), are depicted.

and thus the instantaneous frequency [78–80]. From Equation 2.48, the virtual sampling times are derived as:

$$\tilde{t}_n = \sum_{k=1}^{n} \Delta\tilde{t}_k = \frac{\Delta t}{f_{\text{mean}}} \sum_{k=1}^{n} f(t_k) \tag{2.49}$$

and used to calculate the NuFFT [31]:

$$\text{NuFFT}\left(\tilde{S}_{\text{total}}(\tilde{t}_n)\right) = \sum_{n=1}^{N} \tilde{S}_{\text{total}}(\tilde{t}_n) \exp\left(\frac{-2\pi i k \tilde{t}_n}{\tilde{t}_N - \tilde{t}_1}\right) \tag{2.50}$$

based on which the spectral separation and ventilation and perfusion map generation is performed similar to the FD method.

2.3.2 T_2-Mapping

T_2-weighted imaging is, as mentioned before, one of the main MRI image contrast generation mechanisms making use of the tissue-dependent spin-spin relaxation time and is specifically sensitive to the underlying tissue structure and composition as well as present water content and iron levels [81]. Based on this, T_2-weighted imaging

has been applied to identify collagen content, inflammation and edema as well as hemorrhage in the heart, myelin content in the brain and iron content in the liver, as these appear bright in T_2-weighted images [81]. One problem of MRI in general is the dependency of the acquired signal on hardware and specifically on the type of coils and their application along with the homogeneity of the static magnetic field, which results in a large variability over different MRI-scanners and even on a scan-to-scan basis. As this hinders the direct comparison of purely weighted images and use of these images for accurate area-at-risk definition and delineation in many applications, T_2-mapping has been introduced as quantitative extension. The principle of T_2-mapping is to retrieve the absolute tissue-specific T_2, by acquiring the signal in terms of T_2-weighted images at multiple TEs in order to model the signal given by:

$$S = S_0 \exp\left(-\frac{\mathrm{TE}}{T_2}\right) \tag{2.51}$$

with S_0 basically being the proton density. Voxel-wise fitting of this signal with an exponential curve, allows to extract the T_2 relaxation time on a voxel-by-voxel basis. This principle is illustrated in Figure 2.13. To reduce the computational complexity, Equation 2.51 is usually linearized to:

$$\ln(S) = \ln(S_0) - \frac{1}{T_2}\mathrm{TE} \tag{2.52}$$

and linearly fitted accordingly to obtain T_2.

For the acquisition of T_2-weighted images and in turn T_2-maps, long TEs and long TRs are employed in order to mitigate the influence of the T_1 relaxation process. In order to avoid the influence of static magnetic field or the susceptibility-induced inhomogeneities and in turn the acquisition of the T_2^* relaxation time, spin echo sequences are typically utilized to acquire the true T_2 relaxation time. Even though sequences specifically dedicated to T_2-mapping have been introduced making use of T_2-preparation pulses in combination with bSSFP readout, T_2-mapping can be similarly performed on T_2-weighted images acquired by repeatedly using the same sequence, but with varying TEs.

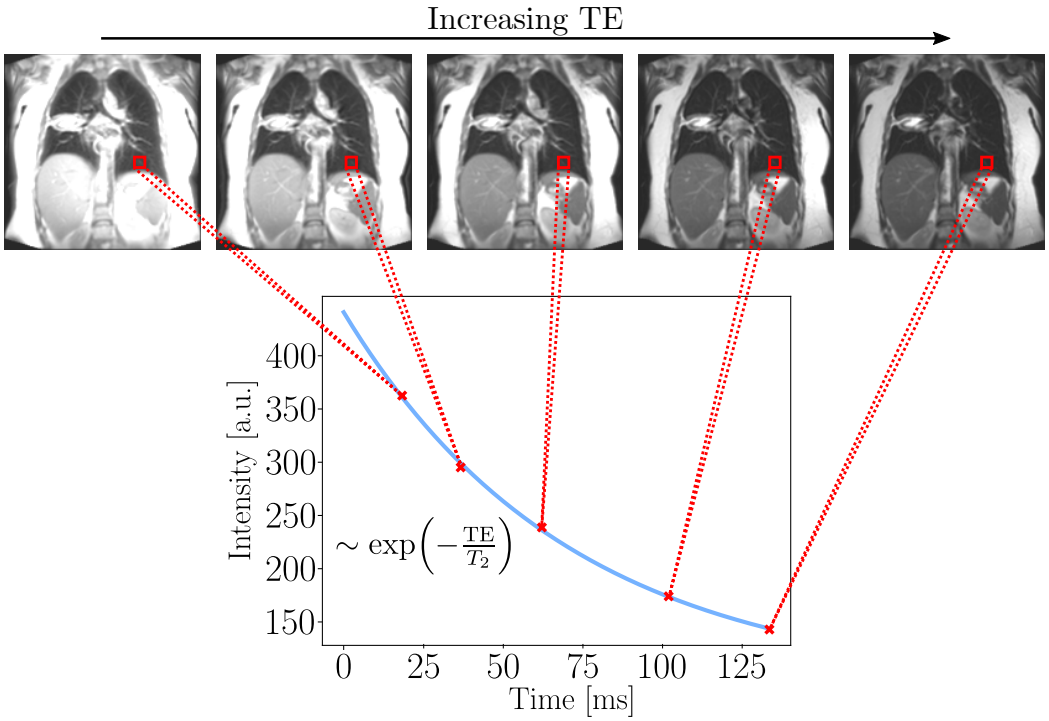

FIGURE 2.13: ***T_2*-mapping principle.** After aligning the different T_2-weighted images using deformable image registration (Section 2.7), the intensity found in each voxel is plotted against the utilized echo time TE. Using an exponential decay of the form shown in Equation 2.51, the decrease in intensity over time is fitted and the tissue-specific T_2 is extracted.

2.4 Photon Radiotherapy

Photon radiotherapy is one of the main cancer treatment approaches. By irradiating the patient with high energy photons, photon radiotherapy aims at sterilizing the cancer cells through cell damages triggered by photons depositing energy followed by interaction with tissues. This section gives an overview over these interactions of photons with matter (Section 2.4.1) and the basic treatment planning workflow in Section 2.4.2. Along with an introduction to radiobiology concepts in Section 2.4.3 and to treatment delivery techniques in Section 2.4.4, a description of stereotactic body radiotherapy (SBRT) (Section 2.4.5) followed by image-guided radiotherapy (IGRT) (Section 2.4.6) is given. The section ends with an explanation of the current treatment standard in lung radiotherapy (Section 2.4.7).

2.4.1 Photon Interactions With Matter

Photons in the energy range of about 10 keV to 10 MeV, as used for medical imaging and radiotherapy, interact with matter, i.e., the atoms, in different ways depending

on the photon energy and the properties of the atom, in particular the atomic number Z. The three most relevant interactions are:

- **Photoelectric Absorption:** Photon is absorbed by atom and atomic electron is emitted
- **Compton Scattering:** Photon inelastically scatters from atomic electron and transfers a part of its energy to this electron, which is emitted from the atom as a result
- **Pair Production:** Photon in the electric field of atom nucleus generates an electron-positron pair

A schematic visualization of the effects is given in Figure 2.14. In the photon energy range of 4-15 MeV used for external beam radiotherapy, the most prominent effect is the Compton scattering [53]. The locally absorbed energy via these processes per mass defines the dose, the main quantity in radiotherapy. The absorbed energy dose D is therefore given as [50]:

$$D = \frac{\mathrm{d}\bar{\epsilon}}{\mathrm{d}m} \tag{2.53}$$

with $\bar{\epsilon}$ being the mean locally absorbed energy in matter with mass m. This dose is deposited in matter through indirectly ionizing radiation, i.e., the electrons that are generated via the interaction mechanisms described above. A more detailed description of the photon-matter interactions and a derivation of the dose definition is, among others, given in Schlegel et al. [53].

2.4.2 Treatment Planning Workflow

The workflow after a patient was chosen to undergo radiotherapy mainly consists of five steps that will be briefly explained in the following. A more concise description is found, e.g., in Schlegel et al. [53].

Baseline Imaging The first step in the treatment workflow is to acquire images from one or more imaging modalities to assess the geometrical position and volume of the tumor and the surrounding organs at risk (OARs) that have to be spared during RT. In most radiotherapy approaches, CT-scans are a key component, as information on the photon energy absorption of the different tissues are derived from the obtained CT numbers for the dose calculation planning (step 4).

Segmentation of Target and OARs Based on the baseline images, the tumor or target is delineated along with the OARs and the isocenter is defined. In order to incorporate potential uncertainties regarding tumor extent, patient positioning and motion as well as dose delivery, additional target volumes using margins are defined based on international recommendations. In general, four different target volumes are considered and schematically visualized in Figure 2.15:

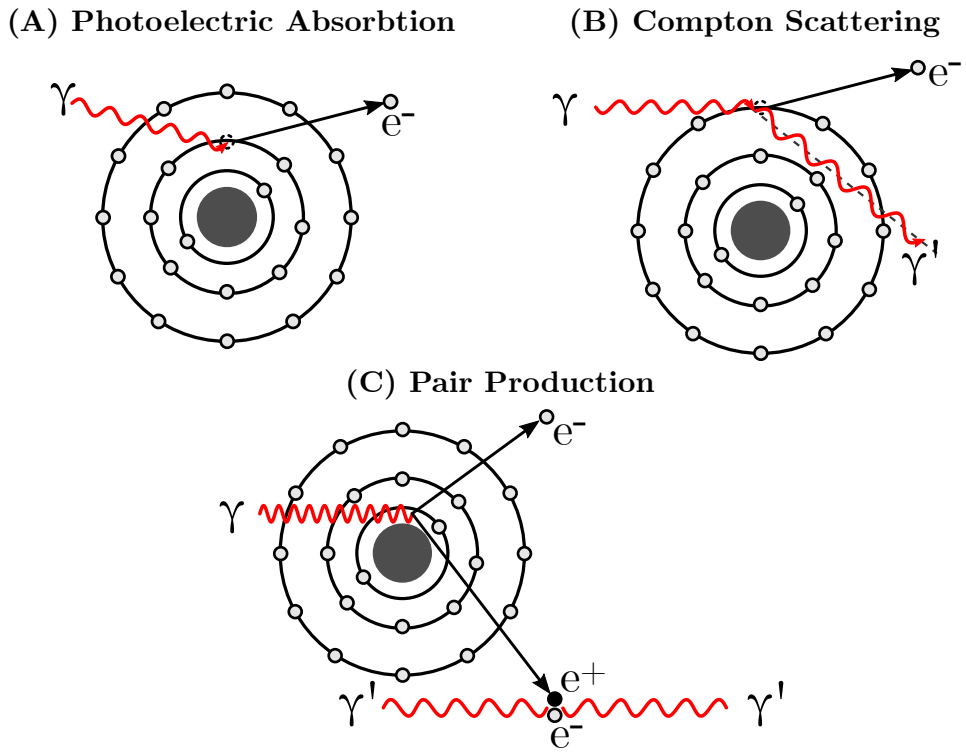

FIGURE 2.14: **Photon interactions with matter.** This schematic depicts the three most relevant interaction processes between photons and matter made up of atoms, namely the photoelectric absorption, i.e., the photon absorption and electron emission, in Subfigure (A), the Compton scattering, i.e., the inelastic scattering of a photon on an electron in (B) and the pair production, i.e., the generation of an electron-positron pair from a photon in (C). Adapted from [53].

- **Gross Target Volume (GTV):** Visible tumor that is distinguishable from normal tissue
- **Clinical Target Volume (CTV):** Extension of the GTV to incorporate microscopic tumor infiltrations into normal tissue
- **Internal Target Volume (ITV):** Extension of the CTV to compensate internal motion
- **Planning Target Volume (PTV):** Extension of the ITV to take uncertainties in the exact patient positioning and overall uncertainties in the dose delivery into account

Agreement on Radiotherapy Approach Depending on the tumor type and location as well as the patient history or treatment outcome (curative vs palliative),

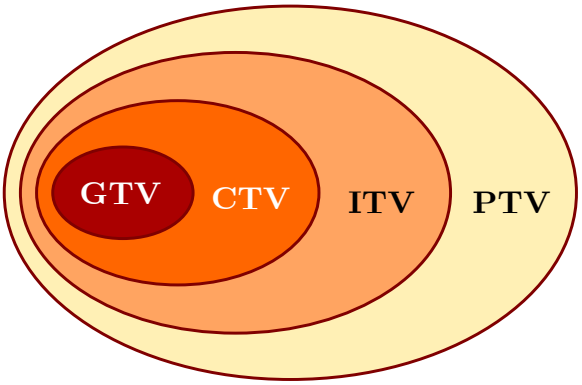

FIGURE 2.15: **Target volume definitions.** The gross tumor volume (GTV), i.e., the delineation of the visible tumor, is enveloped by the clinical target volume (CTV) containing additional microscopic tumor infiltrations. In order to compensate for internal motion, the CTV is, often anisotropically, extended to form the internal target volume (ITV), which is further extended to the planning target volume (PTV) to incorporate potential uncertainties in patient positioning and dose delivery. Adapted from [53].

the radiotherapy approach, the treatment delivery technique and the target dose and dose fractionation (explained in Section 2.4.3) are decided. Different treatment delivery approaches are presented in the Sections 2.4.5 and 2.4.4. A more detailed description on the specifics of radiotherapy for lung lesions is given in Section 2.4.7.

Dose Calculation and Optimization Dose calculation is understood as a simulation of the spatial distribution of the dose per volumetric element (voxel) in the patient. The number of radiation beams, their angles/directions and their intensity and shape are optimized with the goal to deliver the prescribed dose to the target and minimize the dose to the surrounding healthy/normal tissue and the OARs. With this, the tumor control should be maximized and the normal tissue complications minimized [53].

Treatment Once the dose plan is optimized and verified by a medical physicist and a radiation oncologist, the plan is delivered to the patient in a pre-defined number of treatment fractions (Fxs). To account for differences in patient positioning and/or anatomical changes between or during a treatment Fx, image-guided radiotherapy (Section 2.4.6) together with an offline- or online-adaptive workflow (Section 2.5.3) can be used.

2.4.3 Radiobiology

The exact impact of the radiation depends on the properties of the radiotherapy treatment, i.e., the treated organ and its properties, the dose and the type of radiation. In general, the radiation effect is divided into the physical, the chemical and the biological phase. While the first two describe the more immediate interactions of the radiation with the irradiated tissue, meaning damaging of the cell DNA, membrane and organelles, the biological phase is concerned with the more long-term enzymatic reactions and regulations processes of the cell, i.e., cell reparation, proliferation and death. The main goal of radiotherapy is to induce damage to tumor cells that leads to the death of the cells directly (pre-mitotic) or after one or two cell divisions (post-mitotic). The principles for the quantification of the impact of radiation dose on tissue have been developed in in-vitro experiments using clonogenic assays where the number of clonogenic cells (cells that can proliferate to form a colony) are determined after being irradiated with different doses. Based on the empirical observations, the linear-quadratic (LQ) model has been introduced to describe the cell survival fraction (SF) of the number of surviving cells N_{surv} to the total number of irradiated cells N_{rad} [53]:

$$\text{SF}(D) = \frac{N_{\text{surv}}}{N_{\text{rad}}} = \exp\left(-\alpha D - \beta D^2\right) \tag{2.54}$$

with the model parameters α and β representing the cell's sensitivity to the used radiation. Biologically, lethal cell damage induced by one radiation particle is expressed by the linear term, while the lethal cell damage induced by two independent, sublethal particle-tissue interactions is characterized by the quadratic term. Based on this, the so-called $\frac{\alpha}{\beta}$-ratio is defined as a measure for the capacity of the cells to repair radiation-induced damage such as single- or double-strand DNA breaks.
Even though a delivery of the total dose at once is in some cases possible, typically, a fractionated treatment, i.e., the delivery of smaller doses over several treatment sessions is performed and is considered the main form of modern radiation therapy treatment [53]. Fractionation makes use of the fact that the DNA repair capability of normal tissue is superior to the the tumor tissue repair processes. Hence, normal tissue cells benefit from a repeated delivery of smaller radiation doses over several days, due to the repair of radiation-induced cell damage from one to the next treatment. With this, radiation-induced toxicities in the healthy tissue and corresponding potentially long-term radiation-induced tissue damage are reduced, while the tumor cells are lethally damaged [82]. The general goal of fractionated RT is to maximize the therapeutic window, i.e., to maximize the damage to the tumor cells, but to minimize overall normal tissue damage at the same time. Whereas in conventional fractionated radiotherapy total doses of 40-70 Gy are delivered with daily fractions of 1.8-2 Gy over several weeks, in hypofractionated radiotherapy, fractionated doses of more than 2 Gy are delivered within one ore two weeks. Hypofractionated RT is particularly advantageous if the α/β-ratio in the tumor is smaller compared to the normal tissue or if the doses can be precisely deposited in the target with the aid of,

e.g., image-guided radiotherapy (Section 2.4.6). The effect of two different fractionation schemes on two different α/β-ratios according to the LQ model is illustrated in Figure 2.16.

In order to assess the effectiveness of different hypofractionated RT schemes in com-

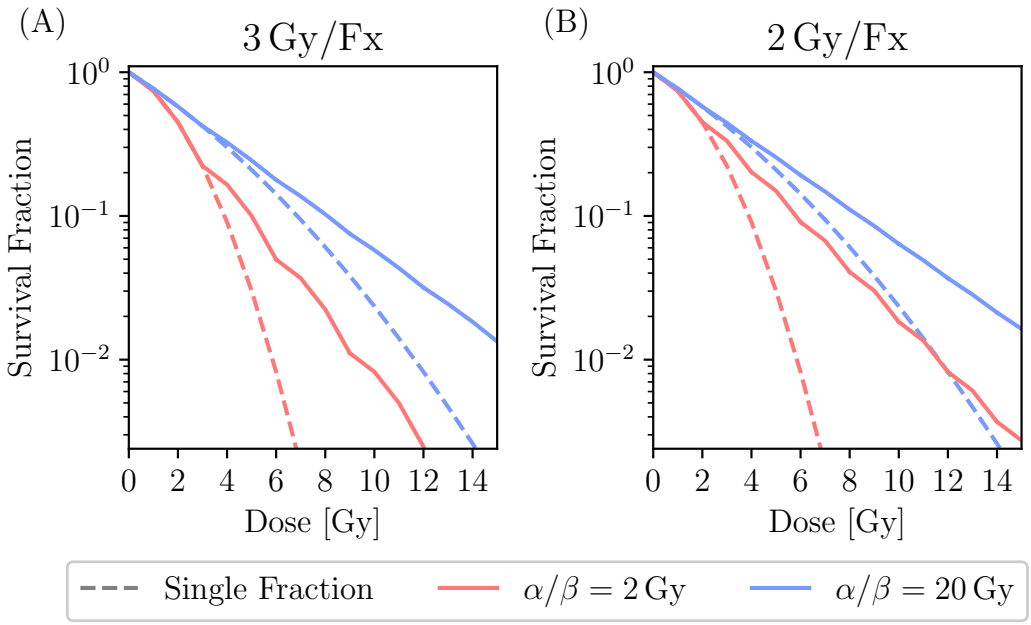

FIGURE 2.16: **Illustration of the linear quadratic model.** The cell survival fractions for a 3 Gy/Fx fractionation scheme (Subfigure (A)) and a 2 Gy/Fx are shown for tissues with two different α/β-ratios (2 Gy in red and 20 Gy in blue) in case of a fractionated treatment (solid line) and a single fraction (dashed line). Adapted from [53].

parison with conventional RT, the dose distributions are converted into equivalent doses in 2 Gy fractions (EQD2) [83]:

$$\mathrm{EQD2} = D \cdot \frac{D_{\mathrm{frac}} + \frac{\alpha}{\beta}}{2 + \frac{\alpha}{\beta}} \tag{2.55}$$

with D_{frac} being the dose per fraction. Additionally, the biological effective dose (BED) is calculated with:

$$\mathrm{BED}_{\alpha/\beta} = \mathrm{EQD2} \cdot \left(1 + \frac{2\,\mathrm{Gy}}{\frac{\alpha}{\beta}}\right) = D \cdot \left(1 + \frac{D_{\mathrm{frac}}}{\frac{\alpha}{\beta}}\right). \tag{2.56}$$

2.4.4 Treatment Delivery Techniques

There are several different methods to deliver the radiation dose to the patient. Commonly used devices are Linacs that produce beams of high-energy photon radiation.

With these devices, multiple overlapping radiation beams can be used in the dose optimization stage in conventional RT to generate a regularly shaped high-dose region centered at the target. As this approach exposes potentially large parts of surrounding normal/healthy tissue with high radiation doses, which can result in severe tissue damage and toxicities, a more accurate technique has been introduced with conformal radiotherapy. For this, the radiation beams are shaped to the target contour by optimizing the number of used beams and by employing a multi-leaf collimator (MLC) to shield the normal surrounding tissue from the beams, which are individually shaped to match the target volume in beam's eye view. With intensity-modulated radiation therapy (IMRT) and volumetric-modulated arc therapy (VMAT), two extensions of conformal radiotherapy have been developed and established in the clinical treatment routine [53, 84].

Intensity-Modulated Radiation Therapy (IMRT)

In addition to the usage of MLCs for lateral beam shaping, in IMRT the target conformality is improved by the utilization of a non-uniform beam intensity. By subdivision of each radiation beam into a number of beamlets, the intensity of each beamlet is made adjustable and therefore allows a more precise shaping of the beams to the target. This is especially advantageous for the treatment of complex target shapes and/or OARs in close proximity to the target. Due to the achieved steep dose gradients, i.e., strong dose fall-offs, with this technique, the surrounding normal tissue and OARs are further spared from the high doses [84]. In contrast to conventional RT, the dose distribution for IMRT treatments is inversely planned, meaning that a planning software is used that optimizes the beam characteristics until pre-defined dose requirements and limits to target and OARs are reached [85].

Volumetric-Modulated Arc Therapy (VMAT)

Since IMRT typically results in longer treatment times as radiation beams from different fixed angles are delivered consecutively with the beam being off during Linac gantry motion, a more time-efficient approach has been established with VMAT. The idea of VMAT is that the radiation dose is applied as a cone beam while the Linac gantry is continuously rotated around the patient. The intensity modulation in a VMAT treatment is achieved by a variable gantry rotation speed, a variable dose rate and dynamically adjusted MLCs [85].

2.4.5 Stereotactic Body Radiotherapy (SBRT)

One radiotherapy approach, that has been established as standard treatment for medically inoperable stage I NSCLC and has found application in more and more treatment sites, is the SBRT. SBRT describes a high-precision external beam RT approach to deliver high radiation doses to extracranial targets [7, 86]. The aim of SBRT is to deposit high radiation doses (about 48-60 Gy) in the target in about 1-5

Fx or up to 10 Fx (within two weeks) depending on the definition, while minimizing the dose deployed in the surrounding normal tissue [86]. For this, a high conformality to the target is necessary and is achieved again by using MLCs to shape the beam to the target. The SBRT dose to the target boundaries (prescription isodose) is typically chosen to be around 60-80% of the maximum, typically inhomogeneous target dose. This leads to high dose gradients at the target-normal tissue interface, which is further facilitated by the utilization of the previously described IMRT or VMAT methods that allow to further adjust the photon beam.
An important element for the safe and efficient application of SBRT is management of tumor motion to minimize the radiation field size and target margins and thus to further limit the normal tissue extent subjected to the high dose. Depending on the patient, the treatment is therefore usually delivered in multiple breath-holds or in tidal breathing. Large breathing amplitudes can be further restricted with the usage of an abdominal compressor or accounted for by a respiratory gated beam delivery. This has been fostered by the integration of different kinds of imaging devices into the radiotherapy treatment device and the introduction of IGRT [7, 86].

2.4.6 Image-Guided Radiotherapy (IGRT)

As mentioned before, exact and reproducible patient positioning between planning and first Fx as well as over several treatment Fx is an integral element to ensure a safe dose delivery and is one of the main components of IGRT. For this, imaging modalities such as CBCT or MRI have been integrated into the treatment device for pre-treatment volumetric in-room imaging to position the patient and to assess potential inter-fractional changes, due to, e.g., the filling of hollow organs, tumor response or weight loss of the patient. In order to compensate for these inter-fractional changes, the treatment plan is adjusted, which is known as adaptive radiotherapy (ART). Depending on the available tools, the treatment plan is either adapted between fractions (time scale of hours or days) in offline ART or immediately prior to the dose delivery, while the patient remains in the treatment position, in online ART [87]. As many tumor sites are affected by motion, optical surface imaging for patient surface motion tracking, ultrasound for internal volumetric imaging, X-ray imaging, partly in combination with fiducial markers or other landmarks, and cine MRI have been established for intra-fractional motion detection. In combination with the treatment plan adaptation, this motion detection using real-time or near real-time imaging allows a more precise dose delivery. A more detailed description of ART in the context of MRgRT is given in Section 2.5.3.

2.4.7 Lung Radiotherapy

Radiotherapy plays an integral part in the treatment of most patients with lung cancer or pulmonary metastases. SBRT serves as standard-of-care curative treatment for patients where surgical resection of the tumor (NSCLC stage I, II or pulmonary oligometastasis) or the respective lung lobe is not possible due to tumor location

or affected lymph nodes [5, 6]. As the RT dose description not only depends on the staging but also the location of the tumor, peripherally-located tumors, central (distance to tracheo-bronchial tree $< 2\,\text{cm}$) and ultra-central (distance from proximal bronchial tree $< 2\,\text{cm}$) tumors as well as metastases are differentiated [88]. For peripherally-located tumors, a $\text{BED}_{10} = 113\,\text{Gy}$ for the prescribed dose to the PTV is recommended, while for tumors with broad chest wall contact the recommended dose is reduced to $\text{BED}_{10} = 106\,\text{Gy}$. This results in a fractionation of $3 \times 15\,\text{Gy}$ and $4 \times 12\,\text{Gy}$, respectively [89]. The most commonly used fraction schemes for ultra-central lung tumors are $5 \times 10\,\text{Gy}$, $8 \times 7.5\,\text{Gy}$ and $12 \times 5\,\text{Gy}$ with a $\text{BED}_{10} = 52.5$-180 Gy [90]. Recommended fractionations are 8×7.5 Gy for ultra-central and 5×10 Gy for central tumors [91]. The dose recommendation for peripheral and central lung metastasis is a $\text{BED}_{10} \geq 100\,\text{Gy}$, whereas for ultra-central metastasis, the dose should be reduced to $\text{BED}_{10} \geq 75\,\text{Gy}$ [6]. In stage III NSCLC patients, RT with concurrent chemotherapy is considered the standard curative treatment approach. As a majority of those patients suffer from large tumor volumes and/or poor performance status, palliative RT with lower doses is recommended. Similarly stage IV NSCLC patients benefit from palliative RT to relieve symptoms and to improve the overall quality of life. Additionally, curative RT for present oligometastases has been shown to lead to long-term survival [5].

Apart from application in the treatment of NSCLC, RT is also routinely used in the disease management of small-cell lung cancer (SCLC) patients of stage I-III, but is mainly employed for palliative care of primary tumor or metastases in stage IV SCLC patients [5].

The lung parenchyma is very sensitive to radiation and RT in lungs commonly induces toxicities, typical dose-volume constraints are to restrict the volume receiving more than 20 Gy (V20) to $\leq$ 10-15% and the mean lung dose (MLD) to $\leq 8\,\text{Gy}$ [92]. As lung tumors are affected by breathing motion, several motion management methods exist in the clinical practice for the safe delivery the respective SBRT doses to the tumor. The most common clinically used approach on standard Linac systems is the utilization of a 4D-CT and an ITV concept. For this, a 4D-CT is acquired in the planning stage and the ITV is defined to enclose the GTV in each breathing state [93, 94]. Typically an additional margin (8 mm in superior/inferior and 5 mm in other directions) is added to the ITV for the PTV used for the treatment in free-breathing, resulting in the irradiation of a large lung volume [94]. To reduce the margins for large tumors or large motion, a gated delivery can be performed in expiration or deep inspiration breath-hold. For this, only a CT should be acquired in breath-hold mode [94]. If in-room CBCT is available, it is used for precise patient positioning. Apart from the pre-treatment derived motion compensation, (tumor) motion monitoring or tracking based on X-rays or optical imaging is also emerging clinically. Using X-rays during the treatment in combination with implanted markers as surrogates to track the tumor motion, the tumor is only irradiated at a specific breathing phase in free-breathing or in deep inspiration breath-hold [95]. Besides the X-ray-based options that subject the patient to additional ionizing radiation and require the implantation

of markers in the latter case, optical imaging finds clinical application. For this, an external surrogate, e.g., a block with reflective markers, is placed on the patient's abdomen and illuminated with an infra-red camera to monitor the breathing motion in real-time [95]. As this method requires the motion of the external marker and the internal tumor motion to be correlated, additional X-ray imaging is utilized to improve this correlation. Furthermore, in order to ensure a reproducible breathing pattern, spirometer-based or abdominal compression are used to induce breath-holds or to restrict the breathing amplitude, respectively [96].
Apart from the treatment at standard Linacs, lung tumors have been increasingly treated with MRgRT at MR-Linacs, which allows, in addition to an online ART workflow, ionizing radiation-free as well as internal and external marker-free real-time tumor tracking for a precise dose delivery. This is described in more detail in the following sections.

2.5 Magnetic Resonance Image-Guided Radiotherapy (MR-gRT)

Combining photon radiotherapy devices with MRI-scanners to hybrid MR-Linacs has opened up new opportunities regarding precise dose delivery and anatomical adaption. This section starts with a brief introduction to the currently existing MR-Linac devices (Section 2.5.1). Section 2.5.2 focuses on the specifics of the Viewray MRIdian MR-Linac that was primarily used in this thesis, followed by this system's online-adaptive RT approach in Section 2.5.3 and the motion management in Section 2.5.4. Section 2.5.5 describes the specifics of lung imaging at the Viewray MRIdian MR-Linac.

2.5.1 MRI-Guided Linear Accelerator (MR-Linac)

Due to the difficulties of combining radiotherapy devices with charged particles with MRI-scanners, different magnet configurations have been developed with the photon beam being delivered either parallel or perpendicular to the static magnetic field direction. Additionally, to achieve conformal RT using different photon beam angles, either the beam is rotated around the patient (rotating gantry) or the patient is rotated around a static beam (rotating couch). Four different systems that combine an MRI-scanner with a Linac for radiotherapy treatment have been introduced [97]:

- **Viewray MRIdian:** 0.35 T MRI-scanner with a super-conducting split-bore magnet and a 6 MV Linac, perpendicular beam, rotating gantry, commercially available
- **Elekta Unity:** 1.5 T MRI-scanner with a closed-bore super-conducting magnet and a 7 MV Linac, perpendicular beam, rotating gantry, commercially available
- **MagnetTx Aurora RT** 0.5 T MRI-scanner with a high-temperature super-

conducting split-bore magnet a 6 MV Linac, parallel beam, rotating gantry, commercially available

- **Australian MRI Linac** 1.0 T MRI-scanner with a super-conducting split-bore magnet and a 6 MV Linac, parallel or perpendicular beam, rotating couch, research system

2.5.2 The Viewray MRIdian MR-Linac

The Viewray MRIdian MR-Linac system is comprised of an MRI- and a Linac system, whose details are given in the following. A photo of the MRIdian MR-Linac situated at the LMU University Hospital is given in Figure 2.17.

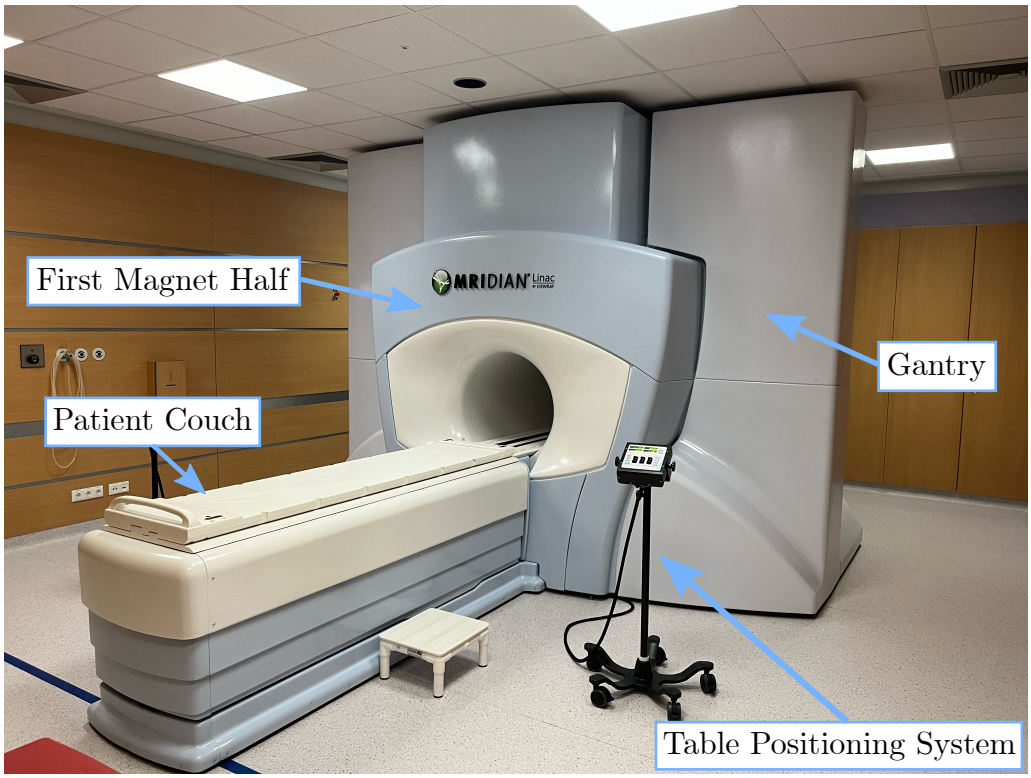

FIGURE 2.17: **Photo of the Viewray MRIdian MR-Linac.** The Viewray MRIdian system situated at Radiation Oncology Department of the LMU University Hospital with its patient couch, the table positioning system, the gantry and the visible first half of the MRI system's magnet is depicted. Own figure.

MRI System The 0.35 T Viewray MRIdian uses a split-bore magnet (double donut) configuration, where two superconducting magnet halves as well as the gradient coil are separated by a 28 cm wide gap and a bore diameter of 70 cm. A gradient

strength of 18 $\frac{\text{mT}}{\text{m}}$ and a slew rate of 200 T/m/s are achieved by the gradient system to image a 50 cm spherical FOV [98, 99]. To acquire the MRI-signal, a whole-body RF transmit coil along with two specifically designed surface receive coils, made up of low-density foam and containing radiolucent phased arrays with six channels for body and 5 channels for head and neck imaging each, are used. The receiver coils are placed anterior and posterior to the patient [99].

Linac System The Linac system (6 MV flattening filter free Linac, dose rate 600 $\frac{\text{cGy}}{\text{min}}$) is mounted in a circular, rotating gantry, which is placed in the gap between the magnet halves allowing the radiation beams to be delivered perpendicular to the static magnetic field [99]. Six cylindrical ferromagnetic shielding compartments were constructed upon the gantry to hold the Linac components and thus circumvent the interference of the magnetic field with the Linac and any disturbances of the MRI scanning by the Linac. To allow the delivery of conformal RT or SBRT, double-stack, double-focus MLCs consisting of a total of 138 tungsten alloy leaves (leaf width = 8.3 mm [99]) are fitted to the Linac [100]. Even though gantry angles between 30° and 33° are not possible because of technical limitations, the Linac system allows conformal and step-and-shoot IMRT radiotherapy treatments.

MR-Linac Laser System For the patient positioning, the treatment room is, as part of the device installation, equipped with a laser system that projects a virtual isocenter outside the bore [99]. The overall localization accuracy of the system was determined to be (1.0 ± 0.1) mm [100].

2.5.3 Online-Adaptive Radiotherapy

As already mentioned before, image-guidance and the possibility to acquire images at the beginning of each treatment Fx is the key component of online-adaptive radiotherapy. In MRgRT the procedure is as follows: After a first 3D MRI-scan at the MR-Linac during the planning phase, using a bSSFP sequence and an in-plane resolution of $1.5 \times 1.5\,\text{mm}^2$ with a slice thickness of 3.0 or 1.5 mm and a suitable FOV, is acquired (under breath-hold) in axial orientation, a CT-scan is performed in breath-hold and registered to the planning or baseline MRI-scan to obtain a planning synthetic CT and provide information on the tissue attenuation necessary for dose calculation and optimization. On each treatment day, the same patient positioning and the same MRI sequence is used to obtain images (setup scans) of the anatomy of the day. While the patient is in treatment position in the MR-Linac, the baseline MRI-scan is registered (basics of image registration can be found in Section 2.7) to the fraction (setup) MRI-scans and the respective target and OAR contours as well as the electron density information from the CT-scan are propagated respectively. After potential re-contouring of the propagated contours, the original dose plan is re-calculated based on the registered baseline synthetic CT. Depending on the quality of the predicted dose compared to the baseline planning dose, the plan is either

accepted or adapted, i.e., re-optimized using the initial optimization parameters and weights or using modified planning objectives. Once the adapted dose distribution is accepted by a radiation oncologist and a medical physicist, the patient is treated accordingly [97, 99].

2.5.4 Motion Management

In addition to an assessment of the anatomy on each treatment day and the subsequent adaptation of the dose plan to the present anatomy, MRgRT requires management or compensation of intrafractional motion such as breathing or peristaltism. For this, similar to the 3D image acquisition at the planning stage and for the MRI-scans at each Fx used to assess the anatomy of the day and to perform dose plan adaptation, a 2D bSSFP sequence is employed. With an in-plane resolution of $3.5 \times 3.5\,\mathrm{mm}^2$ (cartesian read-out) or 2.4×2.4 to $2.5 \times 2.5\,\mathrm{mm}^2$ (radial read-out) and slice thickness of 5, 7 or 10 mm, image series of one 2D slice intersecting the tumor in sagittal orientation is continuously acquired during treatment in real-time with a frame rate of 4-8 frames/s using cartesian or radial k-space read-out. Based on these 2D-cine images, the delineated target is tracked utilizing real-time deformable image registration. The treatment is performed in a gated fashion, meaning the radiation beam is only activated by the beam control if the tracked target is within a predefined boundary/margin with a predefined minimal confidence [98]. This principle is illustrated in Figure 2.18. For targets that are subject to breathing motion, the treatment is typically delivered in multiple breath-holds. This precise localization of the target in almost real-time (due to system latency), allows a reduction of the uncertainty margins added to the GTV and therefore a dose reduction in the normal tissue surrounding the target that potentially decreases the probability of radiation-induced toxicities.

2.5.5 Lung Imaging at the MR-Linac

One of the main challenges of MR imaging of the lung in general is its low tissue density, i.e., low proton density, resulting in a weak MR signal and thus a low SNR [101]. An increase of the magnetic field strength ($>3\,\mathrm{T}$) to increase the SNR, as has been the trend in, e.g., high-resolution brain imaging, poses additional challenges for lung imaging. Due to the lung's foam-like structure with multiple air-tissue interfaces formed by airways and alveoli, lung MRI is limited by short T_2^* times, i.e., a fast signal decay in GRE imaging caused by the magnetic susceptibility difference between the paramagnetic oxygen in the air and the diamagnetic tissue [102]. As these susceptibility-induced magnetic field inhomogeneities increase and thus the T_2^* times decrease with higher magnetic field strengths (2.11 ms at 1.5 T vs 0.74 ms at 3 T [103]), higher SNRs are typically not achievable at diagnostic MRI-scanners (≥ 1.5 T), without the use of ultra-short TE (UTE) or zero TE (ZTE) sequences, owing to the short TE required for the acquisition [101, 102]. Compared to diagnostic scanners, the MR-Linac employs a lower magnetic field strength of 0.35 T, which is

(A) **Target out, beam off** (B) **Target in, beam on**

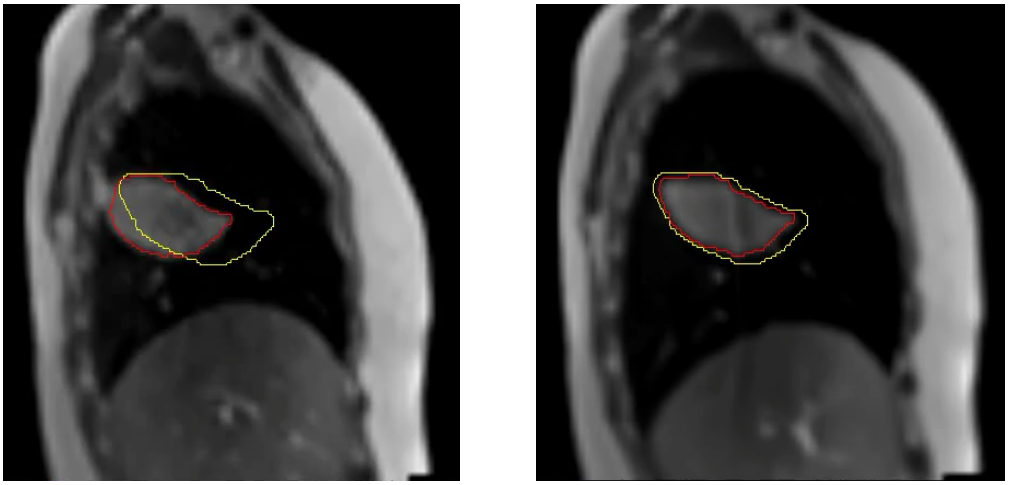

FIGURE 2.18: **Motion management at the MR-Linac.** In this figure, two different frames of the 2D cine-MRI scans acquired during the treatment are depicted with the tracked tumor boundary in red and the treatment position or gating boundary in yellow. Subfigure (A) shows the target out of the treatment boundary and thus in radiation beam-off mode. In Subfigure (B), the target is within the treatment boundary resulting in dose being delivered to the target. Own figure.

beneficial for lung imaging, as the susceptibility artifacts and off-resonance effects are reduced and T_2^* times prolonged ($\geq 8.2\,\text{ms}$) [103]. Lower magnetic field strengths also aid the bSSFP sequence used in this thesis for the image series acquisition required for the NuFD method (Publication I and II). Due to the sensitivity of the bSSFP sequence to field inhomogeneities [104], the reduced magnetic field inhomogeneities decrease the potential for the occurrence of banding artifacts. Besides that, it also benefits from a reduced specific absorption rate (SAR), i.e., the energy deposited into the tissue by RF-pulses that scales with the square of the magnetic field strength [105, 106]. The high flip angles (70-90°) and short TR necessary to achieve high signal amplitudes with the bSSFP sequence [107] can pose SAR problems on diagnostic scanners ($\geq 1.5\,\text{T}$).
One of the limiting factors of imaging (with a bSSFP sequence) at the MR-Linac is the gradient system. The use of a split-bore magnet compared to a closed-bore super-conducting magnet in clinical diagnostic scanners allows the Linac gantry to be mounted in the center of the MRI's FOV for RT but compromises the performance of the MRI gradient system. Current diagnostic 1.5 T MRI-scanners are equipped with gradients with a maximum amplitude $\geq 30\,\frac{\text{mT}}{\text{m}}$ and a slew rate $\geq 125\,\text{T/m/s}$ per gradient axis, i.e., the speed of the gradient system [108]. While the slew rate of the MR-Linac with $200\,\text{T/m/s}$ is the same as for the 1.5 T MRI-scanner (MAGNETOM Aera/SolaFit, Siemens Healthineers, Erlangen, Germany) used in Chapter 5, the

MR-Linac's maximum gradient amplitude of 18 $\frac{\text{mT}}{\text{m}}$ is much lower than the 45 $\frac{\text{mT}}{\text{m}}$ of the 1.5 T MRI-scanner. In 2D imaging, the achievable slice thickness at the MR-Linac is limited by the small maximum gradient amplitude (Equation 2.38) [51]. Apart from the slice thickness, the maximum available gradient amplitude also influences the image resolution. Due to the requirements on the sampling time of the 2D-cine bSSFP acquisition for the NuFD method in order to be able to sample the ventilation and perfusion frequency, higher read-out bandwidths are necessary to reduce TR. Consequently, with a fixed high read-out bandwidth, higher image resolutions can only be achieved with high gradient amplitudes, as can be derived from Equations 2.33 and 2.39 [62].

2.6 Radiation-Induced Lung Toxicities (RILT)

Even though RT plays an important role in the treatment of lung tumors, one common side effect of RT delivered to the lungs is radiation-induced lung injury (RILI). Depending on the time between end of RT and occurrence, two conditions are differentiated, namely RP and RILF. Incidence rates for RILI vary widely from 5-58% [109] but decreased with the introduction of advanced RT techniques to 29-32% for IMRT and 24-29% for VMAT [110]. For MRgRT, incidences of 12-17% have been reported [43, 111].
RP typically occurs within 1-6 months after RT and in most patients within the first three months and shows as radiological changes on CT-scans in the tumor region such as ground-glass opacities and consolidations potentially along with common clinical symptoms such as dyspnea, low-grade fever and non-productive coughing [110, 112]. Radiological changes and symptoms occurring later than 6 months after RT, typically within one year, are defined as RILF. RP development, which is also known as the acute exudative phase of RILI involves complex molecular and cellular processes and is pathophysiologically defined by capillary injury, oxidative stress, vascular damage and inflammatory cell infiltration leading to collagen fibril deposition [6, 110]. The ongoing inflammation preserves the damage of the alveolar epithelial and vascular endothelial cells and aids the infiltration of immune cells, the capillary permeability and pulmonary edema that result in pathological changes [6]. If this condition persists over a longer time period, epithelial and or endothelial cells transform to mesenchymal cells, RILI transitions into RILF, the chronic fibrotic phase. This phase is defined by fibroblastic proliferation, vascular sclerosis, fibrous tissue deposition and collapse of alveolar spaces [6].
In the following sections, the focus will be mainly on RP.

2.6.1 Diagnosis and Grading

RP is a common toxicity of RT, yet apart from recommendations found in a Delphi consensus study, there exist no general guidelines on RP diagnosis and management as well as the frequency of follow-up imaging [113]. The diagnosis of RP is typically

TABLE 2.1: **A summary of RP grades.** The symptoms, diagnosis and treatment approaches are summarized for CTCAE, RTOG and LENT-SOMA scheme, as the definitions of grades vary slightly between the schemes. As grade 5 is typically defined as death, it was not included in this table. Information from [92, 109, 110, 113].

	Grade 1	Grade 2	Grade 3	Grade 4
Symptoms	none or mild	moderate	severe	life-threatening
Diagnosis	Affected region $<25\%$ of lung	Affected region 25-50%	Affected region >50-75%	Affected region $>75\%$
Treatment	None	corticosteroids	corticosteroids and antibiotics	corticosteriods, antibiotics, intubation

based on findings on follow-up CT-scans [110, 114] in combination with the clinical presentation of the patient. Typical image findings are ground-glass opacities, consolidative opacities, traction bronchiectasis, or less common, crazy paving (interstitial septal thickening with associated ground-glass opacities), reversed halo (peripheral rim of consolidation surrounding a ground-glass opacity) [6, 109]. Depending on the severity of the radiological findings and potential RP-associated symptoms, RP is graded into five categories from an asymptomatic condition (grade 1) to death (grade 5) that define the disease management and treatment. Several grading systems exist that mostly only differ slightly in the definitions of grades 1-3 [113]. Three commonly used grading schemes are: Common Terminology Criteria for Adverse Events (CTCAE), Radiation Therapy Oncology Group (RTOG) and the Late Effects in Normal Tissue-Subjective Objective Management Analysis (LENT-SOMA) from the European Organization for Research and Treatment of Cancer (EORTC). A summary of the RP grade definitions and management is given in Table 2.1. To assess and monitor potential RP and/or tumor recurrence, repeated follow-up CT-scans are recommended every three months in the first year after RT, every 6-12 months in the years 1-3 and once a year in the following years (up to five years after RT) [6, 114].

2.6.2 Prediction Approaches

The avoidance of RP and potential subsequent long-term consequences and restrictions are of great interest. Several approaches have been proposed over the years to predict the occurrence of RP in order to identify patients at risk and to derive new treatment or dose constraints. Even though predisposing factors such as comorbidities (e.g. interstitial lung disease (ILD)), smoking, tumor location, age, and GTV or PTV sizes can increase the risk of RP development, studies have not been able to show clear correlations and influences [109, 115]. Dosimetric parameters and particularly the MLD and the V20, that already serve as constraints in the dose planning

phase, have been investigated regarding their predictive qualities but have not been found to be consistently predictive. Multiple studies on the one hand reported significant differences in these parameters between the RP and non-RP patient groups [116–118] and on the other hand no significant differences were found in other studies [44, 45, 119].
Apart from finding clinical or pure dosimetric factors, recent research focus has shifted towards the incorporation of functional lung imaging into the treatment workflow [120, 121]. The motivation for the inclusion of functional information is to especially protect highly-functioning, healthy lung tissue that is involved in gas exchange by reducing the radiation dose delivered to these lung areas. It is hypothesized that including this information in the treatment planning to supplement the anatomical images (functional avoidance planning) could reduce the toxicity and risk for RP and in turn improve the functional outcome [121, 122]. Furthermore, functional imaging opens up opportunities in finding function-based RP predictors [120]. Finding these parameters and the respective predictive power and the corresponding correlations with outcome can be considered as the first step in the establishment of biomarkers that later allow to derive dose constraints or to support the treatment planning. Several approaches to extract pre-treatment ventilation and/or perfusion information have been investigated. For the extraction of ventilation, the use of standard 4DCT [44] or inhale-exhale CT [123] as well as PET [48] or SPECT [124] have been proposed. To assess the voxel-based ventilation, the former two approaches require image registration (see Section 2.7) between the breathing states before voxel-wise intensity subtraction of the inspiration state from the expiration state [125] or utilizing the so-called Jacobian method [126], while the latter two require the inhalation of gaseous radioactively-labeled chemical compounds. PET and SPECT imaging with the intravenous administration of radioactive chemical compounds have been similarly considered for the assessment of perfusion [45, 48, 119, 124]. The dominating approach for the definition of functional parameters so far has been the formulation of functional dose-volume parameters based on pre-treatment imaging such as the fV20 or the fMLD, describing the highly-functioning (ventilation and/or perfusion) lung volume receiving more than 20 Gy and the mean dose in the highly-functioning lung, respectively. Due to the current recommendation to not treat grade 1 RP (Table 2.1), most studies have focused on the prediction of RP grade ≥ 2 or even grade ≥ 3 but found higher predictive qualities of fV20 and fMLD compared to the pure dosimetric counterparts V20 and MLD. These parameters even have been shown in some studies to add valuable information to the anatomical information in multivariable/multivariate prediction models [120, 121]. Even though MRI and in particular MRI utilizing the inhalation of xenon or helium to assess lung ventilation has been considered to analyze dose-response relationships, only a limited number of studies investigate the potential of MRI during MRgRT to provide (prediction) biomarkers [121].

The increase in general interest in the integration of functional information has been also aided by the growing application and clinical availability of image-guided RT

devices that in most cases allows the effortless (repeated) acquisition of additional (functional) imaging data and therefore to access potential functional parameters predictive of RP within the regular treatment workflow. The idea of finding these predictive functional parameters derived from repeated imaging is also one of the key topics in this thesis.

2.7 Image Registration

Image registration is one of the key elements in intra- and inter-patient comparison, correspondence or combination of two or more sets of mono- or multimodal images in the medical context. The general task of image registration is to transform several image sets into a single coordinate system to combine image sets with potentially complementary information to aid diagnosis, modelling and planning steps, real-time image guidance or post-processing procedures [127]. In this thesis, image registration found application in the clinical MRgRT workflow, where the baseline MRI-scan is registered to the daily setup MRI-scans, the baseline CT-scan is registered to the baseline MRI-scan and the real-time cine images that are acquired during the treatment are registered to the respective reference image frame to allow for image guidance. Apart from the clinical importance of image registration, it was also used to register a 2D MRI series, acquired in free-breathing, to a reference breathing state, as well as to align volumes acquired with different MRI sequences, i.e., the registration of images with different TE, different MRI-scanners, i.e., registration of images acquired at the 0.35 T MR-Linac and a 1.5 T diagnostic scanner, and different modalities, i.e., registration of 3D-MRI and 3D-CT images.

2.7.1 Basic Principles

The general idea of image registration is to find a transformation for a source or moving image so that it is spatially or temporally aligned with a target or fixed image. More precisely this means that a transformation vector field $\boldsymbol{v}(\boldsymbol{x})$ needs to be found that warps each voxel of the moving image $I_{\text{mov}}(\boldsymbol{x'})$, defined in the 3D coordinates $\boldsymbol{x'} = (x'_1, x'_2, x'_3)$ of the moving image domain, to the respective voxel $I_{\text{fixed}}(\boldsymbol{x})$ in the fixed image domain $\boldsymbol{x} = (x_1, x_2, x_3)$. A simplified version of the idea is visualized in Figure 2.19. Mathematically, this process of generating these transformed moving images $\tilde{I}_{\text{mov}}(\boldsymbol{x})$ is described as:

$$\tilde{I}_{\text{mov}}(\boldsymbol{x}) = I_{\text{mov}}\big(\boldsymbol{x'}\big) \circ \boldsymbol{v}(\boldsymbol{x})\,. \tag{2.57}$$

Due to an increase in computational cost with increasing transformation complexity, image registration algorithms are usually formulated as optimization problems and are therefore of iterative nature [128]. The basic principle of such an iterative registration algorithm is as follows: The moving image is transformed using an estimation from a pre-defined transformation model, which are described in more detail in the following two subsections. Based on this transformed moving image, an

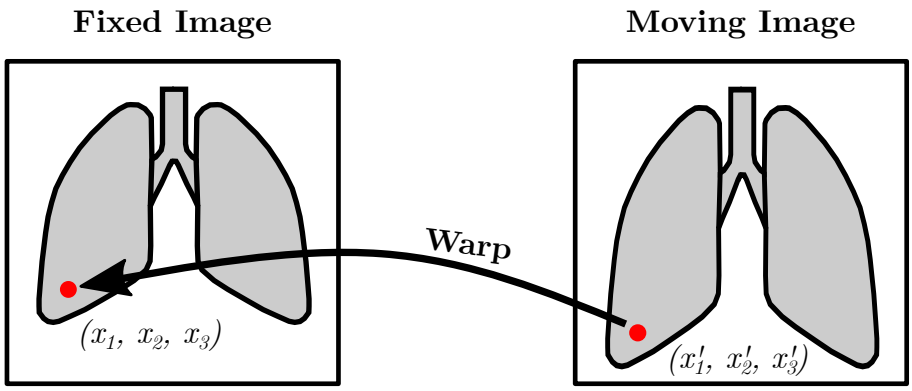

FIGURE 2.19: **A simplified illustration of the registration process.** The basic idea of image registration is to find a transformation $\boldsymbol{v}(\boldsymbol{x})$ that warps the voxels $I_{\text{mov}}(\boldsymbol{x'})$ in the moving image domain $\boldsymbol{x'} = (x_1', x_2', x_3')$ to the corresponding voxels $I_{\text{fixed}}(\boldsymbol{x})$ in the fixed image domain $\boldsymbol{x} = (x_1, x_2, x_3)$. Own figure.

also pre-defined similarity cost function is calculated to determine the quality of the alignment between the transformed moving and the fixed image. The cost function then informs the optimizer of the algorithm on how to improve the estimation of the transformation that is applied to the moving image in the next iteration. This process is usually repeated until the algorithm reaches a local minimum in the similarity cost function and the moving and fixed images are aligned [128]. The goal of the registration algorithm is therefore to find a $\boldsymbol{v}(\boldsymbol{x})$ that maximizes the similarity between $\tilde{I}_{\text{mov}}(\boldsymbol{x})$ and the fixed image $I_{\text{fixed}}(\boldsymbol{x})$ by minimizing a cost function ζ:

$$\underset{\boldsymbol{v}}{\operatorname{argmin}}\, \zeta\left(I_{\text{mov}} \circ \boldsymbol{v}, I_{\text{fixed}}\right) \tag{2.58}$$

that evaluates the alignment of transformed moving to fixed image and forces the vector field $\boldsymbol{v}$ to follow a specific, pre-defined transformation model.

2.7.2 Transformation Models

Depending on the complexity of the registration task, either only one or a combination of different transformation models are chosen and applied in a step-wise manner with increasing transformation complexity. In addition to using multiple transformation types, usually multiple resolution levels, e.g., using a pyramid scheme, are utilized within each transformation type. Specifically, a fast and low resolution registration result serves as a first estimate for the next higher resolution level and therefore more complex registration step in order to avoid local minima and speed up the convergence of the iterative registration algorithm [129].

Rigid and Affine Registration

Many medical imaging applications, e.g., brain MRI or head and neck MRI require a correction of the acquired set of images for patients' translational or rotational motion. This type of transformation model is called rigid registration and is restricted to six degrees of freedom (DOF), meaning that the transformation vector field $\boldsymbol{v}(\boldsymbol{x})$ is of global nature and therefore mathematically defined by a single, linear transformation matrix $\mathcal{M}$ and a translation vector $\boldsymbol{\tau} = (\tau_1, \tau_2, \tau_3)$:

$$\boldsymbol{v}(\boldsymbol{x}) = \mathcal{M}\boldsymbol{x} + \boldsymbol{\tau}. \tag{2.59}$$

In the case of rigid registrations, $\mathcal{M}_{\text{rigid}}$ is given as product of three rotation matrices with θ_{x_1}, θ_{x_2} and θ_{x_3} being the rotation angles around the respective axis:

$$\mathcal{M}_{\text{rigid}} = \begin{pmatrix} 1 & 0 & 0 \\ 0 & \cos(\theta_{x_1}) & -\sin(\theta_{x_1}) \\ 0 & \sin(\theta_{x_1}) & \cos(\theta_{x_1}) \end{pmatrix} \begin{pmatrix} \cos(\theta_{x_2}) & 0 & \sin(\theta_{x_2}) \\ 0 & 1 & 0 \\ -\sin(\theta_{x_2}) & 0 & \cos(\theta_{x_2}) \end{pmatrix} \begin{pmatrix} \cos(\theta_{x_3}) & -\sin(\theta_{x_3}) & 0 \\ \sin(\theta_{x_3}) & \cos(\theta_{x_3}) & 0 \\ 0 & 0 & 1 \end{pmatrix}. \tag{2.60}$$

Extending this transformation model to twelve DOF by allowing global scaling of the moving image as well as shearing, the commonly known affine registration is described by:

$$\mathcal{M}_{\text{affine}} = \begin{pmatrix} 1 & \nu_{1,2} & \nu_{1,3} \\ \nu_{2,1} & 1 & \nu_{2,3} \\ \nu_{3,1} & \nu_{3,2} & 1 \end{pmatrix} \begin{pmatrix} \iota_{x_1} & 0 & 0 \\ 0 & \iota_{x_2} & 0 \\ 0 & 0 & \iota_{x_3} \end{pmatrix} \mathcal{M}_{\text{rigid}} \tag{2.61}$$

where $\nu_{2,1}$ and $\nu_{3,1}$; $\nu_{1,2}$ and $\nu_{3,2}$ as well as $\nu_{1,3}$ and $\nu_{2,3}$ define the shearing direction and magnitude for the axis x_1, x_2 and x_3, respectively and ι_{x_1}, ι_{x_2} and ι_{x_3} the scaling for each axis [128]. The included transformations in the rigid and affine registration are illustrated in Figure 2.20 (B) and (C).

Deformable Registration

Even though rigid and affine transformations are sufficient in many medical registration problems, more complex anatomical motions such as breathing or the pulsating heart that involve volume or morphological changes of one or several organs require an additional registration step, namely non-rigid or deformable image registration (DIR), to compensate for the non-rigid deformations of structures [127]. Instead of being globally defined, such as the rigid and affine transformations, the deformable transformation is individually defined for each point/voxel in the image using a continuous displacement field $\boldsymbol{u}(\boldsymbol{x})$ [128]:

$$\boldsymbol{v}(\boldsymbol{x}) = \boldsymbol{x} + \boldsymbol{u}(\boldsymbol{x})\,. \tag{2.62}$$

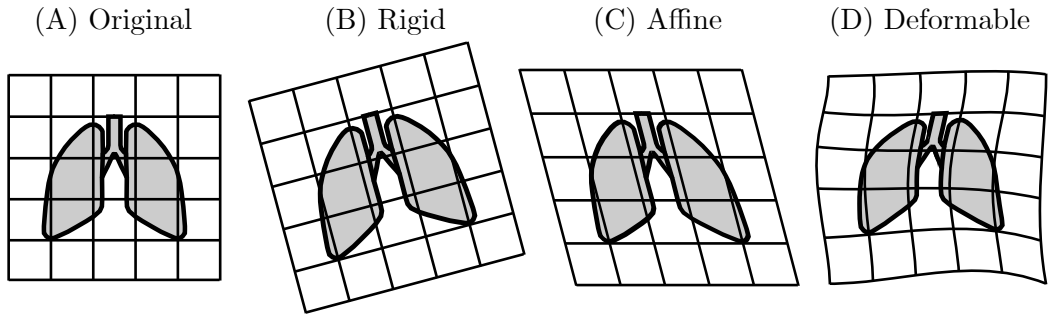

FIGURE 2.20: **An illustration of the transformation types.** The original image in (A) can be rotated and shifted for the rigid transformation in (B). The extension of the rigid transformation with shearing and scaling defines the affine transformation shown in (C). For more complex, structural changes of the image, a deformable transformation (D) needs to be utilized. Inspired by [127].

DIR algorithms can be loosely divided into two types: parametric and non-parametric registration algorithms. The idea of the latter transformation algorithms is to model the image under deformation as a physical model. In these deformation models, the deformed image is modeled, e.g., as an elastic body following the Navier-Cauchy Partial Differential Equation, as a viscous fluid that is described by the Navier-Stokes equation as well as diffusion process or optical flow [130]. While non-parametric registrations rely on transformations resembling physical motions, parametric registrations are inspired by interpolation and approximation theory and are based on the optimization of a set of parameters that control basis functions [128, 130]. Apart from radial basis functions, B-splines are widely used as basis functions for image registration using free-form deformations (FFD) [131]. The basic principle of FFD with B-splines is to describe the deformation of an object/image by the manipulation of an underlying rectangular $n_{x_1} \times n_{x_2} \times n_{x_3}$ grid of control points $\phi_{i,j,k}$ with uniform spacing κ. This means that the control points or rather the coefficient values of these control points parameterize the movement of each voxel between the fixed and moving image. Interpolation of these coefficients using piece-wise continuous B-spline basis allows to determine the displacement vectors for each voxel [132]. The displacement field $\boldsymbol{u}(\boldsymbol{x})$ is therefore defined by the l-th basis function θ_l of the 1D cubic B-splines [131]:

$$\boldsymbol{u}(\boldsymbol{x}) = \sum_{l=0}^{3} \sum_{m=0}^{3} \sum_{n=0}^{3} \theta_l(u)\theta_m(v)\theta_n(w)\phi_{i+l,j+m,r+n} \tag{2.63}$$

with $i = \lfloor \frac{x_1}{\kappa} \rfloor - 1$, $j = \lfloor \frac{x_2}{\kappa} \rfloor - 1$, $r = \lfloor \frac{x_3}{\kappa} \rfloor - 1$, $u = \frac{x_1}{\kappa} - \lfloor \frac{x_1}{\kappa} \rfloor$, $v = \frac{x_2}{\kappa} - \lfloor \frac{x_2}{\kappa} \rfloor$, $w = \frac{x_3}{\kappa} - \lfloor \frac{x_3}{\kappa} \rfloor$ and:

$$\begin{aligned} \theta_0(s) &= \frac{(1-s)^3}{6} \\ \theta_1(s) &= \frac{3s^3 - 6s^2 + 4}{6} \\ \theta_2(s) &= \frac{-3s^3 + 3s^2 + 3s + 1}{6} \\ \theta_3(s) &= \frac{s^3}{6} \end{aligned} \tag{2.64}$$

with $s \in [u, v, w]$. As mentioned before, Equation 2.63 is calculated repeatedly, meaning that the B-splines coefficient values are refined iteratively until the warped moving image closely resembles the fixed image by minimizing the cost function [132, 133]:

$$\zeta_{\text{total}} = \zeta_{\text{similarity}} + \lambda \zeta_{\text{smoothness}} \tag{2.65}$$

comprising of the cost of the voxel-based similarity measure $\zeta_{\text{similarity}}$ that is calculated with a pre-defined similarity metric and a smoothness constraint $\zeta_{\text{smoothness}}$, e.g., penalization bending energy or minimization of linear elastic energy [134], whose influence is controlled by a weighting factor λ_{reg}, also known as regularization parameter [133, 135]. As the resolution of the control point grid determines the performance of the registration, small-scale or more localized deformations are achieved by a smaller grid spacing, while more global or deformations on a larger scale only require a coarse grid [135]. In order to improve the efficiency, despite the increasing computational complexity with higher grid resolutions, a multi-resolution scheme can be utilized. For this, an initial registration is performed on a low resolution grid until the optimizing algorithm reaches convergences or a number of pre-defined iteration steps. This result then serves as input for another registration step using a higher resolution grid, whose result could be again used as input for another registration step [135].

2.7.3 Similarity Metrics

An essential part of an iterative registration algorithm or more precisely of the cost function utilized in the algorithm is the similarity metric $\zeta_{\text{similarity}}$, as it measures the degree of matching between the fixed and the deformed moving image and therefore drives the optimizer [127]. Several similarity metrics have been introduced in the context of medical image registration such as sum of absolute differences, (normalized) cross-correlation, Jensen–Havrda–Charvat–Tsallis divergence, mean squared error (MSE) or mutual information (MI) [127, 136]. As the underlying principle and requirements on the image pair is different for each similarity metric, the metric needs to be carefully selected depending on the application. In the following, two similarity metrics, i.e., MSE and MI, that are commonly used in the field of radio-

therapy and mono- or multi-modal lung registrations are described in more detail. The latter metric found application in this thesis.

Mean Squared Error (MSE)

The MSE metric provides one of the most basic, but at the same time computationally efficient cost functions. It is calculated by taking the square of the intensity difference between the fixed and the moving image for each voxel and summing this over all voxels in the fixed image domain $\mathbb{D}_{I_{\text{fixed}}}$ and dividing this by the number of voxels $N_{\boldsymbol{x}}$ [128]:

$$\zeta_{\text{MSE}} = \frac{1}{N_{\boldsymbol{x}}} \sum_{\boldsymbol{x} \in \mathbb{D}_{I_{\text{fixed}}}} \left(I_{\text{fixed}}(\boldsymbol{x}) - \tilde{I}_{\text{mov}}(\boldsymbol{x}) \right)^2. \tag{2.66}$$

Even though MSE allows for localized, voxel-based calculation and therefore a high local sharpness, it is limited by the high dependency on the absolute image intensity values. Consequently, the registration performance using MSE can suffer in the case of multi-modal registration problems or in the presence of artifacts and intensity shifts [128].

Mutual Information (MI)

Instead of using intensity differences between the fixed and the deformed moving image directly, the MI metric measures the statistical dependency between the two images and is therefore robust against noise and intrinsic intensity differences, allowing it to be used even in multi-modal registrations [127, 128]. The cost function ζ_{MI} is expressed as [137]:

$$\zeta_{\text{MI}}\left(I_{\text{fixed}}, \tilde{I}_{\text{mov}}\right) = -\left(H(I_{\text{fixed}}) + H\left(\tilde{I}_{\text{mov}}\right) - H\left(I_{\text{fixed}}, \tilde{I}_{\text{mov}}\right)\right) = -\text{MI} \tag{2.67}$$

where $H(I_{\text{fixed}})$ and $H\left(\tilde{I}_{\text{mov}}\right)$ represent the Shannon entropy of the fixed and moving image, respectively, and $H\left(I_{\text{fixed}}, \tilde{I}_{\text{mov}}\right)$ the joint entropy. In the context of images and their underlying intensities, the Shannon entropy evaluates the ability to predict a given intensity value in the image. Mathematically, the Shannon entropy for a discrete random variable A is described as [128]:

$$H(A) = -\sum_{q_A} P_A(q_A) \log(P_A(q_A)) \tag{2.68}$$

with $P_A(q_A)$ being the probability that the value q_A occurs in A. Adding a second random variable B and intensity value q_B, the joint entropy that analyzes how well the pair of q_A and q_B can be predicted using the joint probability distribution $P_{A,B}(q_A, q_B)$ is given by [128]:

$$H(A,B) = -\sum_{q_A, q_B} P_{A,B}(q_A, q_B) \log(P_{A,B}(q_A, q_B)). \tag{2.69}$$

Using Equations 2.68 and 2.69, the MI is defined as [128]:

$$\mathrm{MI}(A, B) = H(A) + H(B) - H(A, B). \tag{2.70}$$

As the MI metric is constructed to increase with similarity of the images, a negative sign has to be added to Equation 2.70 before insertion into the cost function given in Equation 2.67 in order to allow for a formulation as minimization problem.

2.7.4 Landmark-Based Registration

In addition to the registration methods described in the previous sections, there is another image registration approach called feature-based image registration. While automated registration methods can run into problems for some applications, e.g., multi-modal registration or registration of MRI-scans with different image contrast, the manual selection of corresponding points in both, the fixed and the moving image, aids the registration process or even provides an alternative approach.

2.8 Data Analysis/Concepts

The prediction of events or outcomes from data requires the utilization of statistical concepts. The concepts employed in this thesis, namely the general theory behind univariate prediction analysis in Section 2.8.1, the receiver operating characteristic (ROC) curves as visualization and comparison tool in Section 2.8.2 along with bootstrapping as an internal validation strategy in Section 2.8.3 are described. In Section 2.8.4 metrics for spatial analysis are introduced.

2.8.1 Univariate Prediction Analysis

Univariate prediction analysis can be understood as a classification problem with only two classes and one classifier variable/parameter. Hence, each instance or test result is mapped to either the positive or the negative class label. Consequently, a classifier or classification model maps instances to predicted classes. Depending on the true class label and the predicted class label derived from the classifier, four case are differentiated:

- **true positive (TP)**: true class label is positive and predicted class label is positive
- **true negative (TN)**: true class label is negative and predicted class label is negative
- **false positive (FP)**: true class label is negative and predicted class label is positive
- **false negative (FN)**: true class label is positive and predicted class label is negative

These four different cases are usually visualized in a so-called 2×2 confusion matrix as shown in Figure 2.21. Based on this, several common metrics are defined that

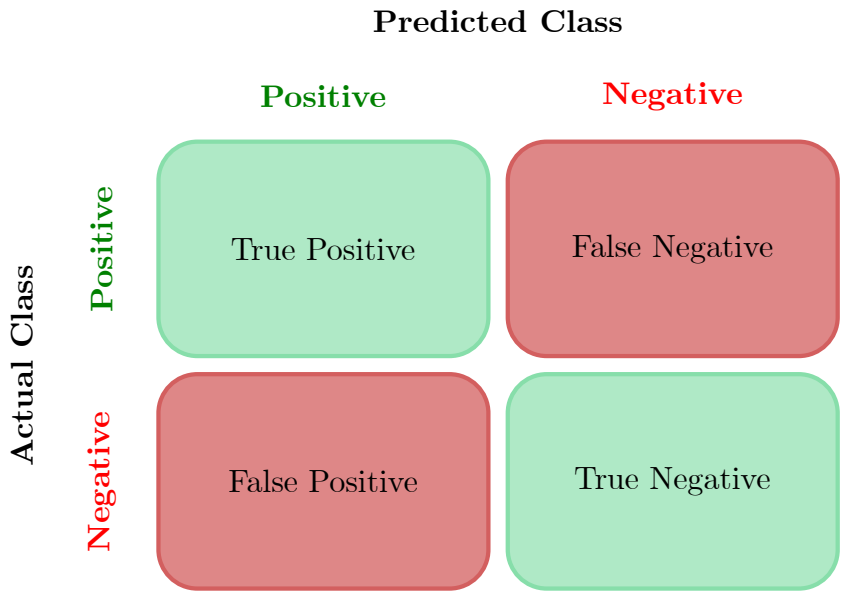

FIGURE 2.21: **Illustration of the confusion matrix.** This figure presents the schematics of the confusion matrix for a binary classification problem in which four different cases are differentiated depending on the actual class and the investigated classifier predicted class. If actual and predicted class coincide, true positives (both classes are positive) or true negatives (both are negative) are achieved. If actual and predicted class disagree, the classifier produced either a false negative (actual class is positive, but predicted class is negative) or a false positive (actual class is negative, but predicted class is positive).

allow to evaluate the performance of a classifier, namely the specificity given by [138]:

$$\text{specificity} = \frac{\text{true negatives}}{\text{false positives} + \text{true negatives}} = 1 - \text{false positive rate} \tag{2.71}$$

and the sensitivity described by:

$$\text{sensitivity} = \frac{\text{true positives}}{\text{true positives} + \text{false negatives}} = \text{true positive rate}. \tag{2.72}$$

2.8.2 Receiver Operating Characteristic (ROC) Curve

A common way to visualize/compare the performance of classifiers is to employ ROC curves that are 2D representations of the false positive rate against the true positive rate. With this, the relative trade-off between benefits (TN) and costs (FP)

is assessed. As discrete classifiers only create one FP rate-TP rate pair, in ROC space these classifiers are presented as single points. For probabilistic classifiers, such as logistic regression or a Naive Bayes classifier, that only produce the probability or a score for an instance or test result to belong to a class or classification models that classify based on a continuous parameter, thresholds need to be utilized to convert the classifier output into binary prediction results. By varying the threshold from the lowest to the highest possible probability, score or parameter value, a FP rate-TP rate pair is generated for each threshold and therefore a point on the ROC curve is retrieved. This resulting graphical representation (Figure 2.22) allows to determine the best threshold for a classification model depending on requirements regarding the sensitivity and specificity. A common approach used to determine the best threshold is by finding the maximal Youden index [139]:

$$\text{Youden index} = \text{sensitivity} + \text{specificity} - 1 \tag{2.73}$$

that by construction maximizes the trade-off between benefits and costs.
In addition to comparing the ROC curves to assess performance differences between classifiers, the area under the curve (AUC) value is calculated for each ROC curve. As a random classifier is expected to reside on the diagonal, realistic classification models should achieve AUC values between 0.5 and 1.0 with higher values being better [138].

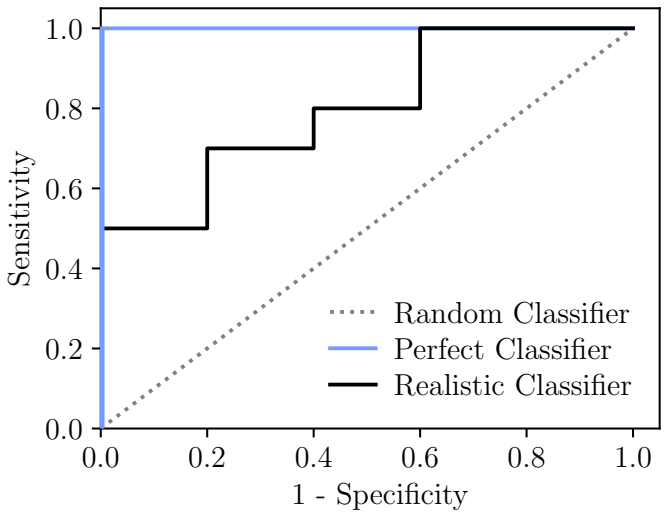

FIGURE 2.22: **The receiver operating characteristic curve (ROC).** The ROC curves of a perfect classifier (blue solid line), a realistic classifier (black solid line) and a random classifier (black dotted line) are depicted as a plot of the sensitivity over (1 - specificity).

2.8.3 Bootstrapping

A problem of any classifier or predictive model especially in the medical field is that these models are developed on a subset of all possible datasets or a subset of patients from the whole population. The model performance therefore might differ from the performance obtained for another dataset. In order to provide a more accurate and more general estimate of the model performance, several strategies have been introduced. Apart from the common simple split-sample approach, where the available dataset is divided into a training subset for model development and a validation subset to assess the performance, more advanced methods exist. One method that is considered to be one of the most efficient, but computationally demanding validation strategies is bootstrapping [140]. The basic principle of bootstrapping and other resampling approaches is to artificially, but mathematically validly, increase the sample size or in other words generate multiple samples from the underlying population [140–142]. This is done by repeatedly drawing samples, of the same size as the available dataset, with replacement from the original available dataset. The performance of a classification model after bootstrapping is usually assessed by generating an ROC curve and AUC value for every bootstrapping iteration and subsequently calculating the average of the ROC curves over all bootstrapping samples along with an averaged AUC value. While split-sample methods in particular and also especially in small sample sizes have been shown to suffer from performance underestimation and high variability, bootstrapping allows a more stable and almost unbiased performance estimation [140]. Even though these internal validation strategies are not able to fully replace an external performance evaluation on an external validation dataset, bootstrapping is considered as a necessary first validation tool particularly in the early stages of classifier or predictive model development [143].

2.8.4 Spatial Analysis

Spatial analyses on a voxel level, i.e., image segmentations, require, apart from visual evaluations, the use of specific metrics to quantitatively assess the performance [144]. For this, especially in the medical context, the comparability between a reference or gold-standard segmentation and the proposed analysis-based segmentation is probed. Many metrics have been proposed over the years that can be, depending on their nature, grouped into different categories, e.g., spatial overlap-based, probabilistic-based or spatial distance-based methods [145]. Typically used spatial overlap-based evaluation measures, that found application in this thesis, are the sensitivity (2.72), precision:

$$\text{precision} = \frac{\text{true positives}}{\text{true positives} + \text{false positives}} \tag{2.74}$$

and the Dice similarity coefficient (DSC):

$$\text{DSC} = \frac{2 \cdot \text{true positives}}{2 \cdot \text{true positives} + \text{false positives} + \text{false negatives}}. \tag{2.75}$$

One of most common spatial distance-based methods is the 95% Hausdorff distance (HD95), i.e., the 95th percentile of the distance between boundary point in the ground-truth and the nearest boundary point in the analyzed segmentation [145]. A probabilistic-based metric, that is not only used in the context of classification model performance assessment, as described in Section 2.8.2, is the ROC and the corresponding AUC. Since the ROC reduces to one measurement, i.e. one point, in the context of segmentations, the segmentation AUC (Seg AUC) is defined as the trapezoidal area between the sensitivity $= 0$ line, the $1 - \text{specificity} = 1$ and the single measurement point [146]:

$$\text{Seg AUC} = 1 - \frac{1}{2}\left(\frac{\text{FP}}{\text{FP} + \text{TN}} + \frac{\text{FN}}{\text{FN} + \text{TP}}\right). \tag{2.76}$$

3 | Publication I

Klaar, R., Rabe, M., Gaass, T., Schneider, M. J., Benlala, I., Eze, C., Corradini, S., Belka, C., Landry, G., Kurz, C., & Dinkel, J. (2023). Ventilation and perfusion MRI at a 0.35 T MR-Linac: feasibility and reproducibility study. Radiation Oncology, 18(1), 58. https://doi.org/10.1186/s13014-023-02244-1

3.1 Summary of Publication I

Non-contrast enhanced functional lung MRI using the FD or its extension the NuFD (Section 2.3.1) have been successfully introduced at clinical diagnostic MRI-scanners at various field strengths and for various lung diseases. The idea of the project for this paper was to test if cine images with the required temporal resolution for FD or rather NuFD can be acquired at a low-field MR-Linac and if the NuFD technique in general can be transferred to this hybrid device, which had not been done before. As bSSFP sequences (Section 2.2.5) find application at MR-Linacs for the acquisition of clinical images, an already implemented bSSFP sequence was used and optimized in terms of spatio-temporal resolution. As this project was considered to be the first step in bringing functional lung imaging at the MR-Linac to lung tumor patients treated at the device, what would later become Publication II, the feasibility of the image acquisition and the NuFD method to assess ventilation and perfusion firstly had to be assessed in healthy volunteers. In order to mimic multiple treatment fractions and to investigate the overall reproducibility of the NuFD technique especially regarding differences in breathing patterns between treatment fractions at the MR-Linac of the Department of Radiotherapy at the LMU University Hospital in Munich, ten healthy volunteers were repeatedly scanned at two different slice positions with breaks inside and outside the scanner. Different breathing patterns were simulated by asking the volunteers to breath in a deeper and shallower fashion during two specific scans. As consistent breathing patterns from fraction to fraction could not be assumed for patients suffering from lung tumors and potential additional comorbidities and the FD or NuFD is only qualitative and depends on the breathing amplitude, a direct comparison of ventilation and perfusion maps at different fraction days would not be possible. Considering that the more final goal is the correlation of longitudinal functional changes with treatment-related outcomes, the reproducibility of this method

is essential. To address this problem, two normalization strategies have been developed and their performance in improving the comparability between functional maps from different scans was evaluated on the repeated scans for each volunteer. One of the normalization strategies consisted of finding a normalization factor based on the slope of the diaphragm position vs ventilation signal amplitude for a reference scan that was then multiplied to later scans of the same volunteer/patient. The second strategy required to select a region-of-interest (ROI) on a (healthy) part of the lung and divide the ventilation and perfusion maps with the respective mean ventilation and perfusion map value found within the ROI. In order to investigate a potential position dependency of the ROI normalization, the performance of six ROI positions (three per lung) was analyzed.
With this publication, not only the feasibility of transferring the NuFD technique to a low-field MR-Linac was successfully shown, but the two developed normalization strategies clearly improved the reproducibility and comparability of repeated ventilation and perfusion maps, especially in the presence of differences in breathing patterns. This was an important first step towards clinically implementing this technique to monitor longitudinal changes in ventilation/perfusion that might be exploited, e.g., for early treatment repsonse assessment.

3.2 Contributions to Publication I

My contributions to this publication involved logistics of volunteer scan planning, data acquisition, image processing, development of normalization strategies, general result analysis, statistical evaluation, visualization of the results and figure preparation as well as writing the original manuscript draft.
First, I designed a scanning protocol for volunteer scans with repeated scans with defined breathing patterns and breaks. In assistance with PD Dr. rer. nat. Christopher Kurz and Dr. rer. nat. Moritz Rabe, I recruited volunteers and performed the scans at the 0.35 T MR-Linac at the Department Radiation Oncology of the LMU University Hospital following the designated scanning protocol using an MRI sequence, whose parameters were optimized by Dr. rer. nat. Moritz J. Schneider and Prof. Dr. med. Julien Dinkel. I preprocessed the images, which included image registration of each image series, manual segmentation, signal filtering and NuFD evaluation. For this, I optimized and automated a pipeline initially prepared by Dr. rer. nat. Thomas Gaass. I developed two normalization strategies in order to be able to compare ventilation and perfusion maps for repeated scans regardless of differences in breathing amplitude and heartbeat. I implemented the normalization in the pipeline for an automated analysis of repeated scans and used this pipeline to analyze the performance of the normalization strategies on the volunteer scans. I performed the statistical tests to assess the repeatability improvement of the normalized functional maps compared to unnormalized maps. I discussed the results with Prof. Dr. Guillaume Landry, PD Dr. rer. nat. Christopher Kurz and Dr. rer. nat. Moritz Rabe and I created workflow and results plots. Finally, I wrote the original

manuscript draft and reviewed and edited the manuscript in cooperation with all co-authors.

3.3 Publication I

Klaar *et al. Radiation Oncology (2023) 18:58*
https://doi.org/10.1186/s13014-023-02244-1

Radiation Oncology

RESEARCH Open Access

Ventilation and perfusion MRI at a 0.35 T MR-Linac: feasibility and reproducibility study

Rabea Klaar[1,2*], Moritz Rabe[3], Thomas Gaass[1,2], Moritz J. Schneider[1,2,4], Ilyes Benlala[1,2,5,6,7], Chukwuka Eze[3], Stefanie Corradini[3], Claus Belka[3,8], Guillaume Landry[3], Christopher Kurz[3†] and Julien Dinkel[1,2†]

Abstract

Background Hybrid devices that combine radiation therapy and MR-imaging have been introduced in the clinical routine for the treatment of lung cancer. This opened up not only possibilities in terms of accurate tumor tracking, dose delivery and adapted treatment planning, but also functional lung imaging. The aim of this study was to show the feasibility of Non-uniform Fourier Decomposition (NuFD) MRI at a 0.35 T MR-Linac as a potential treatment response assessment tool, and propose two signal normalization strategies for enhancing the reproducibility of the results.

Methods Ten healthy volunteers (median age 28 ± 8 years, five female, five male) were repeatedly scanned at a 0.35 T MR-Linac using an optimized 2D+*t* balanced steady-state free precession (bSSFP) sequence for two coronal slice positions. Image series were acquired in normal free breathing with breaks inside and outside the scanner as well as deep and shallow breathing. Ventilation- and perfusion-weighted maps were generated for each image series using NuFD. For intra-volunteer ventilation map reproducibility, a normalization factor was defined based on the linear correlation of the ventilation signal and diaphragm position of each scan as well as the diaphragm motion amplitude of a reference scan. This allowed for the correction of signal dependency on the diaphragm motion amplitude, which varies with breathing patterns. The second strategy, which can be used for ventilation and perfusion, eliminates the dependency on the signal amplitude by normalizing the ventilation/perfusion maps with the average ventilation/perfusion signal within a selected region-of-interest (ROI). The position and size dependency of this ROI was analyzed. To evaluate the performance of both approaches, the normalized ventilation/perfusion-weighted maps were compared and the deviation of the mean ventilation/perfusion signal from the reference was calculated for each scan. Wilcoxon signed-rank tests were performed to test whether the normalization methods can significantly improve the reproducibility of the ventilation/perfusion maps.

Results The ventilation- and perfusion-weighted maps generated with the NuFD algorithm demonstrated a mostly homogenous distribution of signal intensity as expected for healthy volunteers regardless of the breathing maneuver and slice position. Evaluation of the ROI's size and position dependency showed small differences in the performance. Applying both normalization strategies improved the reproducibility of the ventilation by reducing the median deviation of all scans to 9.1%, 5.7% and 8.6% for the diaphragm-based, the best and worst performing ROI-based normalization, respectively, compared to 29.5% for the non-normalized scans. The significance of this improvement was confirmed by the Wilcoxon signed rank test with $p < 0.01$ at $\alpha = 0.05$. A comparison of the techniques against

†Christopher Kurz and Julien Dinkel have contributed equally to this work.

*Correspondence:
Rabea Klaar
Rabea.Klaar@med.uni-muenchen.de
Full list of author information is available at the end of the article

each other revealed a significant difference in the performance between best ROI-based normalization and worst ROI ($p = 0.01$) and between best ROI-based normalization and scaling factor ($p = 0.02$), but not between scaling factor and worst ROI ($p = 0.71$). Using the ROI-based approach for the perfusion-maps, the uncorrected deviation of 10.2% was reduced to 5.3%, which was shown to be significant ($p < 0.01$).

Conclusions Using NuFD for non-contrast enhanced functional lung MRI at a 0.35 T MR-Linac is feasible and produces plausible ventilation- and perfusion-weighted maps for volunteers without history of chronic pulmonary diseases utilizing different breathing patterns. The reproducibility of the results in repeated scans significantly benefits from the introduction of the two normalization strategies, making NuFD a potential candidate for fast and robust early treatment response assessment of lung cancer patients during MR-guided radiotherapy.

Keywords Functional lung MRI, Radiation therapy, MR-Linac, Non-uniform Fourier decomposition, Ventilation, Perfusion, Low-field MRI

Background

Lung cancer is one of the leading causes of cancer related deaths worldwide [1]. Radiotherapy, and in particular adaptive radiotherapy (ART), have become more and more important in the treatment of lung cancer patients, since ART allows adaption of the treatment plan for possible anatomical and physiological changes based on computed tomography (CT) or magnetic resonance imaging (MRI) between treatment fractions [2–6]. The recent introduction in the clinical routine of hybrid systems that combine a MRI-scanner and a medical linear accelerator (MR-Linacs) allows daily ART and image-guidance [7–11]. The excellent soft-tissue contrast of MRI allows for an improved delineation of organs at risk as well as target volumes and additionally enables precise tumor-tracking and beam-gating based on cine-MRI to mitigate intra-fractional motion, resulting in dosimetric benefits [7, 12–15]. Along with being a non-invasive alternative to CT in terms of treatment planning as well as providing image-guidance during radiotherapy, MR-Linacs also enable MRI-specific methods such as functional imaging of head and neck cancer [16–19], but also functional imaging of the lung. Due to fractionated dose delivery, MR-Linacs even allow longitudinal functional data acquisition within the course of the patients' treatment, which is especially valuable since it may permit early treatment response assessments [20–23].

For functional lung imaging, several techniques have been developed over the years. Some of these approaches require the inhalation of gases such as hyperpolarized helium (^{3}He) [24], xenon (^{129}Xe) [25], fluorine (^{19}F) [26] or oxygen [27] to assess lung ventilation, or the injection of gadolinium-based contrast agents to evaluate perfusion [28], which is not only costly but also technically challenging [29]. An alternative are Fourier Decomposition (FD) MRI [30] techniques, which are performed in free breathing and make use of the intrinsic lung signal variation due to breathing and blood flow, such as Non-uniform Fourier Decomposition (NuFD) [31], PREFUL [32] or SENCEFUL [33]. These techniques do not require a contrast agent, any special equipment or respiratory triggering and are therefore fast, easily applicable and have shown promising results in chronic thromboembolic pulmonary hypertension, asthma, chronic obstructive pulmonary disease (COPD) and cystic fibrosis (CF) studies [31, 32, 34–36]. Due to FD-MRI's dependency on changes in the breathing pattern as well as the residual lung volume, variations in breathing amplitude from fraction to fraction may influence ventilation maps and mask pathological changes. NuFD, a robust FD-MRI technique, has been designed to correct for variations in respiratory and cardiac frequencies during the course of image acquisition by retrospectively converting equidistant sampling into non-equidistant sampling in order to track the main frequencies [31]. Their ease of applicability make FD-MRI techniques particularly well suited for longitudinal studies embedded in an MR-Linac radiotherapy workflow. However, reproducibility of the ventilation maps in such studies remains challenging and additionally requires a form of signal normalization [37]. Otherwise, focal longitudinal changes might be masked by global changes due to variations in the breathing amplitude.

Even though the aforementioned functional lung imaging methods have been developed and optimized for high-field MRI (1.5–3 T), studies by Campbell-Washburn et al. [38] and Deimling et al. [39] showed that lung imaging can benefit from lower magnetic field strengths since the susceptibility artefacts caused by local inhomogeneities at the multiple air-tissue interfaces of the lung parenchyma are reduced [40]. The resulting improved image quality suggests that the transfer and optimization of FD-MRI sequences [30] to a 0.35 T MR-Linac is desirable. So far, these methods have not been evaluated at these devices.

The aim of this study was to test the feasibility of non-contrast enhanced ventilation and perfusion MRI using

NuFD at a 0.35 T MR-Linac, and to improve the reproducibility by introducing normalization strategies.

Methods

In order to improve the reproducibility within a longitudinal study, as required for early response assessment in MR-guided radiotherapy, two ventilation normalization strategies are proposed and their performance is evaluated in a study with ten healthy volunteers. Additionally, the reproducibility of the perfusion is investigated with and without one of the introduced normalization approaches.

Image acquisition

Ten healthy volunteers (24–52 years old, five female and five male) were scanned at a 0.35 T MR-Linac (MRidian, Viewray Inc., Cleveland, Ohio) using a 2D balanced steady-state free precession (bSSFP) sequence that was optimized to achieve the required temporal resolution in order to observe signal intensity changes introduced by respiration and perfusion. Two coronal slice positions were selected with a field-of-view (FOV) of $500 \times 500\,mm^2$, a pixel size of $3.91 \times 3.91\,mm^2$, a slice thickness of 20 mm and a matrix size of 128×128. With a repetition time (TR) of 2.42 ms and echo time (TE) of 1.02 ms, a temporal resolution of 310 ms/image was reached, resulting in a total acquisition time of 1.1 min for a series of 240 images. The flip angle was 70.0° and the receiver bandwidth 710.0 Hz/pixel. The slice positions were chosen for each volunteer individually based on a 3D-bSSFP MRI-scan performed in inspiration breath-hold with a total acquisition time of 25 s. The imaging parameters were: TR = 3.0 ms, TE = 1.27 ms, FOV = $540 \times 465 \times 432\,mm^3$, matrix = $360 \times 310 \times 144$, voxel size = $1.5 \times 1.5 \times 3.0\,mm^3$, flip angle = 60.0°, receiver bandwidth = 604.0 Hz/pixel. The vendor's 6-channel torso coils were used to receive the MR-signal. One slice position was selected to intersect the aorta, while the other was positioned anterior or posterior of the first slice depending on the lung volume of each volunteer. In the following, the two slice positions are referred to as 'aorta' and 'lung'. The aorta slice was selected in order to have a comparable position for all volunteers. Considering the potential application in lung cancer patients with different tumor positions and overall lung anatomy, the performance of the methods needed to be investigated at different locations within the lung, thus justifying the additional lung slice. The position was chosen to cover a large variety of slices among the volunteers, showing different parts of the lung. For volunteers with large lung volumes, the lung slice was positioned posterior to the aorta slice, while for volunteers with smaller lung volumes a slice position anterior to the aorta was selected. In order to test reproducibility, both slice positions were scanned repeatedly and with different breathing patterns for each volunteer. After acquiring the image series once for each slice in normal free breathing, a break of about 15 min was taken inside the scanner before repeating the acquisition. To evaluate the robustness for different breathing patterns, the volunteers were then asked to breathe approximately 25% deeper. This instruction was only given to yield a realistic deeper breathing pattern. The actual diaphragm amplitude was not critical for this study. The same procedure was performed after a 15−20 min break outside the scanner, albeit with a reduced in-scanner break between the first and the second regular breathing scans, which was about 2−5 min. The second irregular breathing scan was acquired in shallower breathing. The first in-scanner break was chosen longer to allow the volunteers to get fully accustomed in the scanner and minimize anxiety related effects in the second scan. To limit the overall acquisition time to one hour, the second in-scanner break was shortened. In order to ensure a similar volunteer position after the outside-scanner break some precautions were taken during the first positioning. Pieces of tape were fixed to the volunteers' arms and the scanner table to mark the craniocaudal position and the relative position between volunteer and table based on the integrated laser positioning system. The x-, y- and z-coordinates of the scanner table in iso-center position were noted. For the setup after the break outside the scanner, the relative position between volunteer and table was found using the tape and again the laser system. The table was then moved to the exact coordinates used for the first acquisition. The scanning protocol and the used scan abbreviations are summarized in Table 1.

Image processing workflow

The in-house developed image processing workflow was fully implemented in Python (version 3.9). As shown by Bieri and Scheffler [41], the magnetization in bSSFP sequences approaches a steady-state after several TR periods. Similar to Bondesson et al. [31], the first 20 images were discarded as the steady state condition was not fulfilled. The acquired image series were firstly aligned with a deformable image registration using ANTs (Advanced Normalization Tools) [42] to a reference image in mid-position between full inspiration and full expiration using mutual information as optimization metric employing a three-level multiresolution registration strategy (25%, 50% and 100% of the original resolution). The reference image was automatically determined within the processing workflow. For this, the overall mean signal intensity was calculated for each image as well as the temporal average over these mean

Table 1 The scanning protocol for the volunteers, breathing patterns and used abbreviations (NB = normal breathing, IB = irregular breathing, aB = after Break) for each scan of the corresponding slice position

Scan	Slice	Breathing pattern	Abbreviation
1	3D Volume	Breath-hold	3D-scan
2	Aorta	Normal	Reference
3	Lung		
~ 15 min break inside the scanner			
4	Aorta	Normal	NB 2
5	Lung		
6	Aorta	~ 25% deeper	IB
7	Lung		
~ 10–20 min break outside the scanner			
8	Aorta	Normal	NB aB 1
9	Lung		
~ 2–5 min break inside the scanner			
10	Aorta	Normal	NB aB 2
11	Lung		
12	Aorta	Shallow	IB aB
13	Lung		

signal intensities. The image closest to this average was defined as the reference image and represents a motion state close to the mid-position. Based on this reference image, a manual segmentation of the lung was performed under the supervision of an experienced radiologist. The average temporal lung signal was used to determine the subject-specific cut-off frequency between 0.55−1.0 Hz to separate the ventilation and perfusion signals with a low- and high-pass Butterworth filter, respectively, which was applied forward and backwards to avoid the introduction of a phase shift. Since the Butterworth filter provides a good compromise between attenuation and phase response [43], it finds application in the processing of biomedical signals and was chosen in this study [44]. As shown by Bondesson et al. [31], a uniformly sampled signal with varying frequency is transformable into a non-uniformly sampled signal with constant frequency by defining virtual sampling times $\tilde{t}_n$ based on the instantaneous frequency. For this, a short-term Fourier transform was calculated and an edge-extraction algorithm (ssqueezepy package [45]) was applied to the 2D time-frequency representation to determine the instantaneous frequency of the ventilation and the perfusion signal and thus the respective virtual non-equidistant sampling times. These sampling times were then used to calculate the type-1 Non-uniform fast Fourier Transform (NuFFT) per pixel on the segmented lung. The ventilation- (Vw) and perfusion-weighted (Qw) maps were then generated by taking the maximum magnitude of the corresponding peak in the Fourier spectrum. The Vw- and Qw-maps are not quantitative but reflect the regional tissue density oscillation of the lung parenchyma due to ventilation in the former and the regional MR-signal intensity oscillation due to perfusion in the latter case. Diseased lung areas with altered parenchymal density, reduced pulmonary ventilation and/or poor perfusion would show less signal intensity in the Vw- and Qw-maps [30, 31]. The whole image processing workflow is illustrated in Fig. 1.

Normalization strategies

Diaphragm amplitude scaling factor

The idea of this normalization strategy is to introduce a multiplicative factor to normalize a scan acquired at a certain time point to a reference scan. With this, differences between scans due to breathing amplitude changes are compensated and the comparability within a longitudinal study improved. In order to correct for inter-scan differences in the Vw-maps due to variations in breathing amplitude, the relationship between lung ventilation signal and diaphragm position can be exploited. Relative changes in the average lung ventilation signal correspond to relative changes in lung volume and thus to the diaphragm motion [30]. The frame-wise lung ventilation signal is therefore normalized by the diaphragm position in this approach. The position of the diaphragm for each image frame was determined by placing a ROI around the diaphragm of the right lung and extracting the line profile along a vertical line through the diaphragm, as shown in Fig. 2A. Each of these line profiles was then fitted with a sigmoid function. The derivative of the sigmoid function was computed and its maximum position, i.e., the maximal intensity change, was used to determine the position of the diaphragm (Fig. 2B). Relative diaphragm positions were calculated with respect to the intermediate state. According to the definition used in this study, positive position values correspond to inspiration and negative values to expiration.

Correlating these diaphragm positions with the corresponding average lung ventilation signal in each image revealed a linear relationship. This allows to fit the correlation and to extract the slope dS/dx with the filtered lung ventilation signal S (step 4 in Fig. 1) and the relative diaphragm position x. This is examplarily shown for both slice positions of Volunteer 5 in Fig. 3. More examples of the correlation for different volunteers and scans can be found in the Additional File 1. This factor for a scan i is defined by:

$$\text{normalization factor}_i = \frac{\mathrm{dS_i}}{\mathrm{dx_i}} \cdot \frac{\overline{x}_{\text{ref,max}} - \overline{x}_{\text{ref,min}}}{\overline{S}_{i,\text{max}} - \overline{S}_{i,\text{min}}}, \quad (1)$$

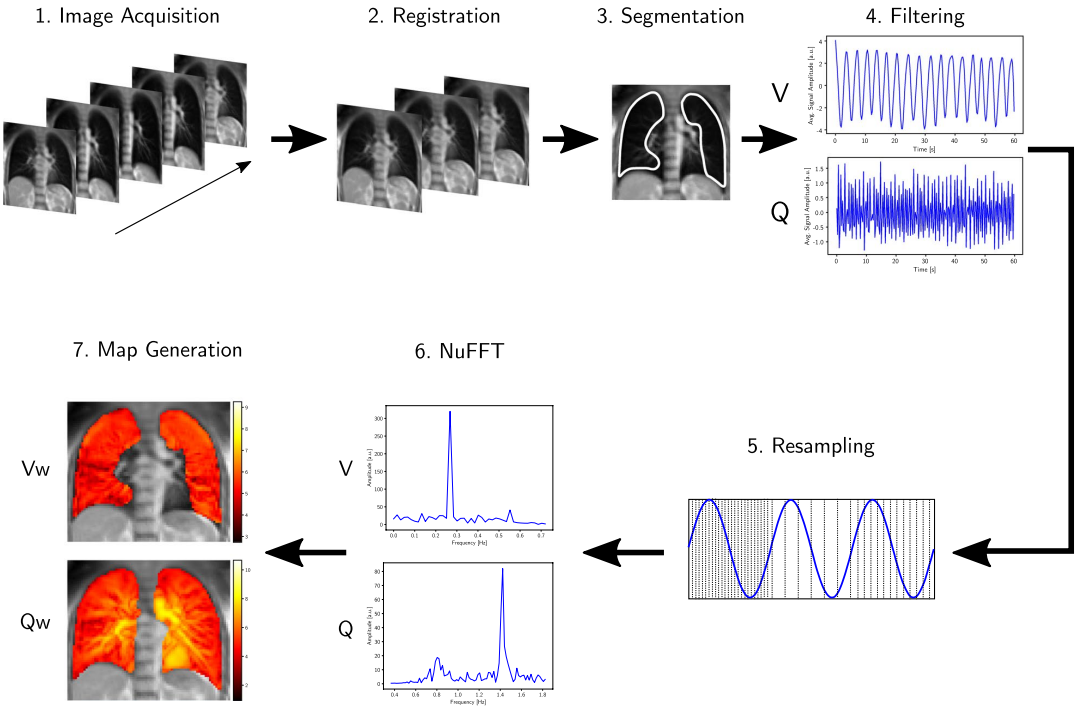

Fig. 1 Sketch of the image processing workflow. The workflow of the NuFD consists of the acquisition of the image series in free breathing (step 1), the image registration using ANTs (step 2) and a manual segmentation (step 3). The lung signal is low- and high-pass filtered to separate the ventilation (V) and perfusion signals (Q) (step 4), respectively. Resampling based on a short-term Fourier transform is performed on both signal components individually in order to transform uniformly sampled signals with varying frequency to non-uniformly sampled signals with constant frequency (step 5). Calculating the NuFFT pixel-wise for both ventilation and perfusion (step 6) and extracting the signal amplitude of the corresponding peak allows to generate V- and Q-weighted maps of the segmented lung that are then overlayed on the original image (step 7)

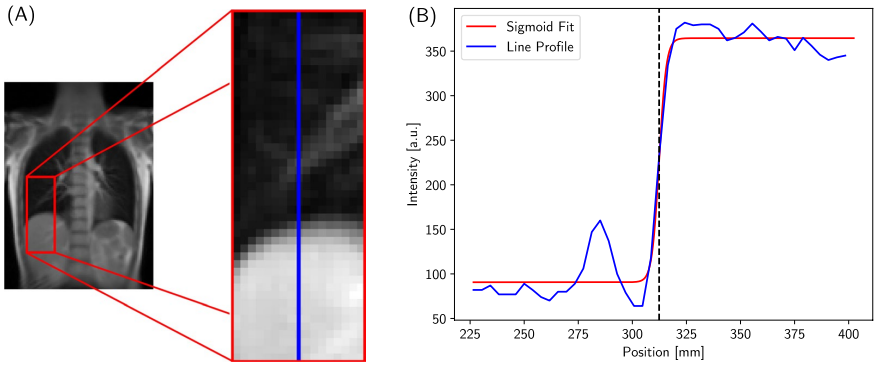

Fig. 2 Working principle of the diaphragm position extraction. The diaphragm positions used for the scaling factor-based normalization are extracted by first selecting a ROI (**A**) to get the line profile of the intensity for each frame in the image series. Each line profile (blue) is then fitted using a sigmoid function (red) as shown in (**B**). To determine the actual position of the diaphragm, the maximum of the derivative of the fitted sigmoid function is calculated, which is indicated by the black dashed line

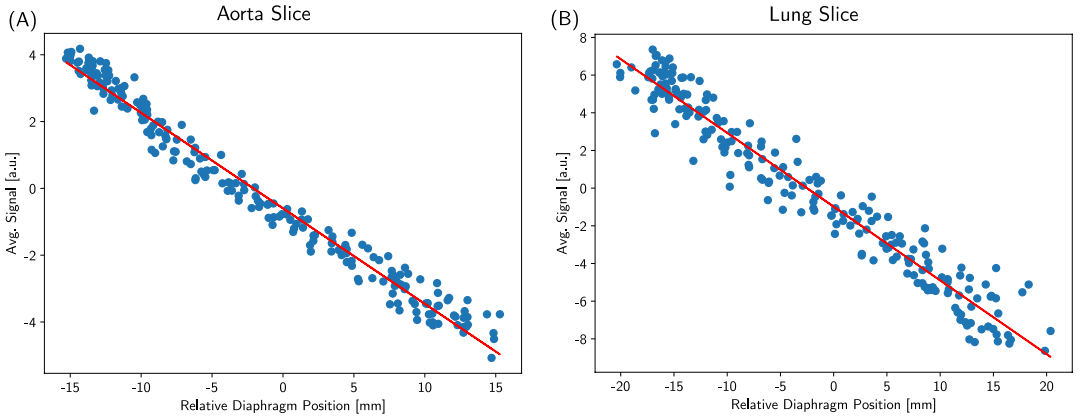

Fig. 3 The linear diaphragm position and lung signal correlation. The correlation between the relative diaphragm position and the average lung ventilation signal of each frame are exemplarily shown for a scan of the aorta (**A**) and lung slice (**B**). As a reference for the diaphragm positions, the mid position between full inspiration and full expiration was used, meaning that positive values describe the increase in lung volume and consequently negative values the decrease in lung volume. Regardless of the considered slice, a linear relationship between the two quantities is observable. The slope of the linear fit function depicted in red finds application in Eq. 1

where dS_i/dx_i is the slope of the linear fit and $\overline{S}_{i,\max}$ and $\overline{S}_{i,\min}$ are the mean maxima and minima of the filtered lung ventilation signal of scan i. The mean maxima and minima of the relative diaphragm positions in the reference scan are $\overline{x}_{\text{ref,max}}$ and $\overline{x}_{\text{ref,min}}$, respectively. A visual explanation of the parameters used in Eq. 1 and their extraction is given in the Additional File 2. Multiplying this resulting factor to the ventilation signal before the pixel-wise NuFFT (step 6 in Fig. 1) allows to correct for differences in the diaphragm amplitude between scan i and the reference scan.

Region-of-interest normalization

An alternative approach for the normalization of consecutive scans is to normalize the Vw- and Qw-maps of each scan pixel-wise by the average value within a chosen ROI where the lung parenchyma is assumed to be healthy. Assuming that breathing pattern changes affect all parts of the lung in a similar manner, this strategy diminishes the dependence on the breathing amplitude. The final normalized maps Γ_{norm} are then given by:

$$\Gamma_{\text{norm}} = \frac{\Gamma}{\overline{\Gamma}(\text{ROI})} \tag{2}$$

with $\Gamma = \text{Vw}, \text{Qw}$ the uncorrected maps and $\overline{\Gamma}(\text{ROI})$ the mean map value within the selected ROI of the same scan. In order to analyze the possible spatial and size dependence of the chosen region used for the normalization, six different positions (three in each lung), as shown in Fig. 4, were evaluated for two different square ROI sizes of 8×8 pixels (Fig. 4A) and 12×12 pixels (Fig. 4B).

Evaluation method

Map comparison

The Vw- and Qw-maps show only the relative signal differences within the lung and are therefore not quantitative. Thus, the aim of the normalization was to get Vw- and Qw-maps of similar intensity despite changes in the underlying breathing pattern and other potential inter-scan differences. In order to quantify the similarity, the mean value segmented lung was calculated for the maps of each scan and compared to the corresponding reference scan map. For healthy volunteers we assume that there should be no change in the maps from scan to scan. The absolute relative deviation δ_Γ of the mean value between unnormalized/normalized maps $\overline{\Gamma}_j$ of scans j and the map of the reference scan ($\overline{\Gamma}_{\text{ref}}$) is defined as:

$$\delta_\Gamma = \left| \frac{\overline{\Gamma}_{\text{ref}} - \overline{\Gamma}_j}{\overline{\Gamma}_{\text{ref}}} \right| \tag{3}$$

with j being a non-reference scan. In the following analysis, the firstly acquired aorta and lung image series served as the respective reference scans.

Statistical analysis

Since there is no reason to assume that the deviations of each scan's map from the corresponding reference are normally distributed for any normalization method, the statistical evaluation for significant differences between the ventilation normalization methods was performed using a Wilcoxon signed rank test (scipy.stats.wilcoxon

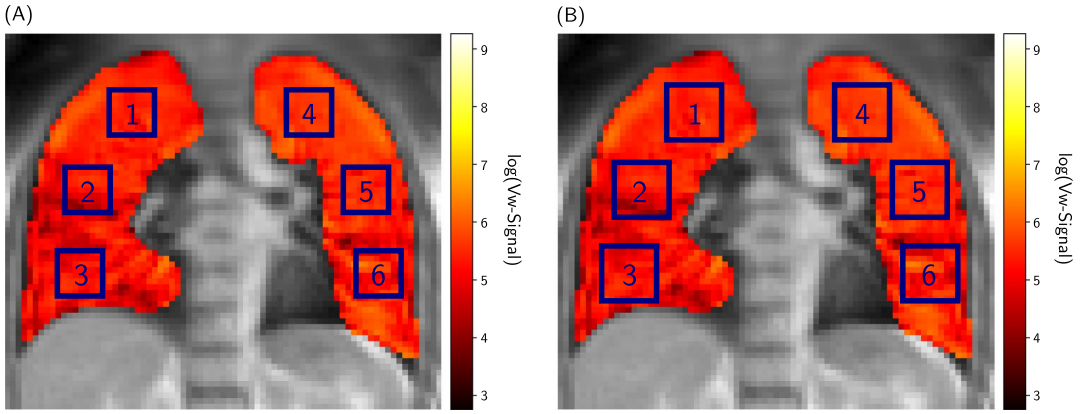

Fig. 4 The small and large ROI positions. The positions and numbering of the ROIs, whose mean ventilation value is used for the normalization of the ventilation-weighted maps, are displayed. In **A** the small ROIs with a size of 8 × 8 pixels and in **B** the large ROIs with 12 × 12 pixels are shown in blue with their assigned numbers starting from the top right lung. For presentation purposes, the ventilation maps were filtered using a Gaussian and then logarithmically plotted

package; version 1.7.2). Although the Vw- and Qw-map deviations can be positive as well as negative, due to over- or underestimation by the normalization techniques, only the absolute deviations were considered. This was to evaluate the performance of the methods solely in terms of magnitude of the deviation rather than direction. For this, each approach was compared to the maps of the uncorrected scans and against each other for both slices separately and the combined total of $n = 96$ scans at $\alpha = 0.05$.

Results

Feasibility

Figure 5 displays Vw- and Qw-maps along with the 2D MR image for two exemplary volunteer scans in normal and deep breathing without normalization. Large vessels and the heart in the lower left and right lung were excluded from the segmented lung used to calculate the Vw-maps. The maps show an overall homogenous intensity which is increased in the vessels for the Qw-maps. Using the same window for the Vw-maps in normal and

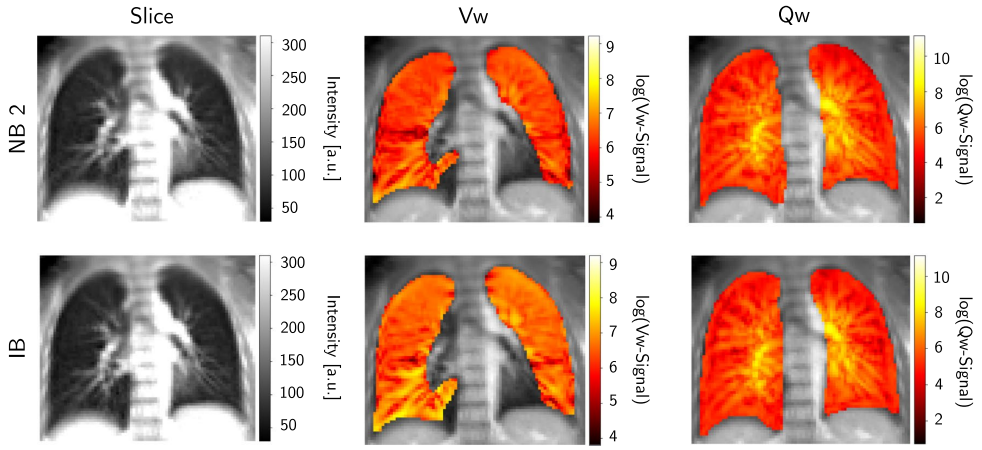

Fig. 5 Exemplary ventilation-(Vw) and perfusion-weighted (Qw) maps. The unnormalized V- and Q-maps for the normal (NB 2) and the first irregular breathing scan (IB, deep breathing) exemplarily presented for the aorta slice of Volunteer 4. The heart and large vessels were excluded from the segmentation of the Vw-maps. The maps were Gaussian filtered and logarithmically plotted

deep breathing results in differences in the overall intensity, as expected. Since the Qw intensity is mostly independent of the breathing pattern, the Qw-maps in Fig. 5 show no noticeable difference.

ROI size and position analysis

The ROI position and size dependency was investigated for both the Qw-maps and Vw-maps by using the ROIs specified in Fig. 4.

Ventilation

The median δ_V of all volunteers for each ROI location and slice position as well as the combined scans are listed in Table 2. Due to inconsistencies in the scanning protocol and the instructions given to Volunteer 1 resulting in unrealistic breathing patterns, both irregular breathing scans had to be excluded from the analysis. The boxplots showing the signed deviations for the small and large ROIs using the maps of all scans regardless of slice position can be found in the Additional File 3. For the small ROIs, the smallest and largest δ_V for both slice positions was achieved for ROI 5 (middle left lung) and ROI 4 (top left lung), respectively. These positions also coincide with the best and worst ROI positions found for the combined maps of both slice positions.

For the large ROIs, the best results were obtained using ROI 3 (bottom right lung) for the aorta slice and ROI 5 for the lung slice. The worst ROI was found to be ROI 4 (top left lung) for the aorta slice and ROI 1 (top right lung) for the lung slice. Combining the maps of both slice positions, ROI 6 and ROI 4 result in the smallest and largest deviations, respectively. Since the large ROIs presents overall smaller deviations compared to the small ROIs, the best (ROI 6) and worst (ROI 4) of the large ROIs were considered for further analysis of the ventilation.

Perfusion

In Table 3, the median δ_Q values of all volunteers for each ROI position and size are shown for both slice positions as well as the combined scans. While the uncorrected scans demonstrated

deviations below 10 %, in the case of the aorta slice, normalization using all ROI positions except ROI 1 and ROI 4 leads to further reduced deviations. The smallest δ_Q for the aorta slice was found for ROI 3 (small ROI) and

Table 2 The median values of the absolute deviations δ_V between each Vw-map mean and the reference presented here depending on the ROI location, the size and the slice position. The median deviations for the combined scans are also listed. All values are given in %

			Median δ_V over volunteers in %											
Uncorrected			ROI 1		ROI 2		ROI 3		ROI 4		ROI 5		ROI 6	
Aorta	Lung		Aorta	Lung	Aorta	Lung	Aorta	Lung	Aorta	Lung	Aorta	Lung	Aorta	Lung
24.9	35.6	Small	5.8	11.0	6.0	9.0	8.1	10.8	8.8	12.3	5.4	7.0	8.5	7.5
		Large	6.0	10.1	6.6	8.6	5.0	7.5	7.7	9.8	7.5	5.4	5.7	6.8
Median of aorta and lung slices														
29.5		Small	8.3		7.7		9.3		9.3		6.4		8.1	
		Large	7.4		7.0		6.5		8.6		6.6		5.7	

Table 3 The median values of the absolute deviations δ_Q of all volunteers Qw-maps for each ROI size and location as well as slice position. The median deviations for the combined scans are also listed. All values are given in %

			Median δ_Q over volunteers in %											
Uncorrected			ROI 1		ROI 2		ROI 3		ROI 4		ROI 5		ROI 6	
Aorta	Lung		Aorta	Lung	Aorta	Lung	Aorta	Lung	Aorta	Lung	Aorta	Lung	Aorta	Lung
11.0	8.8	Small	12.3	11.4	8.9	9.3	6.2	12.5	9.7	14.4	7.5	9.7	10.8	6.2
		Large	12.1	11.2	5.9	11.7	6.3	8.8	11.4	11.2	4.9	5.7	6.9	10.4
Median of aorta and lung slices														
10.2		Small	11.9		9.0		9.7		13.1		8.2		7.6	
		Large	11.6		7.6		8.2		11.3		5.3		7.9	

ROI 5 (large ROI). For the lung slice, only normalization using ROI 6 for the small squares and ROI 5 for the large squares achieved an improvement in δ_Q.

Normalization with ROI 6 for the small squares and ROI 5 for the large squares provided the best performance for the combination of all scans. Similar to the Vw-maps, the large ROIs lead to overall better results and were therefore considered for further analysis. Since using no correction showed better results than using the worst ROI (ROI 1), only ROI 5 as the best perfusion ROI was taken into account.

Reproducibility

Ventilation

The maps of the scans performed with different breathing patterns were each normalized using the diaphragm scaling factor and the ROI normalization strategy. In Fig. 6, the uncorrected and all corrected Vw-maps from both normalization strategies are shown for the selected aorta slice of Volunteer 5. As mentioned above, the best and worst ROI positions were considered for the ventilation analysis and therefore both are presented in Fig. 6. Looking at the Vw-maps of the uncorrected scans, especially IB and IB aB look noticeably different from the reference Vw-map when using the same window for the color map. The Vw-maps of IB (deep breathing) and IB aB (shallow breathing) display the expected higher and lower intensities, respectively, due to the specified breathing patterns.

Additionally, slight intensity differences are observable between the reference map and the Vw-maps of NB 2 and NB aB 2. These differences and especially the strongly increased signal intensity in the IB Vw-map are clearly reduced by the diaphragm-based scaling factor. Only a small underestimation is visually detectable for Volunteer 5 using this approach. Since the ROI-based approach also requires to normalize the reference map in order to validate the similarity of each map, a direct comparison to the uncorrected maps is not possible. All scans normalized with this method present only small differences in the Vw-maps. A slight overestimation of signal intensity is visible in the bottom right and middle left lung of the IB Vw-map normalized using the worst ROI position, whereas a minor underestimation of the whole lung can be noted using the best ROI position. Besides these observations, no other distinct differences in the performance between the best and the worst ROI are discernible.

Apart from the visual evaluation, the resulting normalized Vw-maps were also quantitatively analyzed per volunteer and between the volunteers. The mean ventilation was calculated for each map and compared to the reference map by determining δ_V from Eq. 3. The δ_V values

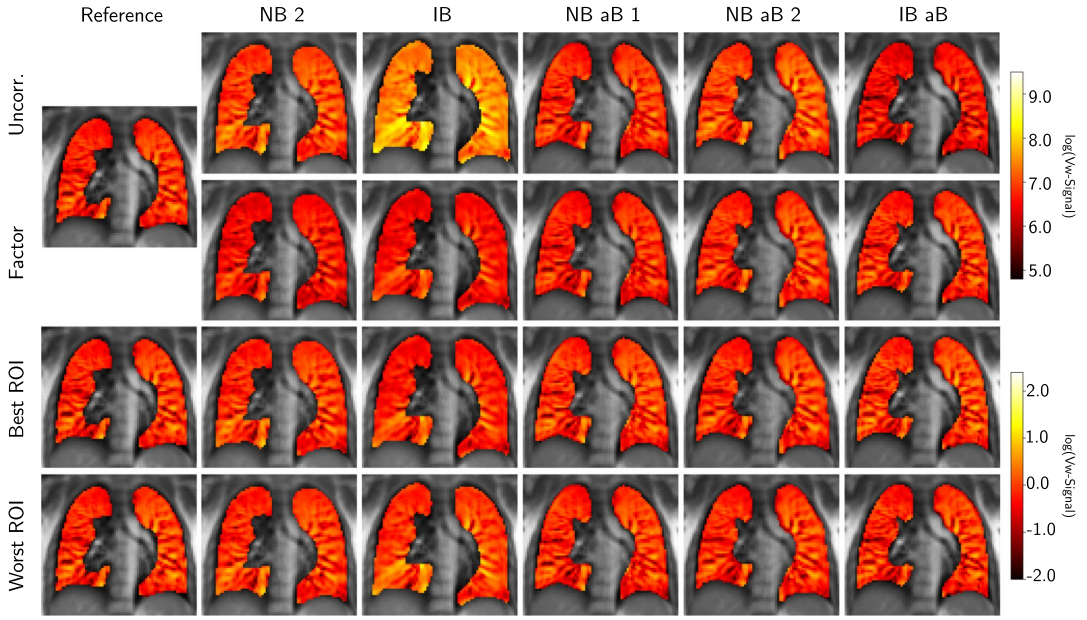

Fig. 6 Comparison of uncorrected and normalized Vw-maps. The performance comparison between the scaling factor, the best and worst ROI-based normalization technique and the uncorrected scans exemplarily illustrated for Vw-maps of the aorta slice scans of Volunteer 5

Table 4 The median δ_V values are listed in % for each volunteer and slice position using no correction, the normalization factor and the large ROIs 6 (best) and 4 (worst) for the ROI-based normalization

Volunteers	Median δ_V over scans in %							
	Uncorrected		Normalization factor		Best large ROI		Worst large ROI	
	Aorta	Lung	Aorta	Lung	Aorta	Lung	Aorta	Lung
Vol 1	12.8	34.9	16.5	21.7	9.3	16.4	16.1	34.0
Vol 2	16.8	23.1	11.6	3.7	10.3	9.3	29.6	11.7
Vol 3	45.5	37.8	16.7	7.4	5.7	4.4	7.5	3.4
Vol 4	17.0	6.2	3.2	14.1	13.2	3.9	12.9	7.9
Vol 5	23.6	44.2	9.7	4.6	5.0	4.4	5.1	12.2
Vol 6	36.5	52.7	13.3	11.4	3.3	2.8	6.7	8.6
Vol 7	26.9	17.9	1.5	4.0	1.8	3.7	22.0	12.4
Vol 8	38.2	50.0	8.1	7.1	6.0	13.4	2.8	5.6
Vol 9	22.7	18.1	12.0	11.5	2.3	22.0	10.6	11.6
Vol 10	25.7	29.5	7.6	13.6	6.5	8.4	5.0	13.6
Median	24.9	35.6	9.1	9.5	5.7	6.8	7.5	9.8
All Scans Median	29.5		9.1		5.7		8.6	

for each Vw-map of Volunteer 5, as shown in Fig. 6, can be found in the Additional File 4. The median δ_V in % for each slice position, volunteer and normalization method are listed in Table 4. Here, as described before, only the best and worst ROIs were considered. Except for Volunteer 1 (only normal breathing scans) using the normalization factor and the worst ROI, the aorta slice of Volunteer 2 using the worst ROI, the lung slice of Volunteer 4 using the normalization factor and the worst ROI, and the lung slice of Volunteer 9 using the best ROI, all deviations calculated for the normalized Vw-maps are clearly reduced compared to the deviations for the uncorrected maps.

This is also confirmed by the Wilcoxon signed rank test. All p-values indicated a significant improvement at $\alpha = 0.05$ and are shown in Table 5. Looking at the slice position dependency of the results, there are, except for Volunteers 2, 3 and 4, only minor differences observable between the δ_V of the aorta and the δ_V of the lung slices ranging from 0.5 to 10.9% using the normalization factor. This is also reflected in the median volunteer δ_V. However, for both considered ROIs, the normalization performance strongly varies between the slice positions for all volunteers with differences between the δ_V values of up to 19.7% for the best ROI and up to 17.9% for the worst ROI. Slightly better results were obtained for the normalization of the aorta slice compared to the lung slice for all three approaches. This also coincides with the observation that the overall unnormalized reproducibility of the results is slightly worse for the lung slices than for the aorta slices. Figure 7 displays the distributions of the deviations subdivided into aorta and lung, confirming the results from the absolute deviations in Table 4. Combining the Vw-maps of all scans regardless of the slice position, the best ROI leads to the lowest absolute deviation

Table 5 Results of the Wilcoxon signed rank test. The p values of the Wilcoxon signed rank test for the six different pairs are displayed for ventilation. For perfusion, only the comparison between unormalized and normalized using the best perfusion ROI was considered. The '*' indicates statistically significant differences between the compared techniques at =5%

Pairs	*p* value					
	Vw-map			Qw-map		
	Aorta	Lung	Total	Aorta	Lung	Total
Factor versus uncorr.	< 0.01*	< 0.01*	< 0.01*			
Best ROI versus uncorr.	< 0.01*	< 0.01*	< 0.01*	< 0.01*	0.02*	< 0.01*
Worst ROI versus uncorr.	< 0.01*	< 0.01*	< 0.01*			
Best ROI versus Factor	< 0.01*	0.18	0.02*			
Factor versus worst ROI	0.61	0.59	0.71			
Best ROI versus worst ROI	0.03*	0.12	0.01*			

Table 6 The median δ_Q values are listed in % for each volunteer and slice position. The uncorrected deviations are compared to the normalized deviations using the best perfusion ROI (ROI 5). The median volunteer $\boldsymbol{\delta}_Q$ for both slices and the combined scans are also presented.

Volunteers	Median δ_Q over scans in %			
	Uncorrected		Best large ROI	
	Aorta	Lung	Aorta	Lung
Vol 1	11.1	4.7	7.2	13.2
Vol 2	8.7	28.5	3.0	7.4
Vol 3	9.1	6.5	5.2	6.0
Vol 4	11.0	3.7	26.5	31.7
Vol 5	16.5	8.0	3.8	9.6
Vol 6	17.1	19.0	7.5	4.8
Vol 7	10.3	10.3	2.1	7.8
Vol 8	9.8	4.5	1.5	4.6
Vol 9	5.3	14.1	18.0	6.0
Vol 10	15.8	9.4	3.6	3.0
Median	11.0	8.8	4.9	5.7
All Scans Median	10.2		5.3	

of all three methods and is significantly better than the worst ROI and the normalization factor at $\alpha = 5\%$. No significant differences between the performances of the factor-based and the normalization using the worst ROI were found. Considering only the Vw-maps of the aorta slices, the best ROI shows significantly lower deviations than the factor-based normalization and the worst ROI, while for the lung slice there was no statistical difference in the performance between all approaches.

Perfusion

The Qw-maps of each scan were normalized using the best perfusion ROI (ROI 5) and the median deviation δ_Q from the reference map for each volunteer and slice position was calculated and compared to the uncorrected maps in Table 6. Using the normalization improved the Qw-map reproducibility in most cases except for the lung slice of Volunteer 1, both slices of Volunteer 4, the lung slice of Volunteers 5 and 8 as well as the aorta slice of Volunteer 9. The differences between the uncorrected and corrected δ_Q varied between 0.1% and 28.0%. Comparing the performances between aorta and lung slice for each volunteer, differences between δ_Q of up to 12% were observable for the normalized maps and up to 19.8% for the unnormalized maps. The reduction factor of about 2 between normalized and unnormalized maps was proven to be statistically significant by the Wilcoxon signed rank test (Table 5) for both slice positions as well as the maps of the combined scans.

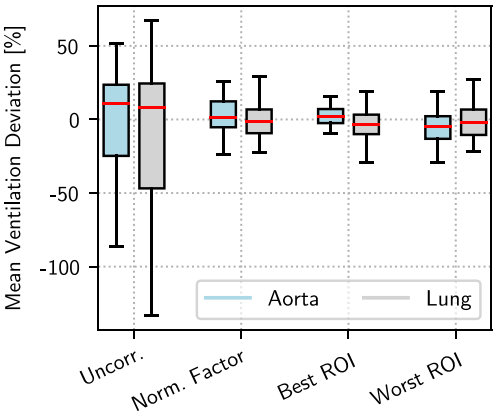

Fig. 7 The boxplots of the mean Vw-map deviations. The distributions of the signed mean deviations between each scan and the reference combined for all volunteers are illustrated for both slice positions as boxplots. The whiskers indicate 1.5 times the interquartile range (IQR). Outliers are not shown

Discussion

The feasibility of NuFD MRI at a 0.35 T MR-Linac was evaluated for ten healthy volunteers that underwent repeated scans using normal, deeper and shallower breathing at two different coronal slice positions. It was shown that differences in the breathing amplitude lead to differences in the ventilation-weighted maps, which made the introduction of two normalization strategies necessary. One strategy utilizes the linear relationship between the average lung signal and the diaphragm position to define a scaling factor that corrects for differences in the diaphragm amplitude between the reference scan and the scan that should be normalized. The second strategy is based on the normalization of the ventilation-weighted maps themselves rather than the ventilation signal by selecting a ROI and dividing the ventilation map pixel-wise by the mean value of the ventilation map within this ROI. Even though the perfusion-weighted maps are generally more reproducible due to the robustness of the physiological process, the ROI-based method was also used to normalize the perfusion maps.

Both the scaling-factor-based and the ROI-based normalization strategy show reasonable results for ventilation where the median δ_V was reduced from about 30% with no correction to below 10% for all investigated correction methods and without a considerable difference between different slice positions. For perfusion, using the ROI-based approach, the uncorrected deviations of about 10% could be further reduced to about 5%. Both techniques do not depend on any additional equipment such as spirometers and therefore provide a fast normalization

workflow that only requires the manual selection of a ROI around the diaphragm to capture the diaphragm motion for the scaling factor approach or at the chosen location in the Vw- or Qw-map for the the ROI-based approach. The idea of fitting the line profile in the former case and extracting the position at the maximum of the derivative of the fit makes use of the fact that the lung parenchyma has a much lower signal than other body parts and therefore causes strong intensity changes at the borders. This makes it a simple and computationally cheap technique compared to more complex feature tracking algorithms. The reason for using the diaphragm motion itself and not the signal of the diaphragm or the 2D lung area as proposed in [37] was to be less dependent on the quality of the image registration and difficulties with motion in and out of the scanned slice. Another advantage of using the presented approaches rather than normalizing the signal itself is that possible global changes in parts of the lung from one scan to another can still be observed, which makes the normalized NuFD suitable for longitudinal studies, such as radiotherapy treatment response monitoring of lung cancer patients.

Even though the results for different slice positions are fairly similar, comparing the volunteers revealed some performance differences for both techniques. Considering the potential integration into longitudinal studies, these robustness aspects have to be looked at in order to decide whether one approach might be better than the other, although there is a statistically significant advantage of using the best ROI. In the case of the scaling factor, one potential reason for these differences between volunteers are possible signal drifts that can cause an underestimation of the signal amplitude (see denominator in Eq. 1) which would lead to an overestimated corrected signal. Since all pixels are multiplied by the scaling factor for both methods, relative differences in the lung are not changed as displayed for the IB Vw-maps in Fig. 6. Additionally, the quality of the image registration plays an important role as it can not only influence the signal amplitude, but also the Vw- and Qw-maps as a consequence of misaligned lung structures. Hence both normalization strategies are affected. Due to differences in the structures visible in the selected slices and the overall intensity, it is reasonable to assume that the registration performance differs for each volunteer. Even though the quantitative influence of the image registration algorithm needs to be further investigated, care was taken during image registration. Visually unsatisfying registration results were re-evaluated and the corresponding scans re-registered with specifically optimized registration parameters. Since the focus of this study was on the analysis of feasibility and reproducibility of the NuFD and the introduced normalization techniques based on relative and not absolute quantitative values, only macroscopic differences in lung density and blood flow were of interest instead of small scale registration differences. The image registration might therefore influence absolute ventilation and perfusion map values, but have limited impact on the main findings of this study in terms of normalization and longitudinal reproducibility.

Another point that needs to be taken into account and concerns the general NuFD workflow is the manual segmentation. According to Willers et al. [46], inter- and intra-observer differences can occur for human observers. In our study this might translate in slight changes in the estimation of the mean value of the Vw- and Qw-maps, but is not expected to have a large impact. However, evaluating patients suffering from COPD and/or lung cancer, differences in the segmentation of the diseased areas has not only a more prominent impact on the mean pixel content of the Vw- and Qw-maps, but also the average lung signal and therefore the normalization factor. This makes it reasonable to potentially consider deep learning-based segmentation approaches for further evaluation.

Even though both approaches are easily realizable in most cases, there are also some limitations. The scaling factor-based normalization requires the tracking of the diaphragm motion. In patients suffering from uni- or bilateral diaphragmatic paralysis, the contraction of the lung is more or less performed by the thorax, namely the accessory muscles of inspiration [47]. In this case, the scaling factor approach would not be practicable and thus the ROI-based normalization would have to be applied. On the other hand, the ROI-based approach reveals not only a slight location and size dependency, but also in order to be able to see possible global changes in specific lung areas, the ROI needs to be positioned on a healthy part of the lung, which are not affected by irradiation in a longitudinal study. Normally, the 12×12 pixels ROI can be easily fitted into the lungs of lung cancer patients, but in special cases, it might be required to reduce the ROI size and to choose a position, which might not coincide with the best location at the lower left lobe and therefore degrades the overall normalization performance. In case of the perfusion, this might in some cases even lead to worse results using normalization compared to the uncorrected scans. However, in patients with severe COPD or CF, where either already the whole lung is affected or the lung function in a formerly healthy lung region worsens over the course of a longitudinal study, this can pose problems and therefore requires future tests to evaluate the applicability of this approach.

The utilization of different evaluation metrics and the novelty of the 0.35 T MR-Linac allows only a limited comparison of the presented study with previously published

studies. Lederlin et al. [48] reported a good reproducibility with average differences between ventilation maps of about 6% and between perfusion maps of about 3% obtained 24 h apart in healthy volunteers at a diagnostic 1.5 T MR-scanner using the original FD technique. One major limitation of [48] is that scans were acquired only in normal breathing, which could also explain the differences in mean deviations compared to the reported uncorrected deviations in this study. Similarly, Pöhler et al. [49] investigated the repeatability of ventilation and perfusion parameters derived from the PREFUL technique in healthy volunteers and COPD patients between two normal breathing scans acquired also at a 1.5 T MR-scanner. No significant differences were found between the two acquired scans for the investigated ventilation and perfusion parameters. The study conducted by Voskrebenzev et al. [37] on ventilation reproducibility assessment using a lung area-based and a spirometry-based normalization approach with FD-MRI considered normal and deep breathing scans as well as fixed frequency breathing and chose a more quantitative evaluation approach by calculating the fractional ventilation and the coefficient of variation. Similarly to this study, they found a strong dependence of the ventilation on the breathing amplitude and improved reproducibility by using a normalization strategy with an inter-volunteer coefficient of variation reduction from 0.23 (uncorrected) to 0.12 (normalized).

Generally, the NuFD is not only feasible, but also integrateable into the radiation therapy workflow at a 0.35 T MR-Linac due to the short acquisition time of about 1 min and the lack of contrast agents, respiratory triggering or patient compliance without prolonging treatments. Both normalization strategies improve the reproducibility and comparability of Vw- and Qw-maps in repeated scans.

Conclusions

In this work, the feasibility of NuFD as a non-contrast enhanced functional lung MRI method to assess ventilation and perfusion has been successfully demonstrated for a 0.35 T MR-Linac using an optimized 2D bSSFP sequence. In order to improve the reproducibility of the ventilation- and perfusion-weighted maps, two normalization techniques have been introduced and tested in a study with ten healthy volunteers, undergoing repeated scans at two different coronal slice positions and utilizing different breathing patterns. Both normalization strategies, the diaphragm amplitude scaling factor and the ROI-based approach, are able to correct for shallow and deep breathing. Averaged over the ten volunteers, median absolute deviations of 9.1% for the normalization factor-based and 5.7%/8.6% for the best/worst ROI-based approach were achieved for ventilation, which shows a clear reduction compared to the deviations of the uncorrected scans of 29.5%. Even though perfusion is in general a more regular and reproducible physiological process, using the best perfusion ROI further improved the reproducibility of the perfusion maps from 10.2 to 5.3%.

Abbreviations

aB	After break
ART	Adaptive radiotherapy
bSSFP	Balanced steady-state free precession
CF	Cystic fibrosis
COPD	chronic obstructive pulmonary disease
CT	Computed tomography
IB	Irregular breathing
IQR	Interquartile range
MRI	Magnetic resonance imaging
NB	Normal breathing
NuFD	Non-uniform Fourier Decomposition
NuFFT	Non-uniform Fourier Transform
Q	Perfusion
Qw	Perfusion-weighted
ROI	Region-of-interest
TE	Echo time
TR	Repetition time
V	Ventilation
Vw	Ventilation-weighted

Supplementary Information

The online version contains supplementary material available at https://doi.org/10.1186/s13014-023-02244-1.

Additional file 1: The linear diaphragm position and lung signal correlation. The correlation between the relative diaphragm position and the average lung ventilation signal of each frame are exemplarily shown for a normal breathing scan of Volunteer 4 for aorta (A) and lung slice (B), deep breathing scan of Volunteer 2 (aorta (C) and lung (D)) as well as the shallow breathing scans of Volunteer 8 (aorta (E), lung (F)). The slope of the linear fit function depicted in red finds application in Eq. 1.

Additional file 2: Explanatory figure for the diaphragm-based normalization. The mean maxima and minima of the relative diaphragm positions $\overline{x}_{\mathrm{ref,max}}$ and $\overline{x}_{\mathrm{ref,min}}$ are extracted from the corresponding reference scan. The filtered average lung ventilation signal of scan *i*, which should be normalized, is determined and the mean maxima and minima of this signal ($\overline{S}_{i,\mathrm{max}}$, $\overline{S}_{i,\mathrm{min}}$) calculated from the respective peaks. This filtered average lung ventilation signal is also correlated with the relative diaphragm positions of scan *i*. Fitting this correlation allows to extract the slope $\mathrm{d}S_i/\mathrm{d}x_i$.

Additional file 3: Boxplot comparison of ROI size and location for the Vw-maps. The boxplot for the signed mean deviations for each ROI using the 8×8 pixels square in (A) and the 12×12 pixels square in (B) compared to the uncorrected scans. Here, all scans of all volunteers were combined regardless of the slice position. The whiskers indicate 1.5 times the interquartile range (IQR). Outliers are not shown.

Additional file 4: The δ_V values of Volunteer 5 for the uncorrected Vw-maps as well as for the normalized Vw-maps using the diaphragm-based and the best and worst ROI-based normalization. The corresponding maps to these values are shown in Fig. 6.

Acknowledgements

The authors would like to thank Daniel Reitz for the clinical support during the data acquisition.

Author contributions
RK designed the scanning protocol, acquired the data, implemented the normalization strategies, performed the data analysis and prepared the manuscript. MR contributed to the data acquisition, supervision of the data analysis and reviewed the manusript. TG provided the base for the image processing pipeline, co-developed the idea for the normalization methods and supervised the data analysis. MJS optimized the bSSFP sequence protocol for the MR-Linac. IB implemented the manual segmentation. CE, SC and CB were included in the volunteer recruitment and study design and supported the ethics approval. GL and CK participated in all stages of this work from study design, volunteer recruitment, data acquisition, development of the normalization techniques, data analysis and the manuscript writing. JD initiated and designed the study, substantially contributed to the sequence and protocol optimization and oversaw all stages in the analysis process. All authors read and approved the final manuscript.

Funding
RK, TG, MJS, IB and JD acknowledge partial funding by the German Center for Lung Research (DZL), but received no specific grant for this research. MR was supported by the German Research Foundation (DFG) within the Research Training Group GRK2274.

Availability of data and materials
The datasets used and/or analysed during the current study are available from the corresponding author on reasonable request.

Declarations

Ethics approval and consent to participate
The data was acquired in the scope of a clinical study that was approved by the local ethics committee (study project number 21-0019). Written informed consent was provided and signed by all volunteers.

Consent for publication
Written informed consent was provided and signed by all volunteers.

Competing interests
The Department of Radiation Oncology of the University Hospital, LMU Munich has received research grants from ViewRay Inc. (Oakwood Village, OH, USA). ViewRay did not fund this study, was not involved and had no influence on the study design, the collection or analysis of data, on the writing of the manuscript, or the decision to submit the manuscript for publication. MJS is currently employed by Antaros Medical AB, BioVenture Hub, Mölndal, Sweden.

Author details
[1]Department of Radiology, University Hospital, LMU Munich, Munich, Germany. [2]Comprehensive Pneumology Center (CPC-M), Member of the German Center for Lung Research (DZL), Munich, Germany. [3]Department of Radiation Oncology, University Hospital, LMU Munich, Munich, Germany. [4]Antaros Medical AB, BioVenture Hub, Mölndal, Sweden. [5]Univ. Bordeaux, Centre de Recherche Cardio-thoracique de Bordeaux, F-33600 Pessac, France. [6]CHU Bordeaux, Service d'Imagerie Thoracique et Cardiovasculaire, Service des Maladies Respiratoires, Service d'Exploration Fonctionnelle Respiratoire, Unité de Pneumologie Pédiatrique, CIC 1401, F-33600 Pessac, France. [7]INSERM, U1045, Centre de Recherche Cardio-thoracique de Bordeaux, F-33600 Pessac, France. [8]German Cancer Consortium (DKTK), Munich, Germany.

Received: 20 January 2023 Accepted: 7 March 2023
Published online: 03 April 2023

References

1. Siegel RL, Miller KD, Fuchs HE, Jemal A. Cancer statistics, 2022. CA Cancer J Clin. 2022;72:7–33.
2. Green OL, Henke LE, Hugo GD. Practical clinical workflows for online and offline adaptive radiation therapy. Semin Radiat Oncol. 2019;29:219.
3. Belshaw L, Agnew CE, Irvine DM, Rooney KP, McGarry CK. Adaptive radiotherapy for head and neck cancer reduces the requirement for rescans during treatment due to spinal cord dose. Radiat Oncol. 2019;14:1–7.
4. Christiansen RL, Dysager L, Hansen CR, Jensen HR, Schytte T, Nyborg CJ, et al. Online adaptive radiotherapy potentially reduces toxicity for high-risk prostate cancer treatment. Radiother Oncol. 2022;167:165–71.
5. Yoon SM, Luterstein E, Chu FI, Cao M, Lamb J, Agazaryan N, et al. Clinical outcomes of stereotactic magnetic resonance image-guided adaptive radiotherapy for primary and metastatic tumors in the abdomen and pelvis. Cancer Med. 2021;10:5897–906.
6. Stowe HB, Price A, Henke LE, Laugeman E, Robinson CG, Green OL, et al. CT-guided adaptive radiotherapy (CT-ART) improves target coverage in hypofractionated radiation therapy for bladder cancer. Int J Radiat Oncol Biol Phys. 2022;114: e206.
7. Nierer L, Eze C, da Silva MV, Braun J, Thum P, von Bestenbostel R, et al. Dosimetric benefit of MR-guided online adaptive radiotherapy in different tumor entities: liver, lung, abdominal lymph nodes, pancreas and prostate. Radiat Oncol. 2022;17:1–14.
8. Eze C, Lombardo E, Nierer L, Xiong Y, Niyazi M, Belka C, et al. MR-guided radiotherapy in node-positive non-small cell lung cancer and severely limited pulmonary reserve: a report proposing a new clinical pathway for the management of high-risk patients. Radiat Oncol. 2022;17:1–8.
9. Hunt A, Hanson I, Dunlop A, Barnes H, Bower L, Chick J, et al. Feasibility of magnetic resonance guided radiotherapy for the treatment of bladder cancer. Clin Transl Radiat Oncol. 2020;25:46–51.
10. Mayinger M, Ludwig R, Christ SM, Bello RD, Ryu A, Weitkamp N, et al. Benefit of replanning in MR-guided online adaptive radiation therapy in the treatment of liver metastasis. Radiat Oncol. 2021;16:1–8.
11. Corradini S, Alongi F, Andratschke N, Belka C, Boldrini L, Cellini F, et al. MR-guidance in clinical reality: current treatment challenges and future perspectives. Radiat Oncol. 2019;14:1–12.
12. Crockett CB, Samson P, Chuter R, Dubec M, Faivre-Finn C, Green OL, et al. Initial clinical experience of MR-guided radiotherapy for non-small cell lung cancer. Front Oncol. 2021;11:617681.
13. Godley A, Zheng D, Rong Y. MR-linac is the best modality for lung SBRT. Appl Clin Med Phys. 2019;20:7–11.
14. Dunlop A, Mitchell A, Tree A, Barnes H, Bower L, Chick J, et al. Daily adaptive radiotherapy for patients with prostate cancer using a high field MR-Linac: initial clinical experiences and assessment of delivered doses compared to a C-arm Linac. Clin Transl Radiat Oncol. 2020;23:35–42.
15. Rogowski P, von Bestenbostel R, Walter F, Straub K, Nierer L, Kurz C, et al. Feasibility and early clinical experience of online adaptive MR-guided radiotherapy of liver tumors. Cancers. 2021;13:1523.
16. Dubec M, Datta A, Clough A, Buckley DL, Little RA, Berks M, et al. OC-0623 first-in-human clinical translation of oxygen-enhanced MRI onto an MR Linac. Radiother Oncol. 2022;170:S551–2.
17. Nejad-Davarani SP, Zakariaei N, Chen Y, Haacke EM, Hurst NJ, Siddiqui MS, et al. Rapid multicontrast brain imaging on a 0.35T MR-Linac. Med Phys. 2020;47:4067–76.
18. Habrich J, Boeke S, Nachbar M, Nikolaou K, Schick F, Gani C, et al. Repeatability of diffusion-weighted magnetic resonance imaging in head and neck cancer at a 1.5 T MR-Linac. Radiother Oncol. 2022;174:141–8.
19. Lawrence LSP, Chan RW, Chen H, Keller B, Stewart J, Ruschin M, et al. Accuracy and precision of apparent diffusion coefficient measurements on a 1.5 T MR-Linac in central nervous system tumour patients. Radiother Oncol. 2021;164:155–62.
20. Kooreman ES, Tanaka M, Beek LCT, Peters FP, Marijnen CAM, van der Heide UA, et al. $T_{1\rho}$ for radiotherapy treatment response monitoring in rectal cancer patients: a pilot study. J Clin Med. 2022;11:1998.
21. Yang Y, Cao M, Sheng K, Gao Y, Chen A, Kamrava M, et al. Longitudinal diffusion MRI for treatment response assessment: preliminary experience using an MRI-guided tri-cobalt 60 radiotherapy system. Med Phys. 2016;43:1369–73.
22. Cusumano D, Russo L, Gui B, Autorino R, Boldrini L, D'Erme L, et al. Evaluation of early regression index as response predictor in cervical cancer: a retrospective study on T2 and DWI MR images. Radiother Oncol. 2022;174:30–6.
23. Thorwarth D, Ege M, Nachbar M, Mönnich D, Gani C, Zips D, et al. Quantitative magnetic resonance imaging on hybrid magnetic resonance linear accelerators: perspective on technical and clinical validation. Phys Imaging Radiat Oncol. 2020;16:69–73.
24. Altes TA, Meyer CH, Mata JF, Froh DK, Paget-Brown A, Teague WG, et al. Hyperpolarized helium-3 magnetic resonance lung imaging of

non-sedated infants and young children: a proof-of-concept study. Clin Imaging. 2017;45:105–10.
25. Grist JT, Collier GJ, Walters H, Kim M, Chen M, Eid GA, et al. Lung abnormalities depicted with hyperpolarized xenon MRI in patients with long COVID. Radiology. 2022;305:709–17.
26. Couch MJ, Ball IK, Li T, Fox MS, Biman B, Albert MS. 19F MRI of the lungs using inert fluorinated gases: challenges and new developments. J Magn Reson Imaging. 2019;49:343–54.
27. Ohno Y, Hatabu H, Takenaka D, Adachi S, Cauteren MV, Sugimura K. Oxygen-enhanced MR ventilation imaging of the lung: preliminary clinical experience in 25 subjects. AJR Am J Roentgenol. 2001;177:185–94.
28. Matsuoka S, Uchiyama K, Shima H, Terakoshi H, Oishi S, Nojiri Y, et al. Effect of the rate of gadolinium injection on magnetic resonance pulmonary perfusion imaging. J Magn Reson. 2002;15:108–13.
29. Wielpütz MO. Making contrast material obsolete: functional lung imaging with MRI. Radiology. 2020;296:200–1.
30. Bauman G, Puderbach M, Deimling M, Jellus V, Chefd'hotel C, Dinkel J, et al. Non-contrast-enhanced perfusion and ventilation assessment of the human lung by means of Fourier decomposition in proton MRI. Magn Reson Med. 2009;62:656–64.
31. Bondesson D, Schneider MJ, Gaass T, Kühn B, Bauman G, Dietrich O, et al. Nonuniform Fourier-decomposition MRI for ventilation- and perfusion-weighted imaging of the lung. Magn Reson Med. 2019;82:1312–21.
32. Voskrebenzev A, Gutberlet M, Klimeš F, Kaireit TF, Schönfeld C, Rotärmel A, et al. Feasibility of quantitative regional ventilation and perfusion mapping with phase-resolved functional lung (PREFUL) MRI in healthy volunteers and COPD, CTEPH, and CF patients. Magn Reson Med. 2018;79:2306–14.
33. Fischer A, Weick S, Ritter CO, Beer M, Wirth C, Hebestreit H, et al. SElf-gated Non-Contrast-Enhanced FUnctional Lung imaging (SENCEFUL) using a quasi-random fast low-angle shot (FLASH) sequence and proton MRI. NMR Biomed. 2014;27:907–17.
34. Bauman G, Puderbach M, Heimann T, Kopp-Schneider A, Fritzsching E, Mall MA, et al. Validation of Fourier decomposition MRI with dynamic contrast-enhanced MRI using visual and automated scoring of pulmonary perfusion in young cystic fibrosis patients. Eur J Radiol. 2013;82:2371–7.
35. Veldhoen S, Weng AM, Knapp J, Kunz AS, Stäb D, Wirth C, et al. Self-gated non-contrast-enhanced functional lung MR imaging for quantitative ventilation assessment in patients with cystic fibrosis. Radiology. 2016;283:160355.
36. Capaldi DPI, Sheikh K, Eddy RL, Guo F, Svenningsen S, Nair P, et al. Free-breathing functional pulmonary MRI: response to bronchodilator and bronchoprovocation in severe asthma. Acad Radiol. 2017;24:1268–76.
37. Voskrebenzev A, Gutberlet M, Becker L, Wacker F, Vogel-Claussen J. Reproducibility of fractional ventilation derived by Fourier decomposition after adjusting for tidal volume with and without an MRI compatible spirometer. Magn Reson Med. 2016;76:1542–50.
38. Campbell-Washburn AE, Ramasawmy R, Restivo MC, Bhattacharya I, Basar B, Herzka DA, et al. Opportunities in interventional and diagnostic imaging by using high-performance low-field-strength MRI. Radiology. 2019;293:384.
39. Deimling M, Jellus V, Geiger B, Chefd'Hotel C. Time resolved lung ventilation imaging by Fourier decomposition. In: Proceedings of the International Society for Magnetic Resonance in Medicine, vol 16; 2008. p. 2639.
40. Hinsen M, Heiss R, Nagel AM, Lévy S, Uder M, Bickelhaupt S, et al. Lungenbildgebung in der Niederfeld-Magnetresonanztomographie. Radiologe. 2022;62:418.
41. Bieri O, Scheffler K. Fundamentals of balanced steady state free precession MRI. J Magn Reson Imaging. 2013;38:2–11.
42. Avants BB, Tustison NJ, Song G, Cook PA, Klein A, Gee JC. A reproducible evaluation of ANTs similarity metric performance in brain image registration. Neuroimage. 2011;54:2033–44.
43. Zumbahlen H. CHAPTER 8—analog filters. In: Zumbahlen H, editor. Linear circuit design handbook. Burlington: Newnes; 2008. p. 581–679.
44. AlHinai N. Chapter 1—introduction to biomedical signal processing and artificial intelligence. In: Zgallai W, editor. Biomedical signal processing and artificial intelligence in healthcare. London: Academic Press; 2020. p. 1–28.
45. John Muradeli. ssqueezepy, GitHub repository; 2020. https://github.com/OverLordGoldDragon/ssqueezepy.
46. Willers C, Bauman G, Andermatt S, Santini F, Sandkühler R, Ramsey KA, et al. The impact of segmentation on whole-lung functional MRI quantification: repeatability and reproducibility from multiple human observers and an artificial neural network. Magn Reson Med. 2021;85:1079–92.
47. Celli BR. Respiratory management of diaphragm paralysis. Semin Respir Crit Care Med. 2002;23:275–81.
48. Lederlin M, Bauman G, Eichinger M, Dinkel J, Brault M, Biederer J, et al. Functional MRI using Fourier decomposition of lung signal: Reproducibility of ventilation- and perfusion-weighted imaging in healthy volunteers. Eur J Radiol. 2013;82:1015–22.
49. Pöhler GH, Klimeš F, Behrendt L, Voskrebenzev A, Gonzalez CC, Wacker F, et al. Repeatability of phase-resolved functional lung (PREFUL)-MRI ventilation and perfusion parameters in healthy subjects and COPD patients. J Magn Reson Imaging. 2021;53:915–27.

Publisher's Note

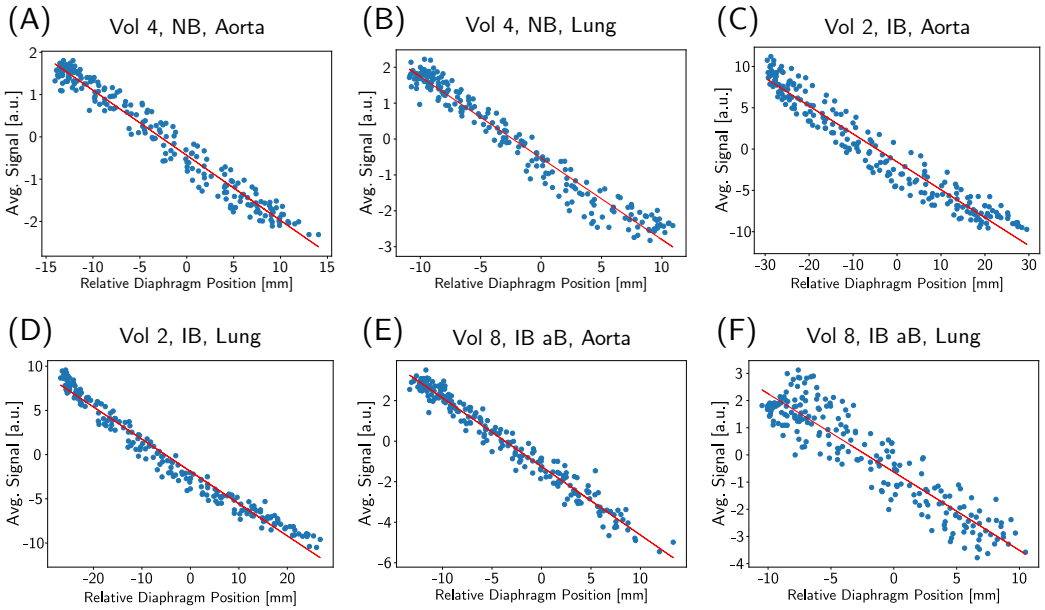

Additional File 1. The linear diaphragm position and lung signal correlation. The correlation between the relative diaphragm position and the average lung ventilation signal of each frame are exemplarily shown for a normal breathing scan of Volunteer 4 for aorta (A) and lung slice (B), deep breathing scan of Volunteer 2 (aorta (C) and lung (D)) as well as the shallow breathing scans of Volunteer 8 (aorta (E), lung (F)). The slope of the linear fit function depicted in red finds application in Eq. 1.

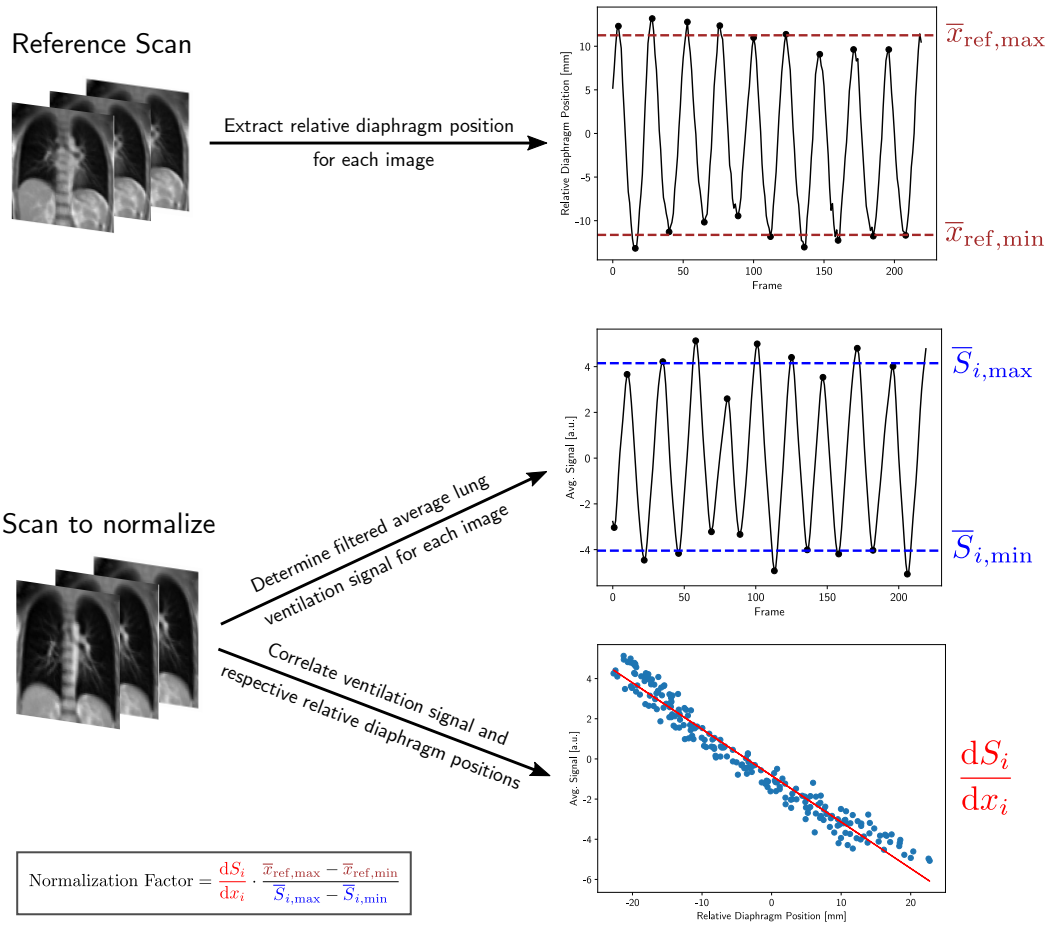

Additional File 2. Explanatory figure for the diaphragm-based normalization. The mean maxima and minima of the relative diaphragm positions $\overline{x}_{\mathrm{ref,max}}$ and $\overline{x}_{\mathrm{ref,min}}$ are extracted from the corresponding reference scan. The filtered average lung ventilation signal of scan i, which should be normalized, is determined and the mean maxima and minima of this signal ($\overline{S}_{i,\mathrm{max}}$, $\overline{S}_{i,\mathrm{min}}$) calculated from the respective peaks. This filtered average lung ventilation signal is also correlated with the relative diaphragm positions of scan i. Fitting this correlation allows to extract the slope $\frac{\mathrm{d}S_i}{\mathrm{d}x_i}$.

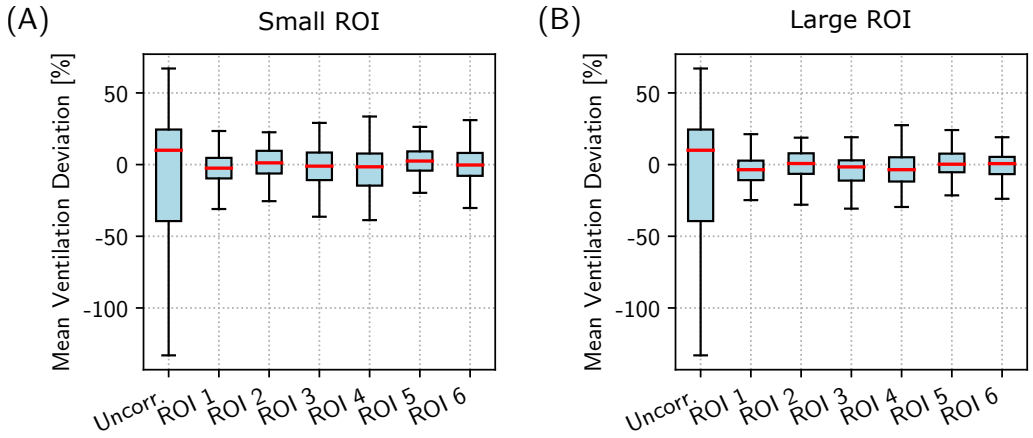

Additional File 3. Boxplot comparison of ROI size and location for the Vw-maps. The boxplot for the signed mean deviations for each ROI using the 8×8 pixels square in (A) and the 12×12 pixels square in (B) compared to the uncorrected scans. Here, all scans of all volunteers were combined regardless of the slice position. The whiskers indicate 1.5 times the interquartile range (IQR). Outliers are not shown.

	δ_V in %			
Scans	Uncorrected	Normalization Factor	Best Large ROI	Worst Large ROI
NB 2	23.6	20.4	3.7	2.4
IB	114.9	15.2	5.7	14.5
NB aB	0.43	9.7	5.0	4.4
NB aB 2	24.6	5.1	0.1	5.1
IB aB	23.0	1.5	7.3	5.5
Median	23.6	13.3	5.0	5.1

Additional File 4. The δ_V values of Volunteer 5 for the uncorrected Vw- maps as well as for the normalized Vw-maps using the diaphragm-based and the best and worst ROI-based normalization. The corresponding maps to these values are shown in Fig. 6.

4 | Publication II

Klaar, R., Rabe, M., Stüber, A. T., Hering, S., Corradini, S., Eze, C., Marschner, S., Belka, C., Landry, G., Dinkel, J., & Kurz, C. (2024). MRI-based ventilation and perfusion imaging to predict radiation-induced pneumonitis in lung tumor patients at a 0.35T MR-Linac. Radiotherapy and Oncology, 199, 110468. https://doi.org/10.1016/j.radonc.2024.110468

4.1 Summary of Publication II

After the feasibility of the NuFD technique and respective normalization strategies were successfully shown in healthy volunteers, the next step was to transfer the method to patients in a dedicated patient study (TOSCA Study). The objective for this study was to investigate whether ventilation and perfusion information (around the tumor) acquired over the fractionated treatment course at the MR-Linac could predict the occurrence of radiation-induced pneumonitis (RP) that develops at the earliest around 2-3 months after the end of treatment. A total of 23 patients that received lung radiotherapy at the MR-Linac of the Department of Radiation Oncology at the LMU University Hospital in Munich in 3-10 treatment fraction were additionally scanned with the coronal 2D-bSSFP sequence at the tumor position, required for the NuFD evaluation, after each fraction at most and at least after the first and last fraction. Functional parameters based on the difference in ventilation and perfusion between last and first fraction in the high-dose region (PTV, V20-PTV) and the whole tumor bearing lung were defined after normalization of the functional maps using a normalization strategy introduced in Publication I. The predictive power of the functional parameters was assessed and compared to the predictive performance of three clinical, dosimetric parameters (MLD, V20, mean dose in GTV). For this, ROC curves (after bootstrapping) were employed along with the corresponding AUC values for a quantitative comparison between the parameters. The relative change in ventilation in the tumor region (PTV) was identified as predictive of RP. Additionally, good predictive performance was found for the relative change in perfusion in the PTV and the ventilation in the high-dose region without the tumor (V20-PTV). All functional parameters defined in the target and high-dose region demonstrated better predictive qualities than the dosimetric parameters that are partially still used

as dose constraints in the treatment planning workflow.
With this publication, it was shown that the additional, but seamlessly integrable acquisition of non-contrast enhanced functional parameters over the treatment course could aid the identification of patients at risk of developing RP, which had not been demonstrated before. This could allow to monitor patients at risk more closely in order to counteract the disease early.

4.2 Contributions to Publication II

My contributions to this publication involved coordination of patient recruitment, scheduling and data acquisition, data curation, image processing, prediction model building and internal validation, result analysis, statistical analysis, result visualization and figure preparation as well as writing the original manuscript draft.
Together with PD Dr. rer. nat. Christopher Kurz and Dr. rer. nat. Moritz Rabe, I acquired 2D-cine MRI-scans of lung cancer patients directly after their treatment sessions at the 0.35 T MR-Linac of the Department of Radiation Oncology at the LMU University Hospital in Munich. I used the pipeline including the normalization strategies developed in Publication I to preprocess the data. I exported and anonymized the clinically used 3D-MRI baseline and setup scans for each patient and fraction and further preprocessed the images, which involved image registration of setup scans to respective baseline scans, localization of the 2D-cine MRI-scans in the 3D-MRI baseline scans and 2D-2D registration of the 2D-cine MRI-scans to the respective slice in the 3D-MRI baseline scan. I defined the parameters to be assessed for their potential qualities to predict RP collectively with Prof. Dr. Guillaume Landry, PD Dr. rer. nat. Christopher Kurz and Dr. rer. nat. Moritz Rabe. After consulting with Anna Theresa Stüber regarding statistical approaches, I performed a univariate prediction analysis including bootstrapping for the defined parameters. The results were critically discussed together with Prof. Dr. Guillaume Landry, Prof. Dr. med. Julien Dinkel, PD Dr. rer. nat. Christopher Kurz and Dr. rer. nat. Moritz Rabe. I prepared workflow and result plots to visualize the methodology and the results. I wrote the original manuscript draft and reviewed and edited the manuscript in cooperation with all co-authors.

4.3 Publication II

Radiotherapy and Oncology 199 (2024) 110468

Contents lists available at ScienceDirect

Radiotherapy and Oncology

journal homepage: www.thegreenjournal.com

Original article

MRI-based ventilation and perfusion imaging to predict radiation-induced pneumonitis in lung tumor patients at a 0.35 T MR-Linac

Rabea Klaar [a,b,*], Moritz Rabe [c], Anna Theresa Stüber [a,d,e], Svenja Hering [c], Stefanie Corradini [c], Chukwuka Eze [c], Sebastian Marschner [c], Claus Belka [c,f,g], Guillaume Landry [c], Julien Dinkel [a,b,1], Christopher Kurz [c,1]

[a] Department of Radiology, LMU University Hospital, LMU Munich, Munich, 81377, Germany
[b] Comprehensive Pneumology Center (CPC-M), Member of the German Center for Lung Research (DZL), Munich, 81377, Germany
[c] Department of Radiation Oncology, LMU University Hospital, LMU Munich, Munich, 81377, Germany
[d] Department of Statistics, LMU Munich, Munich, 80539, Germany
[e] Munich Center for Machine Learning (MCML), Munich, 80539, Germany
[f] German Cancer Consortium (DKTK), partner site Munich, a partnership between DKFZ and LMU University Hospital Munich, Munich, 80336, Germany
[g] Bavarian Cancer Research Center (BZKF), Munich, 80336, Germany

ARTICLE INFO

Keywords:
MR-linac
Functional imaging
Ventilation
Perfusion
Low-field MRI
Radiation-induced pneumonitis
Prediction
Biomarker

ABSTRACT

Background and purpose: Radiation-induced pneumonitis (RP), diagnosed 6–12 weeks after treatment, is a complication of lung tumor radiotherapy. So far, clinical and dosimetric parameters have not been reliable in predicting RP. We propose using non-contrast enhanced magnetic resonance imaging (MRI) based functional parameters acquired over the treatment course for patient stratification for improved follow-up.
Materials and methods: 23 lung tumor patients received MR-guided hypofractionated stereotactic body radiation therapy at a 0.35 T MR-Linac. Ventilation- and perfusion-maps were generated from 2D-cine MRI-scans acquired after the first and last treatment fraction (Fx) using non-uniform Fourier decomposition. The relative differences in ventilation and perfusion between last and first Fx in three regions (planning target volume (PTV), lung volume receiving more than 20 Gy (V20) excluding PTV, whole tumor-bearing lung excluding PTV) and three dosimetric parameters (mean lung dose, V20, mean dose to the gross tumor volume) were investigated. Univariate receiver operating characteristic curve - area under the curve (ROC–AUC) analysis was performed (endpoint RP grade ≥ 1) using 5000 bootstrapping samples. Differences between RP and non-RP patients were tested for statistical significance with the non-parametric Mann–Whitney U test ($\alpha = 0.05$).
Results: 14/23 patients developed RP of grade≥1 within 3 months. The dosimetric parameters showed no significant differences between RP and non-RP patients. In contrast, the functional parameters, especially the relative ventilation difference in the PTV, achieved a p-value < 0.05 and an AUC value of 0.84.
Conclusion: MRI-based functional parameters extracted from 2D-cine MRI-scans were found to be predictive of RP development in lung tumor patients.

Introduction

Radiation therapy, and in particular stereotactic body radiation therapy (SBRT), serves as standard of care for most patients suffering from inoperable non-small cell lung cancer (NSCLC) or lung metastasis [1,2]. Many technical advances have been made to decrease the burden on the patient while improving tumor control and treatment outcome [3–7]. In particular, the clinical introduction of magnetic resonance-guided radiotherapy (MRgRT) using MR-linacs has been beneficial for the treatment of lung cancer patients [8–10]. The integrated MRI-scanner provides not only improved soft-tissue contrast, but also allows for respiratory-gated dose delivery, based on cine MRI-scans, as well as adaptation of treatment plans to the daily anatomy, thus enabling highly accurate treatment in few treatment fractions (Fxs) [3,11,12]. Despite these technical developments, radiation-induced pneumonitis (RP) still remains a common side effect of lung tumor radiotherapy, with reported incidence of 10–17% [3,13] for grade ≥ 2 RP in MRgRT.

* Correspondence to: Marchioninistr. 15, 81377 Munich, Germany .
E-mail address: rabea.klaar@med.uni-muenchen.de (R. Klaar).
[1] The authors contributed equally to this work.

https://doi.org/10.1016/j.radonc.2024.110468
Received 2 April 2024; Received in revised form 10 July 2024; Accepted 31 July 2024
Available online 5 August 2024

RP is thus a non-negligible adverse effect which occurs at the earliest 6 weeks after end of treatment and is usually diagnosed using computed tomography (CT) scans 2–3 months after treatment [14,15].

Finding parameters or biomarkers capable of predicting the occurrence of RP is therefore expected to be beneficial to patients. Initial candidates were clinically motivated parameters such as tumor-related factors, patient-related factors or dosimetric parameters such as the mean lung dose (MLD) and the volume receiving more than 20 Gy (V20) [15]. Even though these parameters are considered during the dose optimization, variable predictive power has been reported in relatively small patient cohorts [16,17]. Recently, the focus of research has shifted towards the potential integration of functional information in clinical routine for treatment monitoring [18–20], investigation of dose–response relationships [21–24], function-informed treatment planning or functional-guided radiotherapy [25–29], offering new lung function-based parameters for RP patient stratification. So far, most studies focused on the pre-treatment acquisition of 4DCTs for the extraction of ventilation maps [16,17,30], SPECT/CT-scans for lung perfusion [31–33] or PET/CT imaging to estimate lung ventilation and/or perfusion [26,34,35]. Correlating the highly functional regions of the lung with the dose and defining parameters based on the MLD and V20 in these regions were reported to be more predictive than anatomical dosimetric parameters [36].

These studies have been conducted for conventional radiotherapy techniques and required additional scans at different imaging devices relying on ionizing radiation. With MR-linacs, MRI-based functional information can be acquired directly during the treatment session, thus reducing logistical challenges, costs and the overall patient burden [37]. A technique called non-uniform Fourier decomposition (NuFD) allows the extraction of relative ventilation and perfusion information from cine MRI-scans at MR-linacs without the need of contrast agents, dedicated equipment or patient compliance [20].

The goal of this imaging biomarker discovery study was to define ventilation- and perfusion-based parameters extracted using the NuFD method acquired at the start and end of treatment at a low-field MR-linac for predicting the occurrence of grade ≥ 1 RP 6–12 weeks after the end of treatment.

Materials and methods

Patient cohort

A total of 23 patients with 24 lung lesions who received hypofractionated online adaptive MRgRT with gated beam delivery from June 2021 to April 2024 at the 0.35 T MR-Linac (MRIdian, ViewRay Inc., Cleveland, Ohio) of the LMU University Hospital Munich were included in this prospective study (Table 1). The identification of correlations between RP development and changes in MRI-based ventilation and perfusion between the first and the last Fx was the primary endpoint. Ethical approval (project number 21–0019) was granted by the local ethics committee and written informed consent was signed by all patients. Requirements for the inclusion in the study were SBRT in at least three treatment Fx and no infracarinal lesions. One patient received simultaneous SBRT for two targets (primary tumor and metastasis).

Table 1
Patient characteristics for the 23 patients. Unless indicated otherwise, all numbers reported in the table are in units of patient numbers. The fractionation is given as physical dose. *GTV: Gross tumor volume, NSCLC: Non-small cell lung cancer, RP: Radiation-induced pneumonitis.*

Age [yrs]	Median	63
	Range	38–81
Sex	Male	9 (39%)
	Female	14 (61%)
Fractionation	3 × 13.5 Gy	6 (25%)
	3 × 15.0 Gy	4 (17%)
	5 × 8.0 Gy	1 (4%)
	5 × 10.0 Gy	1 (4%)
	8 × 7.5 Gy	2 (8%)
	10 × 4.0 Gy	1 (4%)
	10 × 5.0 Gy	8 (33%)
GTV Size [cm^3]	Median	9.8
	Range	1.6–71.4
Tumor Location	Superior Lobe Left	11 (48%)
	Superior Lobe Right	5 (22%)
	Inferior Lobe Left	5 (22%)
	Inferior Lobe Right	3 (13%)
Type of Cancer	Primary Lesion	6 (25%)
	Metastasis	18 (75%)
NSCLC Stage	IA-B	3
	IIA	1
	IVA-B	2
RP Grade	Grade 0	9 (39%)
	Grade 1	10 (45%)
	Grade 2	4 (17%)

Image processing workflow

In addition to 3D balanced steady-state free precession (bSSFP) MRI-scans (sequence parameters in the Supplementary Material 1) used in the MRgRT workflow [12], 2D+*t* coronal cine MRI-scans intersecting the tumor were performed in free-breathing directly after the first (Fx1) and last (FxN) treatment fractions using a bSSFP sequence with the following parameters: TE = 1.02 ms, TR = 2.42 ms, pixel size = 3.91 × 3.91 mm^2, slice thickness = 20 mm, FA = 70.0°, FOV = 300 × 300 mm^2, matrix = 128 × 128, frame rate = 3.68 images/s, TA = 1.1 min for 240 images, receiver bandwidth = 710.0 Hz/pixel. Ventilation (Vent) and perfusion (Perf) maps were generated using the NuFD technique as described in Klaar et al. [20]. An additional automatic breath-hold detection and removal step was included similar to Lombardo et al. [38] using the frame-wise diaphragm positions determined following [20].

In order to associate the target/irradiated volume and specifically the high-dose regions with the functional maps generated for Fx1 and FxN, the 3D setup MRI-scans were rigidly registered to the baseline MRI-scan. This allowed to overlay the dose distribution as well as the target delineations on the Fx MRI-scans. From these registered 3D MRI-scans, coronal slices were extracted by finding the slice with the largest PTV (GTV + isotropic 5 mm margin) extent. To achieve a slice thickness similar to the 2D cine MRI-scans and aid the image registration, an averaged coronal slice was calculated by averaging over slices in anterior and posterior direction from the originally selected slice position. The reference frame of the 2D-cine MRI-scans was then deformably registered to the averaged coronal slice downsampled to the in-plane cine-MRI resolution using Plastimatch [39]. The registration quality was visually assessed in each step and if necessary individually optimized. The application of the respective deformation fields allowed to overlay the baseline GTV and PTV structures and planned dose distribution onto the Vent- and Perf-maps of Fx1 and FxN. For the patient that received simultaneous radiotherapy for several targets, it was automatically checked whether the additional targets were within slices used for the slice averaging. If this was the case, a joint PTV was used for the definition of the parameters. Due to FOV limitations, a small part of the upper lungs was cropped in the baseline and 3D setup MRI-scans of one patient with large lung volume and a lesion in the lower left lung. The corresponding functional maps were cropped accordingly resulting in a slightly reduced lung area available for analysis distant to the high-dose region. A summary of the workflow is illustrated in Fig. 1. An example of the defined regions for the calculation of the functional parameters can be found in Supplementary Figure 2.

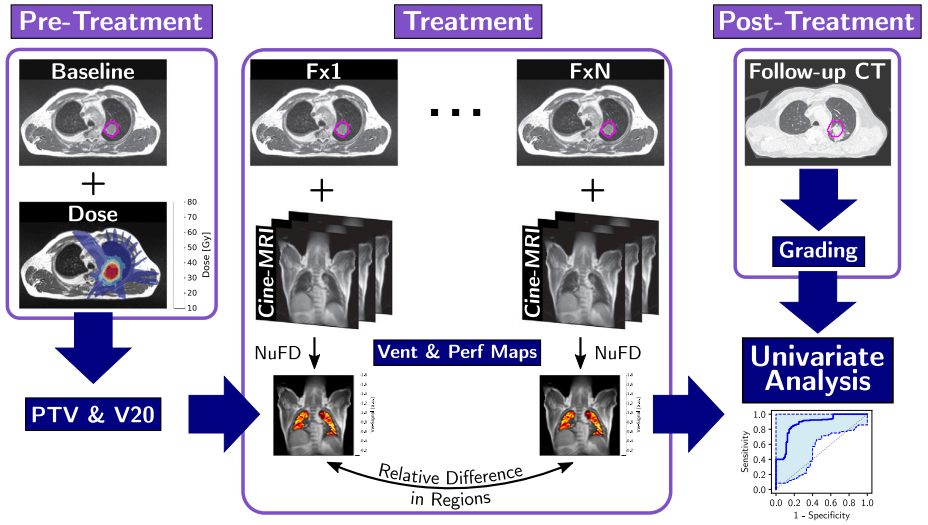

Fig. 1. Sketch of the image acquisition and processing workflow. The PTV (pink solid line) and the V20 were extracted from the baseline 3D MRI-scan, acquired for treatment planning. In addition to the Fx setup MRI-scans, 2D coronal cine-MRI image series at the tumor position were obtained directly after the first (Fx1) and last (FxN) fraction in free-breathing. Non-uniform Fourier decomposition (NuFD) was applied to both image series and ventilation (Vent) and perfusion (Perf) maps were generated. Relative differences between the respective functional maps were calculated in the PTV, the V20 without the PTV and the tumor bearing lung without the PTV and defined as prediction parameters. Based on follow-up CT-scans performed at least six weeks after the end of treatment, all patients were retrospectively graded regarding RP. Using this information, the performance of each parameter to predict grade ≥ 1 RP was investigated.

Parameter definition

Using the functional Vent- and Perf-maps retrieved at the start and the end of each patient's treatment as well as the baseline treatment planning dose and target volume, three different regions were considered: the PTV, the V20 without PTV and the whole tumor bearing lung (TLung) without PTV. The mean values of the Vent- and Perf-maps were calculated within these regions and normalized with the respective mean values of the non-tumor bearing lung. To account for the extent of the tumor over several slices, the maximum intensity projection (MIP) in anterior-posterior direction was used for both the PTV and the V20 regions. To be robust against registration uncertainties, an additional margin of one pixel in the cine-MRI resolution (3.91 mm) was added to the PTV contours. To compare the non-quantitative parameters between patients, the relative difference of FxN to Fx1 was calculated for the mean values of the Vent- and Perf-map in the different regions for each patient:

$$\Gamma_{\chi} = \frac{\overline{\Gamma}_{\chi,\mathrm{N}} - \overline{\Gamma}_{\chi,1}}{\overline{\Gamma}_{\chi,1}} \tag{1}$$

with $\Gamma = [\mathrm{Vent}, \mathrm{Perf}]$ and $\chi = [\mathrm{PTV}, \mathrm{V20\text{-}PTV}$ and $\mathrm{TLung\text{-}PTV}]$, resulting in six functional parameters for analysis ($\mathrm{Vent}_{\mathrm{PTV}}$, $\mathrm{Vent}_{\mathrm{V20-PTV}}$, $\mathrm{Vent}_{\mathrm{TLung-PTV}}$, $\mathrm{Perf}_{\mathrm{PTV}}$, $\mathrm{Perf}_{\mathrm{V20-PTV}}$, $\mathrm{Perf}_{\mathrm{TLung-PTV}}$). Additionally, the MLD, the V20 and the mean dose to the GTV were determined. The MLD was calculated excluding the GTV and both MLD and V20 were converted into radiobiological equivalent doses of 2 Gy (EQD2) based on the linear-quadratic model using $\alpha/\beta = 3$ Gy for lung tissue to account for the different fractionation schemes [13]. The dose to the GTV was the physical dose.

Grading

All patients underwent CT-scans as part of the standard follow-up procedure at a median time of 11 weeks after the end of treatment. All CT-scans were assessed in terms of radiation-induced changes such as ground-glass opacities and consolidations in the area around the irradiated lesion by an experienced radiologist. Two exemplary patient scans showing radiation-induced changes on the lung parenchyma and two patient scans showing no corresponding changes can be found in Supplementary Figure 3. Including the patients' general condition and potential symptoms assessed during regular follow-up, the RP grading was performed based on the National Cancer Institute Common Terminology Criteria for Adverse Events (NCI-CTCAE) version 5.0 [40].

Statistical analysis

The predictive performance of each of the nine parameters (six functional, three clinical) was assessed individually with a univariate analysis based on manual thresholding with patients developing RP grade ≥ 1 as endpoint. The receiver operating characteristic (ROC) curve and the area under the curve (AUC) were determined. Bootstrapping with 5000 samples was performed to validate the parameters internally and the median ROC curve and AUC values along with the according the 95% confidence intervals (CI) were calculated. To test for significant differences between the RP and non-RP patient groups, the non-parametric Mann–Whitney U test was used with $\alpha = 0.05$.

Results

Out of the 23 patients in the study, 9 patients (39%) had no indication of RP and were classified with grade 0. 14 patients (61%) showed signs of RP, with 10 patients (45%) classified with grade 1 and 4 patients (17%) with grade 2 RP. The baseline 3D MRI, Vent- and Perf-maps at Fx1 and FxN, as well as the follow-up CT for an exemplary patient that developed RP and a patient without RP are shown in Fig. 2. Based on the grading, the parameter value distributions for the two patient groups are shown in Fig. 3 and compared statistically. The more localized functional parameters based on the V20-PTV and the PTV region (subplots E,F,I) allowed separation between RP and non-RP patients with $\mathrm{Vent}_{\mathrm{PTV}}$ (subplot F) showing significant differences

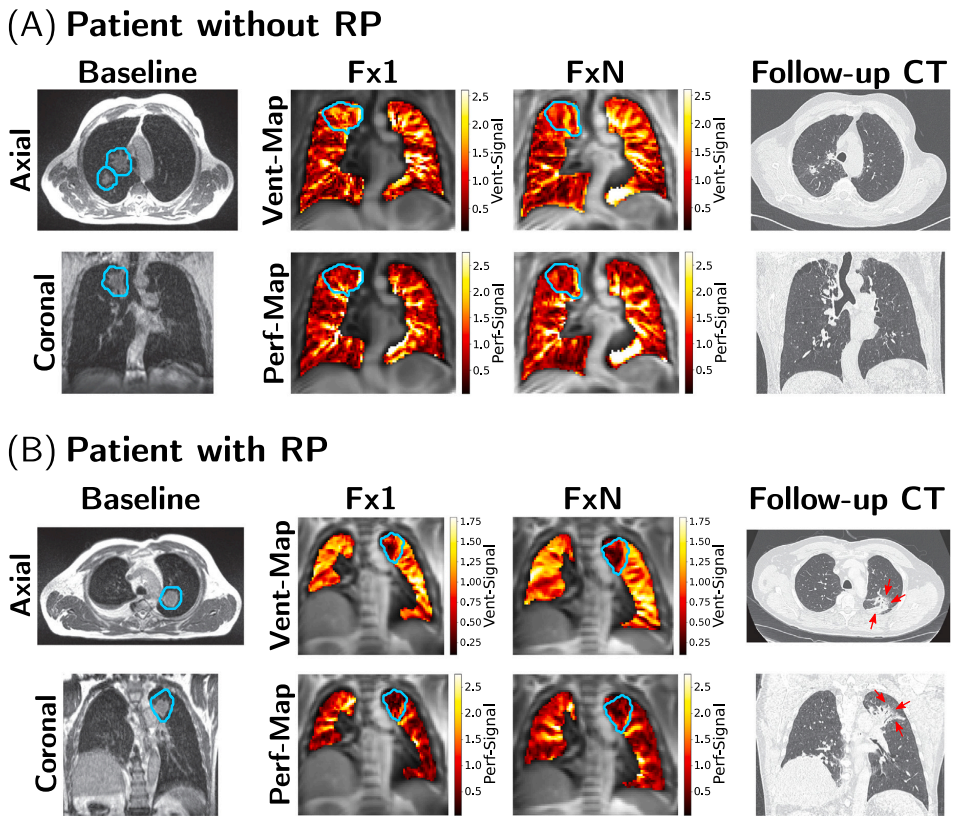

Fig. 2. Two exemplary patients. All images (baseline MRI-scan, Vent- and Perf-maps of first (Fx1) and last (FxN) treatment fraction, follow-up CT) of an exemplary patient without acute RP (A) and a patient that developed acute grade 1 RP (B) are shown. The PTV contours are depicted in light-blue and findings indicating RP are highlighted with red arrows. The patient in subfigure A received simultaneous SBRT for two PTVs.

Table 2
The AUC values. The median AUC values of the univariate ROC–AUC analysis with 5000 bootstrapping samples are listed for the three dosimetric and the six functional parameters. The upper and lower bounds of the 95% confidence intervals are given in brackets.

Biomarkers		AUC
Dosimetric	MLD	0.52 [0.22, 0.75]
	V20	0.54 [0.21, 0.75]
	Mean Dose GTV	0.69 [0.46, 0.90]
Functional	$Vent_{PTV}$	0.84 [0.61, 1.00]
	$Vent_{V20-PTV}$	0.71 [0.47, 0.91]
	$Vent_{TLung-PTV}$	0.52 [0.21, 0.78]
	$Perf_{PTV}$	0.73 [0.48, 0.91]
	$Perf_{V20-PTV}$	0.66 [0.39, 0.88]
	$Perf_{TLung-PTV}$	0.58 [0.33, 0.82]

(p-value of 0.01). The other metrics did not exhibit significant differences between the two patient groups. A tendency of RP patients towards a relative increase or stability in Vent and Perf in the tumor and surrounding tissue over the treatment was found, while for non-RP patients a tendency towards decreasing Vent and Perf over the treatment course was observed.

The results of the univariate ROC-analysis after bootstrapping are presented in Table 2. Similar to the findings of the Mann–Whitney U test, good predictive power was obtained for the ventilation and perfusion parameters in the high-dose regions, namely $Vent_{PTV}$, $Perf_{PTV}$ and $Vent_{V20-PTV}$ with AUC values of 0.84, 0.73 and 0.71, respectively. While the $Perf_{V20-PTV}$ and the mean dose to the GTV also achieved high AUC values of 0.66 and 0.69, all other considered parameters only demonstrated low predictive performance. The ROC curves for the three best performing parameters are illustrated in Fig. 4.

Discussion

The main objective of the presented study was to discover potential MRI-based biomarkers for the prediction of RP in the context of MRgRT. Ventilation and perfusion parameters defined in the high-dose regions ($Vent_{PTV}$, $Perf_{PTV}$, $Vent_{V20-PTV}$) demonstrated promising results in stratifying patients at risk of developing RP $\geq$ 1. With bootstrapping [41], the internal validation strategy of choice for the development of medical prediction models with small sample sizes as suggested by Steyerberg et al. [42,43], a first internal validation of the prediction parameters could be provided, with median AUC values ranging from 0.71 to 0.84. These provided better results than clinical metrics typically associated with RP such as MLD and V20.

One major advantage of the MRI-based biomarkers used in this study over previously published approaches is the acquisition of functional information. Since our approach allows the acquisition of ventilation and perfusion maps using the same device as for treatment, the patient burden is minimized and repeated imaging is made easy. As changes

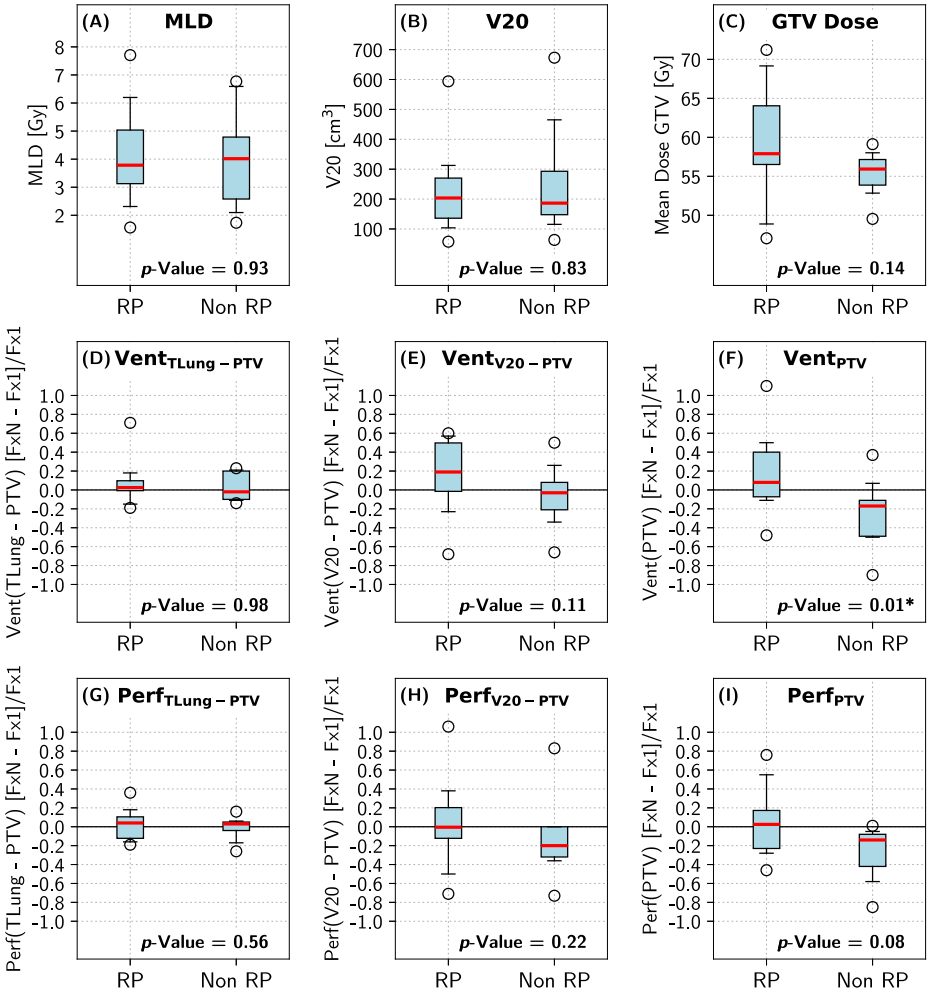

Fig. 3. The boxplots for all considered nine parameters. The comparison between the distributions of the RP and the non-RP patient cohort are illustrated for the three dosimetric parameters (subplots A-C), the Vent-based parameters (D-F) and the Perf-based parameters (G-I). The *p*-values for each parameter were determined using the non-parametric Mann–Whitney U test. All *p*-values below $\alpha = 0.05$ are indicated with '*'. The whiskers specify the 5th and 95th percentiles, the median values of the distributions are denoted as solid red line and outliers as circles.

between the start and end of treatment are to be expected and the Vent- and Perf-maps are qualitative, relative changes between Fx1 and FxN were investigated. This is a reasonable choice, allowing us to maximize signal variation in the maps by ensuring that sufficient time has elapsed. Preliminary analysis of the relative changes between Fx1 and the mid-treatment showed no predictive power, however, further investigations into whether earlier time points are correlated to the outcome are worth consideration in the future for a larger patient cohort. Since the lung density changes linked to RP observed in CT-scans are usually confined to the vicinity of the target, we hypothesized that regions exposed to high doses might lead to predictive biomarkers. Our results indicate that patients developing RP experience increasing ventilation and perfusion in the high-dose regions over the treatment course. Similar observations were made for a small number of patients in Siva et al. [35]. Since RP presents itself as a change in lung density and the NuFD ventilation depicts relative density changes in the lung parenchyma, the correlation between ventilation and RP is plausible. Similar performance for ventilation-based parameters was found in previous publications by Faught et al. [28], O'Reilly et al. [44] and Flakus et al. [17] demonstrating the potential of 4DCT-based ventilation and its superiority compared to clinical parameters with *p*-values below 0.05 for V20 and MLD in highly ventilated lung regions. Studies investigating the perfusion-based parameters extracted from SPECT/CT or PET/CT scans achieved similar AUC values of 0.75–0.87 [26,31,34] and p-values < 0.05. Exact comparisons with these studies, however, are challenging due to differences in the acquisition of the functional information and parameter definition. Furthermore, the different patient cohorts (SBRT vs conventional RT or chemoradiotherapy) and the RP/non-RP distribution was in most cases not comparable. This is also reflected in the mixed findings in literature for the performance of the MLD and the V20. Results ranged from p-values > 0.05 and AUC values ≤ 0.58 to significant p-values and AUC values ≥ 0.94 for the prediction

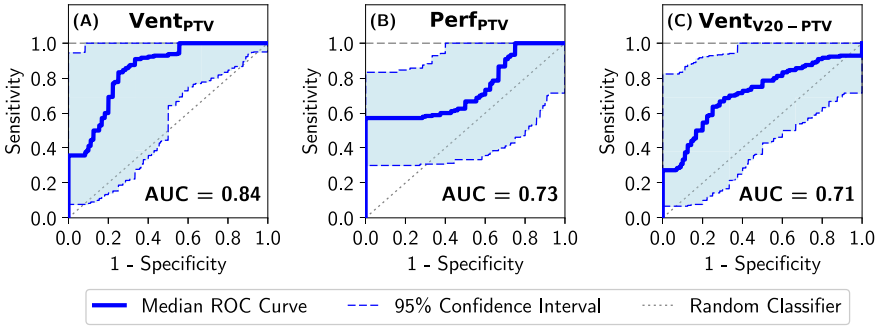

Fig. 4. The ROC curves for the functional parameters with highest AUC values. The median ROC curves after 5000 bootstrapping samples are presented as solid blue lines for the functional parameters with the highest median AUC values, namely Vent in PTV (A), Perf in PTV (B) and Vent in V20-PTV (C). The 95% confidence interval is shown as shaded area and its boundaries are highlighted with dashed blue lines. The dotted black line represents the performance of a random classifier.

of grade ≥ 2 RP [28,34]. In a study by Lucia et al. [26], comparable to our study with patients receiving hypofractionated SBRT, non-significant *p*-values and AUC values of 0.62 and 0.64 were obtained for MLD and V20 in EQD2 doses, respectively, for acute grade ≥ 2 RP prediction.

Using the biomarkers identified in this preliminary study, the early stratification of patients into RP risk groups at the end of treatment could aid patient follow up. As suggested by Arroyo-Hernández et al. [15], especially RP grade 1 should be closely monitored. For this, studies by Torre-Bouscoulet et al. [45] and Mattson et al. [46] proposed that longitudinal evaluation of pulmonary function tests performed at regular intervals starting six weeks after the treatment for patients at risk could help to early identify RP development. This might be further supported by encouraging the patients at risk to use a dedicated mobile application (app) to regularly record their health condition and any potential symptoms over the weeks after the end of radiotherapy [47–49], which has been shown to be beneficial in the early identification of RP and initiation of treatment [50]. Alternatively, Kohno et al. [51] and Iwata et al. [52] proposed monitoring of KL-9, a circulating antigen measurable in the blood and sensitive to interstitial pneumonia, to aid patient management after radiotherapy.

Even though this study is limited by the small patient cohort, which resulted in large confidence intervals for the ROC curves and AUC values, the potential of the presented approach was demonstrated and warrants further investigation in larger cohorts, prospective and multicenter studies following the proposed roadmap for the integration of imaging biomarkers in clinical trials [37]. By taking the patient distributions of the biomarkers found in this preliminary study into account, statistical considerations regarding the required patient numbers necessary to achieve statistical power in future studies can be made. This trial would provide necessary external validation and would also allow to investigate the potential of combinations of several parameters in a multivariate analysis, which could combine the functional parameters we identified, and could lead to an even better prediction model.

Conclusions

In the presented study, the potential of MRI-based ventilation and perfusion biomarkers extracted from non-contrast enhanced cine MRI-scans using the NuFD approach to predict acute radiation-induced changes in the lung parenchyma in MRgRT was investigated. Acquisition of an additional coronal image series at the tumor position using a 2D-bSSFP sequence in free-breathing and without additional equipment directly after the first and last treatment Fx, allowed the definition of function-based parameters in three different lung regions. Univariate analysis revealed encouraging results especially for the $Vent_{PTV}$, $Perf_{PTV}$ and $Vent_{V20-PTV}$ with AUC ≥ 0.71 and a *p*-value < 0.05 for the first parameter.

CRediT authorship contribution statement

Rabea Klaar: Writing – original draft, Visualization, Software, Investigation, Formal analysis, Data curation. **Moritz Rabe:** Writing – review & editing, Supervision, Investigation, Data curation, Conceptualization. **Anna Theresa Stüber:** Writing – review & editing, Methodology. **Svenja Hering:** Investigation, Data curation. **Stefanie Corradini:** Resources, Project administration. **Chukwuka Eze:** Supervision, Resources, Project administration. **Sebastian Marschner:** Resources, Project administration. **Claus Belka:** Resources, Project administration. **Guillaume Landry:** Writing – review & editing, Supervision, Methodology, Conceptualization. **Julien Dinkel:** Writing – review & editing, Supervision, Methodology, Funding acquisition, Data curation, Conceptualization. **Christopher Kurz:** Writing – review & editing, Supervision, Methodology, Data curation, Conceptualization.

Declaration of competing interest

The Department of Radiation Oncology of the LMU University Hospital, Munich has research agreements with Elekta, Brainlab and C-RAD.

Acknowledgments

RK and JD acknowledge partial funding by the German Center for Lung Research (DZL), but received no specific grant for this research. Dominika Dinkel, Christina Walchhofer and Patrick Thum are thanked for their help with the patient data acquisition and realization of the study.

Supplementary data

Sequence parameters

The sequence parameters for the three utilized baseline/setup MRI-scans that are part of the standard MRgRT workflow are listed. The used sequence was selected depending on the patient.

Exemplary functional regions

The regions used for the definition of the predictive functional parameters are depicted. Subfigure (A) shows the distribution of the dose of 20 Gy and higher, restricted to the lung. The 20 Gy isodose line is indicated in pink. The planning target volume (PTV) is displayed in (B) and the difference between the structures in (A) and (B) is displayed in (C). An additional margin of one pixel (3.91 mm) was added to the PTV before the subtraction. The whole tumor bearing lung without the PTV is illustrated in (D).

Exemplary patient scans

Baseline MRI- and follow-up CT-scans for four patients are shown. In subfigure (A) two patients' baseline MRI-scans and follow-up CT-scans in axial and coronal orientation are depicted. Both patients show no typical radiological signs of radiation-induced pneumonitis and were assessed with RP grade 0. Baseline and follow-up scans for two patients presenting with clear radiation-induced changes in the tumor surrounding lung parenchyma (indicated by red arrows), but without clinical symptoms (RP grade 1) are given in subfigure (B). The planning target volume (PTV) is depicted in blue in all baseline MRI-scans.

Supplementary material related to this article can be found online at https://doi.org/10.1016/j.radonc.2024.110468.

References

[1] Postmus PE, Kerr KM, Oudkerk M, Senan S, Waller DA, Vansteenkiste J, et al. Early and locally advanced non-small-cell lung cancer (NSCLC): ESMO Clinical Practice Guidelines for diagnosis, treatment and follow-up. Ann Oncol 2017;28:iv1–21, ESMO updated clinical practice guidelines.

[2] Bonanno L, Attili I, Pavan A, Sepulcri M, Pasello G, Rea F, et al. Treatment strategies for locally advanced non-small cell lung cancer in elderly patients: Translating scientific evidence into clinical practice. Crit Rev Oncol Hematol 2021;163:103378.

[3] Kang HJ, Kwak YK, Kim M, Lee SJ. Application of real-time MRI-guided linear accelerator in stereotactic ablative body radiotherapy for non-small cell lung cancer: One step forward to precise targeting. J Cancer Res Clin Oncol 2022;148:3215–23.

[4] Grills IS, Yan D, Martinez AA, Vicini FA, Wong JW, Kestin LL. Potential for reduced toxicity and dose escalation in the treatment of inoperable non–small-cell lung cancer: A comparison of intensity-modulated radiation therapy (IMRT), 3D conformal radiation, and elective nodal irradiation. Int J Radiat Oncol Biol Phys 2003;57(3):875–90.

[5] Chapet O, Khodri M, Jalade P, N'guyen D, Flandin I, D'hombres A, et al. Potential benefits of using non coplanar field and intensity modulated radiation therapy to preserve the heart in irradiation of lung tumors in the middle and lower lobes. Radiother Oncol 2006;80(3):333–40.

[6] Heinzerling JH, Hampton CJ, Robinson M, Bright M, Moeller BJ, Ruiz J, et al. Use of surface-guided radiation therapy in combination with IGRT for setup and intrafraction motion monitoring during stereotactic body radiation therapy treatments of the lung and abdomen. J Appl Clin Med Phys 2020;21:48–55.

[7] Corradini S, Alongi F, Andratschke N, Belka C, Boldrini L, Cellini F, et al. MR-guidance in clinical reality: Current treatment challenges and future perspectives. Radiat Oncol 2019;14:1–12.

[8] Godley A, Zheng D, Rong Y. MR-linac is the best modality for lung SBRT. J App Clin Med Phys 2019;20:7–11.

[9] Nierer L, Eze C, da Silva Mendes V, Braun J, Thum P, von Bestenbostel R, et al. Dosimetric benefit of MR-guided online adaptive radiotherapy in different tumor entities: liver, lung, abdominal lymph nodes, pancreas and prostate. Radiat Oncol 2022;17:1–14.

[10] Eze C, Lombardo E, Nierer L, Xiong Y, Niyazi M, Belka C, et al. MR-guided radiotherapy in node-positive non-small cell lung cancer and severely limited pulmonary reserve: a report proposing a new clinical pathway for the management of high-risk patients. Radiat Oncol 2022;17:1–8.

[11] Crockett CB, Samson P, Chuter R, Dubec M, Faivre-Finn C, Green OL, et al. Initial clinical experience of MR-Guided Radiotherapy for Non-Small Cell Lung Cancer. Front Oncol 2021;11.

[12] Hering S, Nieto A, Marschner S, Hofmaier J, Schmidt-Hegemann N-S, da Silva Mendes V, et al. The role of online MR-guided multi-fraction stereotactic ablative radiotherapy in lung tumours. Clin Transl Radiat Oncol 2024;100736.

[13] Finazzi T, Haasbeek JA, Spoelstra FOB, Palacios MA, Admiraal MA, Bruynzeel AME, et al. Clinical Outcomes of Stereotactic MR-Guided Adaptive Radiation Therapy for High-Risk Lung Tumors. Int J Radiat Oncol Biol Phys 2020;107.

[14] Käsmann L, Dietrich A, Staab-Weijnitz CA, Manapov F, Behr J, Rimner A, et al. Radiation-induced lung toxicity - Cellular and molecular mechanisms of pathogenesis, management, and literature review. Radiat Oncol 2020;15:1–16.

[15] Arroyo-Hernández M, Maldonado F, Lozano-Ruiz F, Muñoz-Montaño W, Nuñez-Baez M, Arrieta O. Radiation-induced lung injury: Current evidence. BMC Pulm Med 2021;21:1–12.

[16] Vinogradskiy Y, Castillo R, Castillo E, Tucker SL, Liao Z, Guerrero T, et al. Use of 4-dimensional computed tomography-based ventilation imaging to correlate lung dose and function with clinical outcomes. Int J Radiat Oncol Biol Phys 2013;86:366–71.

[17] Flakus MJ, Kent SP, Wallat EM, Wuschner AE, Tennant E, Yadav P, et al. Metrics of dose to highly ventilated lung are predictive of radiation-induced pneumonitis in lung cancer patients. Radiother Oncol 2023;182.

[18] Vinogradskiy YY, Castillo R, Castillo E, Chandler A, Martel MK, Guerrero T. Use of weekly 4DCT-based ventilation maps to quantify changes in lung function for patients undergoing radiation therapy. Med Phys 2012;39:289–98.

[19] Meng X, Frey K, Matuszak M, Paul S, Ten Haken R, Yu J, et al. Changes in Functional Lung Regions During the Course of Radiation Therapy and Their Potential Impact on Lung Dosimetry for Non-Small Cell Lung Cancer. Int J Radiat Oncol Biol Phys 2014;89:145–51.

[20] Klaar R, Rabe M, Gaass T, Schneider MJ, Benlala I, Eze C, et al. Ventilation and perfusion MRI at a 0.35 T MR-linac: feasibility and reproducibility study. Radiat Oncol 2023;18:1–15.

[21] Farr KP, Møller DS, Khalil AA, Kramer S, Morsing A, Grau C. Loss of lung function after chemo-radiotherapy for NSCLC measured by perfusion SPECT/CT: Correlation with radiation dose and clinical morbidity. Acta Oncol 2015;54:1350–4.

[22] Scheenstra AEH, Rossi MMG, Belderbos JSA, Damen EMF, Lebesque JV, Sonke J-J. Local dose-effect relations for lung perfusion post stereotactic body radiotherapy. Radiother Oncol 2013;107:398–402.

[23] Seppenwoolde Y, Muller SH, Theuws JC, Baas P, Belderbos JS, Boersma LJ, et al. Radiation dose-effect relations and local recovery in perfusion for patients with non–small-cell lung cancer. Int J Radiat Oncol Biol Phys 2000;47(3):681–90.

[24] Gaudreault M, Bucknell N, Woon B, Kron T, Hofman MS, Siva S, et al. Dose-Response Relationship Between Radiation Therapy and Loss of Lung Perfusion Comparing Positron Emission Tomography and Dual-Energy Computed Tomography in Non-Small Cell Lung Cancer. Int J Radiat Oncol Biol Phys 2024;118(4):1135–43.

[25] Miften MM, Das SK, Su M, Marks LB. Incorporation of functional imaging data in the evaluation of dose distributions using the generalized concept of equivalent uniform dose. Phys Med Biol 2004;49:1711–21.

[26] Lucia F, Bourhis D, Pinot F, Hamya M, Goasduff G, Blanc-Béguin F, et al. Prediction of Acute Radiation-Induced Lung Toxicity After Stereotactic Body Radiation Therapy Using Dose-Volume Parameters From Functional Mapping on Gallium 68 Perfusion Positron Emission Tomography/Computed Tomography. Int J Radiat Oncol Biol Phys 2023.

[27] Yamamoto T, Kabus S, Bal M, Bzdusek K, Keall PJ, Wright C, et al. Changes in Regional Ventilation During Treatment and Dosimetric Advantages of CT Ventilation Image Guided Radiation Therapy for Locally Advanced Lung Cancer. Int J Radiat Oncol Biol Phys 2018;102:1366–73.

[28] Faught AM, Yamamoto T, Castillo R, Castillo E, Zhang J, Miften M, et al. Evaluating which dose-function metrics are most critical for functional-guided radiotherapy with CT ventilation imaging. Int J Radiat Oncol Biol Phys 2017;99:202–9.

[29] Vinogradskiy Y, Schubert L, Diot Q, Waxweiller T, Koo P, Castillo R, et al. Regional Lung Function Profiles of Stage I and III Lung Cancer Patients: An Evaluation for Functional Avoidance Radiation Therapy Radiation Oncology. Int J Radiat Oncol Biol Phys 2016;95:1273–80.

[30] Katsuta Y, Kadoya N, Kajikawa T, Mouri S, Kimura T, Takeda K, et al. Radiation pneumonitis prediction model with integrating multiple dose-function features on 4DCT ventilation images. Phys Med 2023;105:102505.

[31] Farr KP, Kallehauge JF, Møller DS, Khalil AA, Kramer S, Bluhme H, et al. Radiation induced lung damage inclusion of functional information from perfusion SPECT improves predictive value of dose-volume parameters in lung toxicity outcome after radiotherapy for non-small cell lung cancer: A prospective study. Radiother Oncol 2015;117:9–16.

[32] Dhami G, Zeng J, Vesselle HJ, Kinahan PE, Miyaoka RS, Patel SA, et al. Framework for radiation pneumonitis risk stratification based on anatomic and perfused lung dosimetry. Strahlenther Onkol 2017;193:410–8.

[33] Gayed IW, Chang J, Kim EE, Nuñez R, Chasen B, Liu HH, et al. Lung perfusion imaging can risk stratify lung cancer patients for the development of pulmonary complications after chemoradiation. J Thorac Oncol 2008;3:858–64.

[34] Lee HJ, Zeng J, Vesselle HJ, Patel SA, Rengan R, Bowen SR. Correlation of Functional Lung Heterogeneity and Dosimetry to Radiation Pneumonitis using Perfusion SPECT/CT and FDG PET/CT Imaging. Int J Radiat Oncol Biol Phys 2018;102:1255–64.

[35] Siva S, Hardcastle N, Kron T, Bressel M, Callahan J, Macmanus MP, et al. Ventilation/Perfusion Positron Emission Tomography–Based Assessment of Radiation Injury to Lung Radiation Oncology. Int J Radiat Oncol Biol Phys 2015;93:408–17.

[36] Bucknell NW, Hardcastle N, Bressel M, Hofman MS, Kron T, Ball D, et al. Functional lung imaging in radiation therapy for lung cancer: A systematic review and meta-analysis. Radiother Oncol 2018;129(2):196–208, Special Issue: Radiotherapy in Asia - Part 2.

[37] van Houdt PJ, Saeed H, Thorwarth D, Fuller CD, Hall WA, McDonald BA, et al. Integration of quantitative imaging biomarkers in clinical trials for MR-guided radiotherapy: Conceptual guidance for multicentre studies from the MR-Linac Consortium Imaging Biomarker Working Group. Eur J Cancer 2021;153:64–71.

[38] Lombardo E, Rabe M, Xiong Y, Nierer L, Cusumano D, Placidi L, et al. Offline and online LSTM networks for respiratory motion prediction in MR-guided radiotherapy. Phys Med Biol 2022;67.

[39] Sharp GC, Li R, Wolfgang J, Chen G, Peroni M, Spadea MF, et al. Plastimatch: An open source software suite for radiotherapy image processing. In: Proceedings of the XVI'th International Conference on the use of Computers in Radiotherapy (ICCR), Amsterdam, Netherlands. 2010.
[40] NCI. National Cancer Institute Common Terminology Criteria for Adverse Events (CTCAE), Version 5.0. 2017, https://ctep.cancer.gov/protocolDevelopment/electronic_applications/ctc.htm. [Accessed: 6 March 2024].
[41] Efron B. Bootstrap methods: Another Look at the Jackknife. Ann Statist 1979;7(1):1–26.
[42] Steyerberg EW, Harrell FE, Borsboom GJJM, Eijkemans R, Vergouwe Y, Dik J, et al. Internal validation of predictive models: Efficiency of some procedures for logistic regression analysis. J Clin Epidemiol 2001;54:774–81.
[43] Steyerberg EW, Harrell FE. Prediction models need appropriate internal, internal–external, and external validation. J Clin Epidemiol 2016;69:245–7.
[44] O'Reilly S, Jain V, Huang Q, Cheng C, Teo BKK, Yin L, et al. Dose to Highly Functional Ventilation Zones Improves Prediction of Radiation Pneumonitis for Proton and Photon Lung Cancer Radiation Therapy. Int J Radiat Oncol Biol Phys 2020;107:79–87.
[45] Torre-Bouscoulet L, Arroyo-Hernández M, Martínez-Briseño D, Muñoz-Montaño WR, Gochicoa-Rangel L, Bacon-Fonseca L, et al. Longitudinal Evaluation of Lung Function in Patients With Advanced Non-Small Cell Lung Cancer Treated With Concurrent Chemoradiation Therapy. Int J Radiat Oncol Biol Phys 2018;101(4):910–8.
[46] Mattson K, Holsti LR, Poppius H, Korhola O, Stenman S, Tammilehto L, et al. Radiation pneumonitis and fibrosis following split-course radiation therapy for lung cancer: A radiologic and physiologic study. Acta Oncol 1987;26(3):193–6.
[47] Ciani O, Cucciniello M, Petracca F, Apolone G, Merlini G, Novello S, et al. Lung Cancer App (LuCApp) study protocol: A randomised controlled trial to evaluate a mobile supportive care app for patients with metastatic lung cancer. BMJ Open 2019;9(2).
[48] Yang H, Chung SH, Yoo J, Park B, Kim MS, Lee J. Evaluation of a Smart After-Care Program for Patients with Lung Cancer: A Prospective, Single-Arm Pilot Study. J Chest Surg 2022;55.
[49] Hauth F, Bizu V, App R, Lautenbacher H, Tenev A, Bitzer M, et al. Electronic Patient-Reported Outcome Measures in Radiation Oncology: Initial Experience After Workflow Implementation. JMIR Mhealth Uhealth 2019;7(7):e12345.
[50] Rades D, Werner E, Glatzel E, Bohnet S, Schild S, Tvilsted S, et al. Early Identification of Pneumonitis in Patients Irradiated for Lung Cancer—Final Results of the PARALUC Trial. Cancers 2023;15:326.
[51] Kohno N, Hornada H, Fujioka S, Hiwada K, Yamakido M, Akiyama M. Circulating Antigen KL-6 and Lactate Dehydrogenase for Monitoring Irradiated Patients with Lung Cancer. Chest 1992;102(1):117–22.
[52] Iwata H, Shibamoto Y, Baba F, Sugie C, Ogino H, Murata R, et al. Correlation between the serum KL-6 level and the grade of radiation pneumonitis after stereotactic body radiotherapy for stage I lung cancer or small lung metastasis. Radiother Oncol 2011;101(2):267–70.

Acquisition Dimensions	3D	3D	3D
Sequence Type	bSSFP	bSSFP	bSSFP
Orientation	Transversal	Transversal	Transversal
FOV [mm^3]	$540 \times 465 \times 432$	$500 \times 445 \times 432$	$400 \times 400 \times 432$
Matrix Size	$360 \times 310 \times 144$	$334 \times 300 \times 144$	$266 \times 266 \times 144$
Spatial Resolution [mm^3]	$1.5 \times 1.5 \times 3.0$	$1.5 \times 1.5 \times 3.0$	$1.5 \times 1.5 \times 3.0$
TE [ms]	1.27	1.27	1.43
TR [ms]	3.00	3.00	3.33
Flip Angle [°]	60	60	60
Receiver Bandwidth [Hz/pixel]	604	599	537
Parallel Imaging Technique	GRAPPA	GRAPPA	GRAPPA
Acceleration Factor	2	2	2
Nr Reference Lines	24	30	30
Slice Oversampling [%]	44.4	44.4	44.4
Phase FOV [%]	86.1	89.8	100
Partial Fourier Factor	6/8	6/8	6/8

Additional File 1. Sequence Parameters. The sequence parameters for the three utilized baseline/setup MRI-scans that are part of the standard MRgRT workflow are listed. The used sequence was selected depending on the patient.

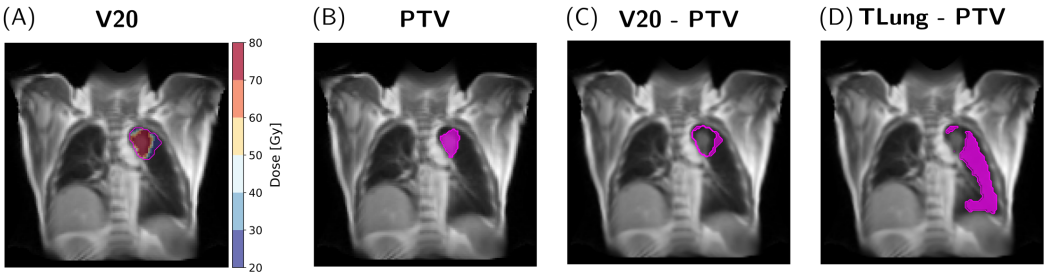

Additional File 2. Exemplary Functional Regions. The regions used for the definition of the predictive functional parame- ters are depicted. Subfigure (A) shows the distribution of the dose of 20 Gy and higher, restricted to the lung. The 20 Gy isodose line is indicated in pink. The planning target volume (PTV) is displayed in (B) and the difference between the structures in (A) and (B) is displayed in (C). An additional margin of one pixel (3.91 mm) was added to the PTV before the subtraction. The whole tumor bearing lung without the PTV is illustrated in (D).

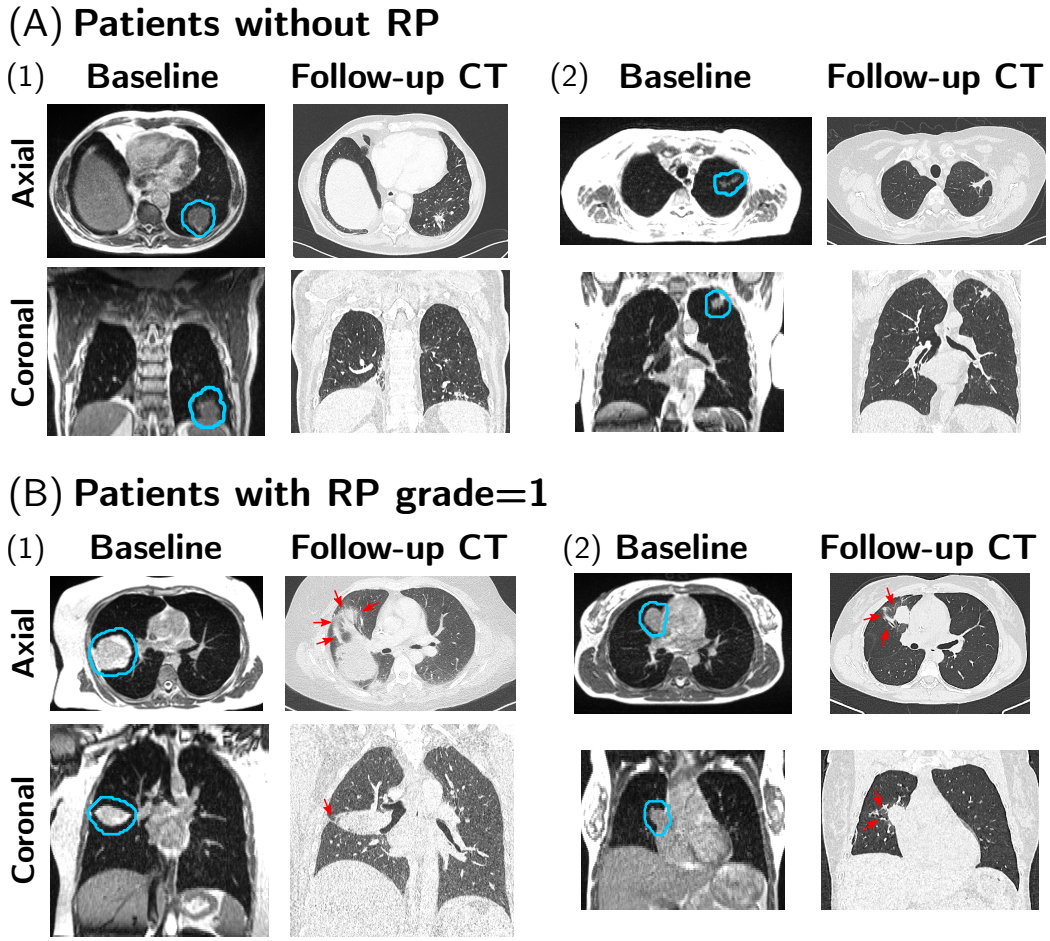

Additional File 3. Baseline MRI- and follow-up CT-scans for four patients are shown. In subfigure (A) two patients' baseline MRI-scans and follow-up CT-scans in axial and coronal orientation are depicted. Both patients show no typical radiological signs of radiation-induced pneumonitis and were assessed with RP grade 0. Baseline and follow-up scans for two patients presenting with clear radiation-induced changes in the tumor surrounding lung parenchyma (indicated by red arrows), but without clinical symptoms (RP grade 1) are given in subfigure (B). The planning target volume (PTV) is depicted in blue in all baseline MRI-scans.

5 Towards Automated Detection and Localization of Radiation-Induced Pneumonitis based on T_2-Maps

This chapter describes a sub-project of the TOSCA study, whose primary endpoint was presented in Publication II. The evaluation of this sub-study was performed in the scope of this dissertation. A manuscript is currently under preparation, but was not ready to be submitted at the time of the submission of this thesis. This chapter starts with a motivation for the use of T_2-mapping in the context of RT in Section 5.1. A summary of the patient cohort, the processing pipeline and statistical analysis tools is given in Section 5.2. The results of this study, divided into patient stratification and T_2-based RP segmentation, are presented in Section 5.3, followed by a Discussion in Section 5.4 and the Conclusions in Section 5.5.

5.1 Motivation

For the treatment of lung lesions originating from NSCLC or as metastasis from other cancer types, SBRT (Section 2.4.5) has been established as standard-of-care for the curative or palliative treatment of many cancer stages. Even though extensive advances with, e.g., MRgRT on MR-Linacs have been made in the context of high precision dose delivery and the corresponding reduction of target margins and thus a reduction of normal tissue subjected to high doses, RP is still a non-negligible side effect. As RP can result in severe long-term effects, regular check-ups and follow-up CT-scans are required to assess the onset of the condition and to monitor the development or the response to medication. Although CT-imaging is still considered as the gold-standard for the assessment of lungs in general and in particular also for post-RT evaluation, a valuable alternative could be MR-imaging. Apart from being radiation-free, MRI T_2-weighted imaging as well as T_2-mapping have been shown to be able to characterize different lung diseases [23, 25, 114, 147] and has been found in

early (pre-)clinical studies to be sensitive to RP and RILF in rats and humans [148, 149]. The purpose of this study was to investigate for the first time the potential of post-RT T_2-mapping acquired around 2-3 months after the end of RT on a diagnostic 1.5 T MRI-scanner for the automated stratification of patients with and without RP as well as for an automated, initial segmentation of the RP-affected lung volume (T_2-based RP mask) to assess the extent of the radiation-induced injury, which could trigger further imaging or intervention.

5.2 Materials and Methods

5.2.1 Patient Cohort

In this prospective study, a total of 22 lung tumor patients received hypofractionated MRgRT SBRT at a ViewRay MRIdian MR-Linac located at the Department of Radiation Oncology of the LMU University Hospital Munich (see Table 5.1). Study inclusion criteria were RT delivery in at least three fractions and no infracarinal lesions. As this study was a secondary endpoint of the study presented in Publication II, the patient cohorts are almost similar except from three patients. Two patients that were part of the primary study had to be excluded for the secondary analysis as the patients did not undergo the diagnostic follow-up MRI. One patient that could not be included in the primary analysis due to a problematic tumor position for the 2D imaging, but received the follow-up MRI and was considered for the secondary analysis. The fractionation schemes ranged from 3-10 fractions with 4-15 Gy/fraction. A detailed description of the utilized fractionation schemes is given in Table 5.1.

5.2.2 RP Grading

As described in Section 2.6.1, a follow-up CT-scan (FuCT) along with clinical presentation of the patient are required for RP assessment. All included patients underwent a FuCT at a median time between end of RT and FuCT of eleven weeks. The FuCT scans of each patient was judged by a radiologist regarding radiological changes suspicious of RP such as ground-glass opacities, new areas of consolidation, and reticulation in the vicinity of the tumor site, which served along with the patient's general condition, assessed during regular follow-up visits, as basis for the RP grading. The grading scheme used for this study was the National Cancer Institute Common Terminology Criteria for Adverse Events (NCI-CTCAE) version 5.0 [150]. Additionally, the RP-affected lung area was segmented (RP mask) by the radiologist, which served as ground-truth for the RP segmentation task. A total of 14 patients (64%) showed radiological indications for RP. Four patients (18%) of these patients additionally presented with symptoms and were therefore classified with RP grade 2, while the other ten patients (45%) showed no symptoms and were classified with RP grade 1. The remaining eight patients (36%) had no indication and were considered as RP grade = 0.

TABLE 5.1: **Patient Characteristics.** Patient Characteristics for the 22 patients with 23 lesions. All numbers listed in this table are reported in units of patient numbers if not indicated otherwise. The fractionation is given as physical dose.

Age [yrs]	Median	63
	Range	38-81
Sex	Male	10
	Female	12
Fractionation	3×13.5 Gy	6 (27%)
	3×15.0 Gy	4 (18%)
	5×8.0 Gy	1 (5%)
	5×10.0 Gy	1 (5%)
	8×7.5 Gy	2 (9%)
	10×4.0 Gy	1 (5%)
	10×5.0 Gy	7 (32%)
Type of Cancer	Primary Lesion	6 (26%)
	Metastasis	17 (74%)
NSCLC Stage	IA-B	3
	IIA	1
	IVA-B	2
Tumor Location	Superior Lobe Left	11 (48%)
	Superior Lobe Right	4 (17%)
	Inferior Lobe Left	4 (17%)
	Inferior Lobe Right	4 (17%)
RP Grade	Grade 0	8 (36%)
	Grade 1	10 (45%)
	Grade 2	4 (18%)

5.2.3 MR Image acquisition and processing

Treatment Planning Stage

The essential element of the standard MRgRT treatment planning workflow is, as explained in Section 2.5.3, the 3D image acquisition using a bSSFP sequence (RT baseline scan) on which the target and OARs are delineated and the dose plan is defined. The 3D lung volume was acquired in inspiration breath-hold and transversal orientation using the following sequence parameters: TE = 1.27 ms, TR = 3.00 ms, flip angle = 60°, receiver bandwidth = 604 Hz/pixel, spatial resolution = $1.5 \times 1.5 \times 3.0\,\text{mm}^3$. Depending on the patient's constitution, one of three different FOVs was selected: $540 \times 465 \times 432\,\text{mm}^3$, $500 \times 445 \times 432\,\text{mm}^3$ or $400 \times 400 \times 432\,\text{mm}^3$ along with the respective matrix sizes: $360 \times 310 \times 144$, $334 \times 300 \times 144$ or $266 \times 266 \times 144$.

For all patients, the PTV was defined as GTV plus an isotropic 5 mm margin.

Follow-up Stage

In addition to the standard-of-care FuCT required for the assessment of RP, comorbidities and tumor recurrence, the patients included in this study received an additional diagnostic follow-up MRI-scan at a 1.5 T MRI-scanner (MAGNETOM Aera/SolaFit, Siemens Healthineers, Erlangen, Germany) located at the Department of Radiology of the LMU University Hospital Munich. The median time between FuCT and follow-up MRI-scan was 22 days. An echo-planar single-shot fast spin echo sequence with phase conjugate symmetry (Siemens HASTE sequence, Section 2.2.5) utilizing electrocardiogramme (ECG) triggering was used to acquire T_2-weighted images of the full lung volume in inspiration breath-hold (two breath-holds per TE) and coronal orientation. The following parameters were utilized: TR = 314 ms, flip angle = 145°, receiver bandwidth = 780-781 Hz/pixel, FOV = 400 × 400 mm^2, slice thickness = 8.8 mm. An acquisition matrix of 128 × 128 and an interpolated matrix of 256 × 256 results in an interpolated in-plane resolution of 1.56 × 1.56 mm^2. The acquisition was repeated for five different TEs = [18, 36, 61, 100, 131] ms. For each patient, the different T_2-weighted images were slice-wise registered to the reference T2-weighted image acquired at TE = 18 ms using ANTs [136] for a multi-stage registration approach (rigid, affine and DIR) with mutual information as optimization metric and three-level multi-resolution (25%, 50%, 100%). The voxel-wise logarithm of the signal over the registered T_2-weighted images were then linearly fitted, as described in Section 2.3.2, to generate T_2-maps.

Image Processing

As different fractionation schemes were used, the dose distribution of each patient was converted to EQD2 according to Equation 2.55 using $\alpha/\beta = 3$ Gy [111] for lung tissue. In order to be able to link the target volume and the dose distribution with the T_2-maps for each patient, the RT baseline scan was deformably registered to the T_2-weighted reference image (TE = 18 ms) using Plastimatch [151]. For the registration, two stages, i.e., rigid and DIR using b-splines, were used with mutual information as optimization metric along with four (12.5%, 25%, 50%, 100%) and two (12.5%, 25%) resolution levels for rigid and DIR, respectively. The respective deformation fields were then used to propagate all defined RT treatment planning contours to T_2-map space. As T_2-maps were only acquired at the follow-up stage and not at the baseline stage, baseline-corrected T_2-maps were calculated per patient. For this, the T_2-maps were firstly masked by the propagated RT baseline lung segmentation and then equally divided into six sub-volumes (three per lung) in cranio-caudal direction. For each patient, a lung subvolume with the greatest possible distance from the target was selected and the mean T_2-value within the (healthy) subvolume $\overline{T}_{2,\text{healthy}}(\text{GTV})$ was calculated over coronal slices in which the GTV was defined. The baseline-

corrected T_2-maps were then calculated by:

$$T_{2,\text{baseline}-\text{corr}} = T_2 - \overline{T}_{2,\text{healthy}}(\text{GTV}). \tag{5.1}$$

Using the baseline-corrected T_2-maps, parameters were defined for the RP stratification task based on the mean T_2-value in two regions: the PTV and the V20 volume without the GTV, namely $\overline{T}_{2,\text{baseline}-\text{corr}}(\text{PTV})$ and $\overline{T}_{2,\text{baseline}-\text{corr}}(\text{V20} - \text{GTV})$.
In order to compare the T_2-based RP mask with the ground-truth RP mask segmented on the FuCT by an radiologist, the FuCTs were deformably registered using Plastimatch to the T_2-weighted reference image and the RP mask propagated to the T_2-map space based on the respective deformation fields, similarly to the baseline MRI to T_2-space registration.

5.2.4 Statistical Analysis and Metrics

The endpoint of the patient stratification task was to differentiate between patients with RP grade ≥ 1 (RP patients) and patients with RP grade $= 0$ (non-RP patients) based on the two T_2-based parameters. To assess the performance of the stratification, a univariate analysis based on systematical thresholding of the mean baseline-corrected T_2-values was performed using ROC curves and the respective AUC (Section 2.8.2) for quantification. In order to provide a first internal validation, bootstrapping (Section 2.8.3) with 5000 samples and the median ROC curves and respective AUC values along with the 95% confidence intervals (CIs) were determined. The non-parametric Mann-Whitney U test with a significance level of $\alpha_{\text{Stats}} = 0.05$ was used to probe for significant differences between the RP and non-RP parameter distributions.
For the segmentation task, first, the baseline-corrected T_2-maps were masked with the propagated RT baseline lung mask as well as the V20 mask to restrict the region-of-interest and to avoid the requirement of exact prior knowledge of (baseline-corrected) T_2-values of bones, blood vessels and other organs as well as other comorbidities that might resemble the radiological appearance of RP. As four patients out of the 14 RP patients received their follow-up MRI and FuCT more than four weeks apart and the voxel-based comparability of the RP regions' appearance could not be guaranteed, these patients were excluded from the segmentation task. To find the T_2-based RP mask, the baseline-corrected T_2 values in the lung-V20 volume were further thresholded. The cut-off used to differentiate between baseline-corrected T_2 values associated with RP or healthy lung parenchyma was determined by calculating the maximal Youden index (Equation 2.73) for the median ROC curve of the $\overline{T}_{2,\text{baseline}-\text{corr}}(\text{PTV})$ after bootstrapping and finding the corresponding baseline-corrected T_2 value cut-off. Using dilation with 6×6 kernel, followed by a 3×3 kernel and erosion with a 6×6 kernel, the thresholded T_2-based RP mask was smoothed for better visualization. Apart from visual comparison of the T_2-based RP mask to the ground-truth RP mask that was propagated to T_2-map space, the DSC, sensitivity, precision, the Seg AUC and the HD95 were calculated.

5.3 Results

5.3.1 Patient Stratification

The distributions of the mean baseline-corrected T_2 values in the PTV and the V20-GTV region were investigated for RP and non-RP patients and the respective boxplots are shown in Figure 5.1. While significant differences between the patient groups were found for both parameters with $p = 0.003$ for the PTV region and $p = 0.02$ for the V20 without GTV region, a visually clearer separation between the distributions was achieved by the mean baseline-corrected T_2 value in the PTV region. This finding is also reflected in the larger difference in the median of the mean baseline-corrected T_2 values between RP and non-RP patients with median values of 14 ms vs 1.6 ms for the RP and non-RP patients, respectively, in the PTV region and 5 ms vs -2.8 ms for the V20 without GTV region. These results clearly show that an increase in baseline-corrected T_2 values corresponds to RP.

The median ROC curves and the respective AUC values retrieved from the uni-

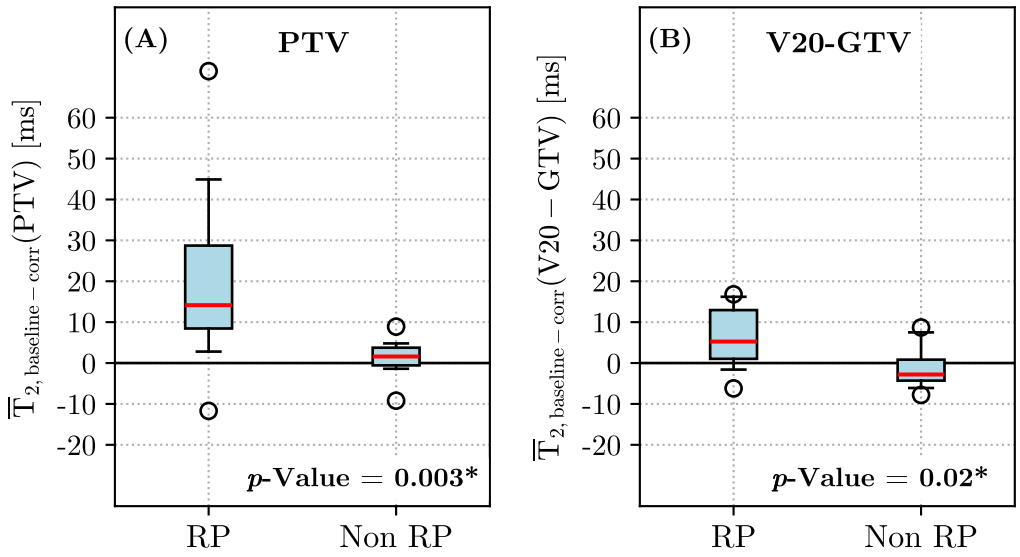

FIGURE 5.1: **Boxplots for the two considered patient stratification parameters.** The RP and non-RP distributions of the mean baseline-corrected T_2 values in the PTV (subplot (A)) and the V20-GTV region (subplots (B)) are illustrated. The boxplot whiskers indicate the 5th and 95th percentiles. The median value of each distribution is visualized with the red lines and outliers as circles. The non-parametric Mann-Whitney U test was used to calculate the p-values, where significance at $\alpha_{\mathrm{Stats}} = 0.05$ is specified with the asterix '*'.

variate analysis after bootstrapping are presented in Figure 5.2. The results of the quantitative stratification model evaluation are in agreement with the findings from the non-parametric Mann-Whitney U test. Both parameters achieve good stratifi-

cation performance regarding sensitivity and specificity and thus high AUC values of 0.88 and 0.80 for the PTV and the V20 without GTV region, respectively. The maximal Youden index of the median ROC curves was found to be 0.80 with the corresponding cut-off of 8 ms for the PTV region and 0.65 with a cut-off of -1 ms for the V20 without GTV region.

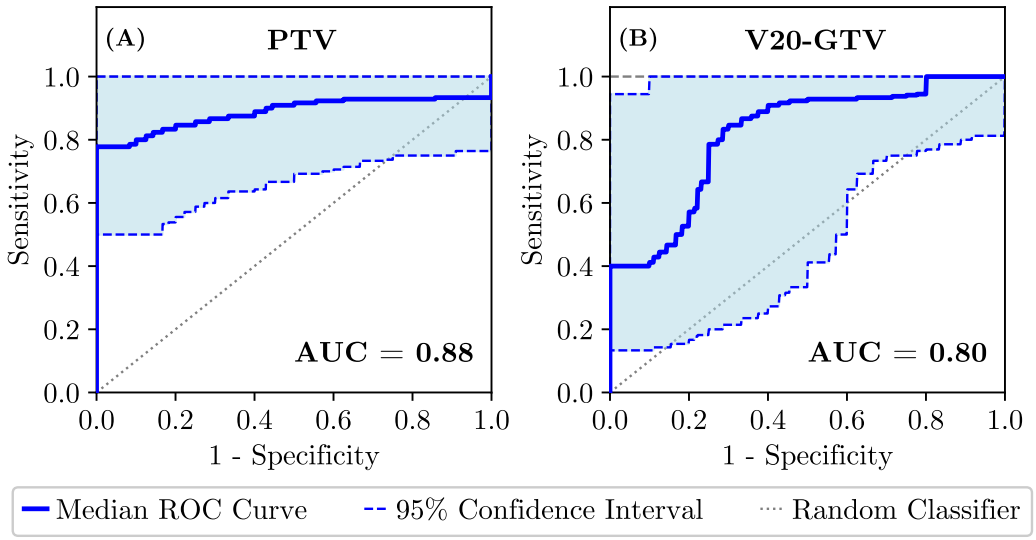

FIGURE 5.2: **Median ROC curves for the two investigated patient stratification parameters.** The solid blue lines illustrate the median ROC curves after 5000 bootstrapping samples for the mean baseline-corrected T_2 values in the PTV (Subplot (A)) and in the V20 without GTV region (Subplot (B)). The respective AUC values represent the median AUC values. The shaded area in light-blue bounded by blue dotted lines indicates the 95% confidence interval and the dotted black line represents the performance of a random classifier.

5.3.2 T_2-based RP Segmentation

The performance of the baseline-corrected T_2-based RP segmentation was assessed visually as well as quantitatively. Starting with the visual comparison of the T_2-based RP mask with the ground-truth RP mask, four exemplary patients are presented in Figure 5.3 with varying initial tumor size and RP extent. A good visual agreement was found for patients with medium to large RP extent (Subfigure (A), (B), (D)), apart from slight overestimation for Patient 2 in Subfigure (B). In patients with minor extent of radiation-induced tissue changes, the T_2-based RP mask clearly overestimates the affected area (Subfigure (C)).

Looking at the quantitative values retrieved from different metrics, shown in Table 5.2, especially the DSC and the HD95 demonstrate only moderate agreement with the ground-truth with median values over all patients of 0.32 and 18.8 mm, respectively.

Similarly, the median sensitivity and precision calculated over all patients indicate merely limited performance with 0.48 and 0.42, respectively. On the contrary, with 0.74, an overall high median Seg AUC was found. Taking a closer look at specific patients reveals that in particular Patient 2 and Patient 6 achieved above average DSC, precision and Seg AUCs with 0.58, 0.62 and 0.77 (Patient 2) and 0.64, 0.74, and 0.78 (Patient 6), respectively, which agrees with the visual impression (Figure 5.3 (B) and (D)). Due to the overestimation of the RP region by the T_2-based RP mask, as already seen in Figure 5.3 (C), Patient 3 achieved the worst DSC and precision values with 0.04 and 0.02, respectively.

TABLE 5.2: **Quantitative segmentation comparison.** In order to provide a quantitative comparison between the T_2-based RP mask and the RP mask segmented by a radiologist propagated to T_2-map space (ground truth), the DSC, sensitivity, precision, segmentation area under the curve (Seg AUC) value and the 95% Hausdorff distance (HD95) were calculated for the ten RP patients.

	Dice	Sensitivity	Precision	Seg AUC	HD95 [mm]
Patient 1	0.40	0.48	0.34	0.74	18.6
Patient 2	0.58	0.54	0.62	0.77	23.6
Patient 3	0.04	0.75	0.02	0.87	33.8
Patient 4	0.34	0.47	0.26	0.73	18.9
Patient 5	0.50	0.43	0.58	0.72	17.2
Patient 6	0.64	0.57	0.74	0.78	14.2
Patient 7	0.23	0.63	0.15	0.81	16.8
Patient 8	0.09	0.19	0.06	0.60	20.7
Patient 9	0.09	0.05	0.49	0.52	54.9
Patient 10	0.29	0.20	0.50	0.60	15.8
Median	0.32	0.48	0.42	0.74	18.8

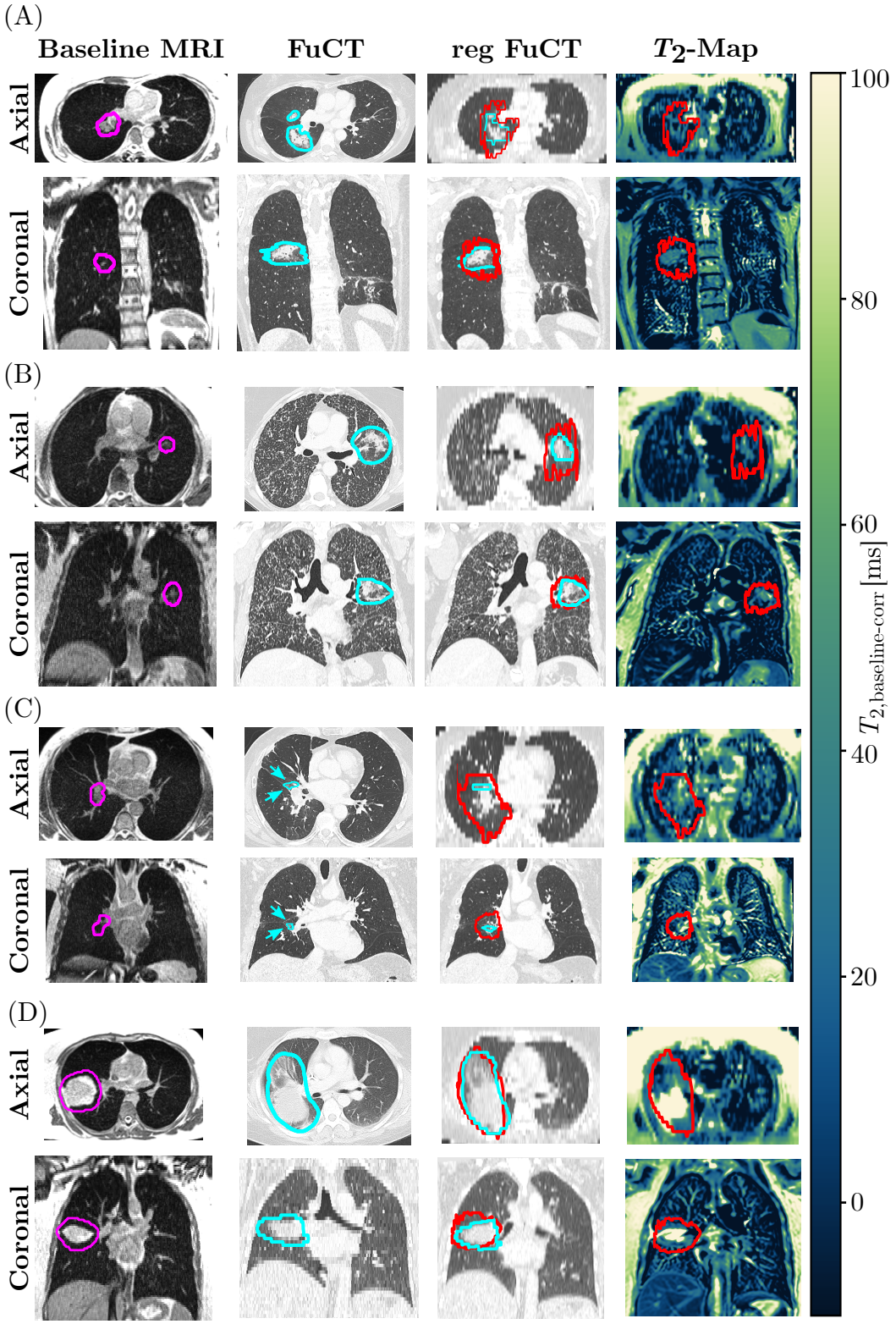

FIGURE 5.3: **RP segmentation comparison.** The baseline MRI-scan with the PTV in pink, the FuCT scan with the RP mask segmented by a radiologist in light-blue, the FuCT scan registered to the T_2-map space with the propagated ground-truth RP mask in light-blue and the T_2-based RP mask in red as well as the baseline-corrected T_2-map with T_2-based RP map in red are shown for Patient 1 (Subfigure (A)), Patient 2 (B), Patient 3 (C) and Patient 6 (D).

5.4 Discussion

The main goal of this study was to investigate the potential of post-RT T_2-mapping to aid the identification of RP patients and to provide a first visualization of the extent of the affected lung volume. Mean T_2 values calculated in the PTV and the V20-GTV region ($\overline{T}_{2,\text{baseline}-\text{corr}}(\text{PTV})$ and $\overline{T}_{2,\text{baseline}-\text{corr}}(\text{V20}-\text{GTV})$) after baseline-correction, done by subtracting the mean T_2 value in a healthy part of the lung with maximal distance from the lesion, demonstrated significant differences between non-RP patients and patients with RP grade ≥ 1. Using bootstrapping as internal validation strategy to assess the T_2-based parameter's ability to stratify patients, AUC values ≥ 0.80 were achieved. In addition to the patient stratification, the T_2-mapping was also investigated regarding its potential in providing a voxel-based initial segmentation of the by RP-affected lung volume. Even though the median DSC, sensitivity, precision and HD95 revealed only moderate conformity between the T_2-based RP mask and the ground-truth, that was segmented on the standard-of-care FuCT-scan by a radiologist and propagated to T_2-map space, an overall good visual agreement between the segmentations and the ground-truth was found especially for medium to large RP-affected lung volumes.

To the best of the author's knowledge, this study is the first that successfully proposed a pipeline for the use of T_2-mapping in lung cancer patients after RT and that does not require a CT-scan. The almost automated nature of the workflow and the lack of radiation dose or the administration of radionuclides during the acquisition of the different TE-images necessary to retrieve the T_2-maps indicate the potential to reduce the radiologist's workload and particularly the patient burden. This is a clear advantage over the studies, e.g., by Farr et al. [152] that suggested to use SPECT/CT before and three months after RT as the change in regional perfusion retrieved from both SPECT/CT-scans are correlated with the severity of RP-related symptoms and showed significant differences between RP and non-RP patients for a specific dose region. Most studies using post-RT SPECT/CT or PET/CT perfusion imaging, e.g., by Siva et al. [48], Scheenstra et al. [153] or Zhang et al. [154] only focused on a pure investigation/description of lung perfusion changes in different lung regions over time post-RT without differentiating between RP and non-RP patients. Similarly, these studies provide no spatial analysis to determine the extent of RP-affected lung areas. Apart from this, a possible comparison with a previous study by Mayo et al. [155] regarding the T_2 values found in healthy volunteers revealed good agreement with the values retrieved in healthy lung parts and used for the baseline-correction.

One limitation of the presented study is the only moderate quantitative performance of the T_2-based RP segmentation. One reason for this, which is also supported by the good visual agreement between ground-truth and T_2-based RP mask for example for Patient 1 (Table 5.2 and Figure 5.3 (A)), is the fact that quantitative metrics to assess segmentation results such as the DSC or the HD95 are not the ideal indicators for this specific application. Despite the use of dilation and erosion methods

to smooth the segmentation boundary retrieved from voxel-based thresholding, the resulting segmentation is still ragged. An overall lower agreement between this segmentation and the manually segmented ground-truth RP mask is therefore expected when using the DSC or the HD95 that focus on the exact overlap of the delineated shapes. This comparison is not only further complicated by uncertainties in the original ground-truth RP masks, as a mass-like RP appearance can be difficult to distinguish from local tumor recurrence [156], but also by the fact that it was segmented on the FuCT scan, which is typically acquired at a higher resolution than the T_2-maps. Even though great care was taken with the required deformable image registration being optimized on a patient-by-patient basis, the need to propagate the ground-truth to the T_2-space can introduce uncertainties.
Similarly, a deformable registration is necessary to align the different TE-images that were acquired over several breath-holds. Slightly mismatched voxels can affect the voxel-intensity curve over the TEs and in turn the linear fit and the resulting T_2 time for these specific voxels. Furthermore, the general approach to generate the T_2-based RP mask could be further optimized. Considering that the Youden index was developed to find the differentiating ability of a biomarker [157] and that the underlying ROC curves of the mean baseline-corrected T_2 values in the high dose region demonstrated good stratification power, utilizing the maximal index and its corresponding cut-off T_2-value to threshold the T_2-maps seemed to be a valid first approach. Despite the good performance of the method for medium to large RP regions, small RP regions, as for Patient 3 (Figure 5.3 (C)), are clearly overestimated suggesting that the thresholding approach might not be ideal in these cases. Therefore, further investigations are necessary to determine whether, e.g., a probability model-based approach might improve the results. Despite these limitations, it is worth to further investigate the use of T_2-mapping in particular and MR imaging in general for post-RT assessment.
Currently, the gold-standard for lung imaging are still CT-scans and they are typically also the standard-of-care follow-up technique post-lung-RT to assess the status of the radiated lung lesion and potential radiation-induced lung injuries. Even though the radiation dose exposure of patients treated with RT is quite high and the dose applied during CT-scans is comparably small, patients can still benefit from reducing the imaging-related radiation dose. Considering the repeated imaging the patients have to undergo, especially in the first five years after the end of RT, MRI-scans to identify and monitor RP could help to decrease the dose burden and decrease the probability of the introduction of secondary cancers. The proposed T_2-mapping approach, that requires no ionizing radiation or contrast agent, could provide, if acquired 2-3 months after the end of RT, a first stratification of patients with and without radiation-induced changes as well as a first estimation on the extent of the changes. One possibility could be that a positive result, i.e., the patient was identified to have RP, triggers additional CT- or PET/CT-imaging to further investigate the severity. Another option could be to leverage further MRI sequences that can be easily added to the follow-up MRI protocol without additional efforts.

To provide CT-like morphological information, Dournes et al. [158] proposed to use UTE sequences with 1 mm-isotropic resolution that were successfully demonstrated for the disease assessment of cystic fibrosis and ILD [159]. Furthermore, Bauman et al. [101] presented a self-gated free-breathing 3D bSSFP (bSTAR) sequence at sub-millimeter resolution as another alternative for CT-scanning for morphological imaging. In addition to adding MRI-based morphological imaging, the quantitative T_2-mapping should be further exploited to characterize different tissue types based on their quantitative T_2 values. Similarly to Buzan et al. [23, 24], who showed that different T_2 values are observed for different patterns in usual interstitial pneumonia and non-specific interstitial pneumonia as well as in active inflammatory and static fibrotic regions, post-RT T_2-mapping could be able to differentiate between RP, remaining and/or recurring tumor mass and healthy tissue. Due to the small patient cohort of ten patients, the quantitative assessment of different regions for tissue characterization was outside the scope of this work. This was additionally hindered by the lack of a baseline T_2-map in this study to identify pre-existing comorbidities. One possibility to overcome this could be by performing T_2-mapping already during the planning stage directly at the MR-Linac as this would require little additional costs and efforts. This could be especially advantageous to also monitor the treatment response as, e.g., proposed by Lutsik et al. [160] for glioblastoma patients using a multi-echo T_2 sequence. The imaging required for the T_2-mapping at the diagnostic 1.5 T MRI-scanner could be further optimized by also using a multi-echo T_2 sequence to potentially decrease the number of required breath-holds or to even implement T_2-mapping based on a free-breathing acquisition [161]. Furthermore, a decrease of the slice thickness and/or the in-plane resolution might increase the precision in segmenting small RP-affected lung volumes.
Even though this study provides a good first step in showing the potential of using post-RT T_2-mapping with significant differences between RP and non-RP in the high-dose region and good visual comparability between T_2-based RP segmentation and the ground-truth RP segmentation, investigations in larger patient cohorts and multicenter studies are necessary to further validate method.

5.5 Conclusions

In this study, an approach using 3D T_2-maps acquired at a diagnostic 1.5 T MRI-scanner with multiple HASTE sequences 2-3 months after the end of lung MRgRT to firstly stratify patients into RP and non-RP patient groups and to secondly provide a visualization of the localization and extent of the lung volume affected by RP without requiring a FuCT was proposed. The mean T_2 values retrieved in the PTV and the V20-GTV region demonstrated significant differences with p-values ≤ 0.02 between RP and non-RP patients and achieved AUC values ≥ 0.80 in a univariate analysis using bootstrapping. Based on the T_2 value cut-off that corresponded to the maximum Youden index of the ROC curve of $\overline{T}_{2,\mathrm{PTV}}$, a T_2-based RP volume segmentation was generated utilizing thresholding. Despite only moderate quantitative

agreement with the ground-truth, a segmentation of the RP volume based on the standard-of-care follow-up CT by a radiologist, with a median DSC of 0.32 as well as sensitivity and precision below 0.50, a good visual comparability was achieved.

6 | Conclusion and Outlook

The introduction of MR-Linacs into the clinical workflow to combine radiation treatment with MR imaging has opened up many opportunities to improve the treatment of cancer patients. The excellent soft-tissue contrast and the radiation dose-free imaging offered by MRI is already utilized for treatment planning and specifically for the delineation of targets and OARs, daily in-room MRI for treatment plan adaptation to the anatomy of the day, as well as real-time cine imaging for tumor tracking and gated beam delivery. This precise target localization and option to adapt to anatomical changes from fraction to fraction along with the ability to visualize the tumor in real-time has allowed to apply highly conformal treatment plans in the form of (hypofractionated) SBRT, which has been established as standard-of-care treatment for many non-operable lung lesions. Even though lung tumor patients already benefit from the described advantages, the integrated MRI offers even more imaging possibilities to gain information on a fraction-by-fraction basis over the treatment course without additional costs. This is of particular relevance for lung tumor patients as RP still commonly develops in the irradiated lung area weeks after the end of RT and no clear indicators have been identified that would enable to determine patients at risk of developing RP.

The focus of this thesis was on the prediction of RP in patients receiving lung MRgRT using non-contrast enhanced functional imaging and the MRI-based detection and assessment of RP. The first part was concerned with the ViewRay MRIdian MR-Linac system and the latter with a diagnostic MRI-scanner. Three research projects were carried out in the scope of this thesis to establish non-contrast enhanced functional lung imaging at the MR-Linac, to investigate its potential for the prediction of RP and to evaluate the possibility of automated MRI-based RP detection to stratify patients and to assess the extent of the affected lung volume.

The first project, Publication I, focused on transferring the, at diagnostic scanners already thoroughly investigated, NuFD method to the low-field MR-Linac and evaluating two normalization methods to compensate for differences in breathing amplitude and heart rate between repeated scans of healthy volunteers and thus strongly improving the reproducibility of the method, which is essential in longitudinal studies investigating functional changes. One of the normalization approaches, the ROI-based technique, was then used to normalize the functional maps in the

subsequent project.
Both normalization strategies developed in Publication I clearly improved the reproducibility of the functional maps in healthy volunteers, however, both demonstrate limitations regarding their applicability in longitudinal patient studies. The first strategy, based on the definition of a normalization factor derived from the correlation between ventilation signal and diaphragm position, provides a normalization of the ventilation signal by only using the diaphragm positions and ventilation signal amplitudes of the unregistered image series. On the one hand, this approach is advantageous, due to lack of potential uncertainties induced by the image registration, on the the other hand, its performance is strongly affected by breath-holds during the acquisition of the image series. As lung tumor patients at the MR-Linac undergo a gated treatment requiring repeated breath-holds, some patients unconsciously tend to hold their breath for short intervals during the free-breathing acquisition of the image series for the NuFD method. The second normalization strategy, based on the positioning of a ROI on a healthy part of the lung and calculating the mean ventilation or perfusion value to normalize the ventilation and perfusion maps, respectively, demonstrates a more robust approach against these breathing irregularities. Despite this robustness, the method showed performance differences depending on the ROI position and size. This might introduce uncertainties in lung tumor patients suffering from additional lung comorbidities in the lung region found to be ideal for ROI placement.
In the second project, Publication II, the NuFD method was integrated into a clinical study and ventilation and perfusion maps were acquired for lung tumor patients receiving MRgRT at the low-field MR-Linac of the LMU University Hospital. Functional parameters defined as the change in ventilation and perfusion between last and first treatment fraction in the high-dose region were found to be predictive of RP grade ≥ 1 thereby providing better prediction performance as commonly employed dosimetric parameters.
One general limitation of the current prediction model developed in Publication II is its predictive qualities regarding the occurrence of RP lather than 2-3 months post-RT. Since there is a non-negligible percentage of patients with a radiation-induced lung injury developing between the first three to six months, further investigations have to be carried out in a larger patient cohort to improve the identification of patients developing RP or RILT at a later stage. Furthermore, even though the functional parameters obtained from the change between last and first treatment Fx provide easily acquirable biomarkers predictive of RP, the gained functional information currently only allows to identify patients at risk directly after RT. As information from start and end of RT are required, an intervention or adaptation of the treatment plan derived from these parameters is not possible. First attempts in including mid-treatment information have been made in the scope of the study presented in Publication II, but showed no predictive power and was thus not able to replace the last fraction scan. However, further investigations in a larger patient cohort are necessary to probe the predictive potential of earlier time points. The

derivation of pre-treatment function-based constraints to inform the baseline dose planning to reduce the RP risk or biomarkers acquired during the treatment to trigger the dose plan adaptation based on the ventilation and perfusion maps retrieved from the NuFD method would be an important step towards RP avoidance treatment planning [121]. This is currently prevented by two main limitations. As the acquisition of the cine data is based on a bSSFP sequence and makes use of unsaturated spins that are pumped into the selected slice by the heartbeat to assess the perfusion information, the Fourier-based methods to assess both ventilation and perfusion are limited to a 2D slice acquisition. Even though the scan time would be noticeably increased, 3D information could be retrieved by multiple 2D acquisitions to cover the whole lung volume. The second limitation is that the method is only of qualitative nature, as it is patient-dependent and represents relative lung density changes and blood flow changes, which limits inter-patient comparison and the possibility of finding quantitative, RP-indicative values. Using the normalization approach developed in Publication I, enables only intra-patient comparison and the calculation of relative functional differences that can be compared between patients. However, despite showing promising results in retrospective studies, prospective, randomized clinical trials designed to compare (ventilation-based) functional lung avoidance RT with the standard-of-care RT, e.g., by Baschnagel et al. [162] or a prospective trial by Miller et al. [163] that compared to historical data, merely found minor differences between the two groups regarding RP development and decrease in lung function assessed by pulmonary function tests. This suggests that the current function-based approaches might not be ideal for the reduction of RP development, but can, as shown in Publication II, provide a fast and easy method to identify patients at risk early to allow a close monitoring with regular check-ups and dedicated medical interventions if necessary. Although most publications focus solely on the prediction or prevention of RP grade ≥ 2, this should be also true for patients with RP grade 1, as done in this thesis. While RP grade 1 is in most grading scales not considered clinically relevant and is assumed to not require medication, it should be closely monitored every three weeks as proposed by Maddali et al. [113] or even every 1-3 days as proposed by Yan et al. [164]. Furthermore, it has to be taken into account that in spite of the many available grading schemes, RP grading is currently still difficult, as both, symptoms and radiological image-based changes are considered. Not only does the clinical symptoms assessment suffer from inter-observer variations between different radiation oncologists [165], without a more objective measure, the patients' own judgment/impression on RP-related symptoms, e.g., occurrence of dyspnea or worsening of their general condition can be obscured by the patients being accustomed to living with symptoms or restrictions related to their cancer burden. As tissue changes on CT-scans are more easily quantifiable and less subjective, a grading scheme solely based on radiological findings was proposed by Kouloulias et al. [166]. On the other hand, grading on pure radiological appearance is considered by radiation oncologists as potentially misleading since tissue abnormalities in the radiated area appear regularly without an increase in symptoms and with a generally good

condition [165]. In this thesis, the focus was on identifying all patients with radiological appearances of radiation-induced changes on their CT-scans, which could trigger a combination of monitoring procedures for the patient management. Along with the proposed approaches of regular pulmonary function tests [167], taking of blood samples to monitor the circulating antigen KL-9 shown to be sensitive to interstitial pneumonia [168] and asking the patient to daily document their health condition in a dedicated mobile application (app) for a more precise symptom evaluation [169], regular imaging might aid the extent assessment of the affected lung area.
Since repeated CT-scans come with an increased radiation dose exposure, an MRI-based approach using T_2-mapping without the need for contrast agents was proposed in the third project of this thesis for the follow-up assessment of lung tumor patients post-RT. It was found to be sensitive to radiation-induced tissue changes and to allow a first localization and volume definition. In order to improve the differentiation between pre-existing comorbidities and radiation-induced tissue changes, a T_2-map could be acquired at baseline level (before RT). With this, the quantitative nature of the T_2-maps is fully leveraged without the need for the baseline-correction introduced in Chapter 5 to remove the influence of pre-existing tissue changes. Quantitative T_2 values could further allow to distinguish tumor recurrence from mass-like RILI patterns, which look similar in CT-scans and typically require the acquisition of a FDG-PET/CT [114]. As the patient cohort available for the project presented in Chapter 5 was limited to 14 patients, an extension of the cohort also in a multi-center setting could enable the characterization of different tissue types and RILI patterns based on T_2 values as demonstrated by Buzan et al. [23] for different interstitial lung disease patterns. Patients could benefit from a reduced exposure to imaging modalities employing ionizing radiation to decrease the risk of radiation-induced secondary cancers. Furthermore, MRI offers to combine different imaging approaches to cover anatomical, morphological, functional and quantitative imaging utilizing the different dedicated sequences in one scan protocol. Adding, e.g., a high-resolution UTE sequence to the follow-up MRI protocol could provide CT-like anatomical and morphological information as shown by Dournes et al. [158] for cystic fibrosis patients and is worth investigating in RP patients. Apart from the morphological imaging options, there are many more possibilities regarding advanced and/or quantitative imaging such as diffusion-weighted imaging [170] or inflammation-sensitive $T_{1\rho}$-mapping commonly used in heart imaging [171] that could eventually enable MRI to replace (PET/)CT for follow-up and monitoring of patients after lung RT.
Especially regarding imaging at the MR-Linac, the potential of simple, pre- or post-RT MR image acquisition on a fraction-by-fraction basis directly at the same device without patient repositioning or additional costs or equipment is not yet fully exploited. Implementing the T_2-mapping and other mapping (T_1, $T_{1\rho}$) or other imaging strategies such as DWI (Section 2.5.5) [35] and integrating it similar to the NuFD method in the clinical workflow could, even in combination with the NuFD-based functional maps, not only support the RP prediction, but could offer additional tumor response monitoring tools in the near-future. This also has the potential to aid

the currently used morphological images in the treatment planning and adaptation process in terms of tumor delineation.
Another active research area that could improve MRgRT in several aspects is artificial intelligence (AI). Besides having been successfully proposed for OAR segmentation [172] and target motion tracking and prediction [173], it has been shown to improve image reconstruction in undersampled data and in the presence of motion. This could allow a higher spatial image resolution for the fast 2D-cine bSSFP acquisition for the NuFD method, which could improve the accuracy of the RP prediction model. A highly accelerated 3D image acquisition (with higher spatial resolution) of the TE-images for the T_2-mapping could enable a transition from repeated breath-hold to free-breathing acquisitions in order to reduce the patient burden, while potentially improving the T_2-based RP segmentation. Furthermore, provided a large dataset from multicenter studies, AI or deep learning models could boost the RP prediction and stratification models presented in this thesis and might aid the T_2-based segmentation.

To conclude, in the scope of this thesis, the non-contrast enhanced functional lung imaging method NuFD along with two normalization strategies for repeated imaging were established at a clinical low-field MR-Linac. NuFD-based functional parameters were derived in a clinical patient study and shown to be predictive of RP and an approach based on post-RT T_2-maps was developed that could provide an automated RP-non-RP patient stratification and a first segmentation of the RP-affected lung volume. With these studies, advances have been made towards the clinical implementation of functional imaging during MRgRT for early identification of patients at risk of developing RP and first steps have been taken towards an MR-only follow-up procedure after lung RT that could improve patient care in the future.

7 | Bibliography

1. Bray, F. *et al.* Global cancer statistics 2022: GLOBOCAN estimates of incidence and mortality worldwide for 36 cancers in 185 countries. *CA: A Cancer Journal for Clinicians* **74,** 229–263 (2024).
2. Kratzer, T. B. *et al.* Lung cancer statistics, 2023. *Cancer* **130,** 1330–1348 (2024).
3. Siegel, R. L., Giaquinto, A. N. & Jemal, A. Cancer statistics, 2024. *CA: A Cancer Journal for Clinicians* **74,** 12–49 (2024).
4. Stella, G. M., Kolling, S., Benvenuti, S. & Bortolotto, C. Lung-Seeking Metastases. *Cancers* **11** (2019).
5. Vinod, S. K. & Hau, E. Radiotherapy treatment for lung cancer: Current status and future directions. *Respirology* **25,** 61–71 (2020).
6. Mayinger, M. *et al.* Stereotactic body radiotherapy for lung oligo-metastases: systematic review and international stereotactic radiosurgery society practice guidelines. *Lung Cancer,* 107284 (2023).
7. Martin, A. & Gaya, A. Stereotactic Body Radiotherapy: A Review. *Clinical Oncology* **22,** 157–172 (2010).
8. Angel, E. *et al.* Dose to radiosensitive organs during routine chest CT: effects of tube current modulation. *American Journal of Roentgenology* **193,** 1340–1345 (2009).
9. Keall, P. J. *et al.* Review of Real-Time 3-Dimensional Image Guided Radiation Therapy on Standard-Equipped Cancer Radiation Therapy Systems: Are We at the Tipping Point for the Era of Real-Time Radiation Therapy? *International Journal of Radiation Oncology*Biology*Physics* **102,** 922–931 (2018).
10. Moskalenko, M. *et al.* Fiducial Markers Allow Accurate and Reproducible Delivery of Liver Stereotactic Body Radiation Therapy. *Current Oncology* **30,** 5054–5061 (2023).
11. Gerlach, S. *et al.* Robotic ultrasound-guided SBRT of the prostate: feasibility with respect to plan quality. *International Journal of Computer Assisted Radiology and Surgery* **12,** 149–159 (2017).
12. Da Silva Mendes, V. *et al.* ExacTrac Dynamic workflow evaluation: Combined surface optical/thermal imaging and X-ray positioning. *Journal of Applied Clinical Medical Physics* **23,** e13754 (2022).

13. Ikushima, H. *et al.* Daily Alignment Results of In-Room Computed Tomography–Guided Stereotactic Body Radiation Therapy for Lung Cancer. *International Journal of Radiation Oncology*Biology*Physics* **79,** 473–480 (2011).
14. Lee, A. *et al.* CT-guided online adaptive stereotactic body radiotherapy for pancreas ductal adenocarcinoma: Dosimetric and initial clinical experience. *Clinical and Translational Radiation Oncology* **48,** 100813 (2024).
15. Nierer, L. *et al.* Dosimetric benefit of MR-guided online adaptive radiotherapy in different tumor entities: liver, lung, abdominal lymph nodes, pancreas and prostate. *Radiation Oncology* **17,** 53 (2022).
16. Rinck, P. A. A short history of magnetic resonance imaging. *Spectroscopy Europe* **20,** 7–10 (2008).
17. Das, I. J., Yadav, P. & Mittal, B. B. Emergence of MR-Linac in Radiation Oncology: Successes and Challenges of Riding on the MRgRT Bandwagon. *Journal of Clinical Medicine* **11** (2022).
18. Baliyan, V., Das, C. J., Sharma, R. & Gupta, A. K. Diffusion weighted imaging: Technique and applications. *World Journal of Radiology* **8,** 785 (2016).
19. Kim, J.-h. *et al.* Comparison of 1.5 T and 3T 1H MR spectroscopy for human brain tumors. *Korean Journal of Radiology* **7,** 156–161 (2006).
20. Fain, S. B. *et al.* Functional lung imaging using hyperpolarized gas MRI. *Journal of Magnetic Resonance Imaging* **25,** 910–923 (2007).
21. Serai, S. D. Basics of magnetic resonance imaging and quantitative parameters T1, T2, T2*, T1rho and diffusion-weighted imaging. *Pediatric Radiology* **52,** 217–227 (2022).
22. Biederer, J *et al.* MRI of the lung (2/3). Why... when... how? *Insights into Imaging* **3,** 355–371 (2012).
23. Buzan, M. T. *et al.* T2 mapping of CT remodelling patterns in interstitial lung disease. *European Radiology* **25,** 3167–74 (2015).
24. Buzan, M. T. A. *et al.* Texture analysis using proton density and T2 relaxation in patients with histological usual interstitial pneumonia (UIP) or nonspecific interstitial pneumonia (NSIP). *PLoS One* **12,** 1–11 (2017).
25. Benlala, I. *et al.* Quantification of MRI T2 Interstitial Lung Disease Signal-Intensity Volume in Idiopathic Pulmonary Fibrosis: A Pilot Study. *Journal of Magnetic Resonance Imaging* **53,** 1500–1507 (2021).
26. Kay, F. U. & Madhuranthakam, A. J. MR Perfusion Imaging of the Lung. *Magnetic Resonance Imaging Clinics of North America* **32.** MR Perfusion, 111–123 (2024).
27. Haage, P. *et al.* Feasibility of pulmonary ventilation visualization with aerosolized magnetic resonance contrast media. *Investigative Radiology* **40,** 85–88 (2005).
28. Edelman, R. R., Hatabu, H., Tadamura, E., Li, W. & Prasad, P. V. Noninvasive assessment of regional ventilation in the human lung using oxygen–enhanced magnetic resonance imaging. *Nature Medicine* **2,** 1236–1239 (1996).

29. Rudnick, M. R., Wahba, I. M., Leonberg-Yoo, A. K., Miskulin, D. & Litt, H. I. Risks and options with gadolinium-based contrast agents in patients with CKD: a review. *American Journal of Kidney Diseases* **77,** 517–528 (2021).
30. Bauman, G. *et al.* Non-contrast-enhanced perfusion and ventilation assessment of the human lung by means of fourier decomposition in proton MRI. *Magnetic Resonance in Medicine* **62,** 656–664 (2009).
31. Bondesson, D. *et al.* Nonuniform Fourier-decomposition MRI for ventilation- and perfusion-weighted imaging of the lung. *Magnetic Resonance in Medicine* **82,** 1312–1321 (2019).
32. Voskrebenzev, A. *et al.* Feasibility of quantitative regional ventilation and perfusion mapping with phase-resolved functional lung (PREFUL) MRI in healthy volunteers and COPD, CTEPH, and CF patients. *Magnetic Resonance in Medicine* **79,** 2306–2314 (2018).
33. Fischer, A. *et al.* SElf-gated Non-Contrast-Enhanced FUnctional Lung imaging (SENCEFUL) using a quasi-random fast low-angle shot (FLASH) sequence and proton MRI. *NMR in Biomedicine* **27,** 907–917 (2014).
34. Zapke, M. *et al.* Magnetic resonance lung function–a breakthrough for lung imaging and functional assessment? A phantom study and clinical trial. *Respiratory Research* **7,** 1–9 (2006).
35. Rabe, M. *et al.* Repeatability quantification of brain diffusion-weighted imaging for future clinical implementation at a low-field MR-linac. *Radiation Oncology* **19,** 31 (2024).
36. Kooreman, E. S. *et al.* Feasibility and accuracy of quantitative imaging on a 1.5 T MR-linear accelerator. *Radiotherapy and Oncology* **133,** 156–162 (2019).
37. Maziero, D. *et al.* Implementation and evaluation of a dynamic contrast-enhanced MR perfusion protocol for glioblastoma using a 0.35 T MRI-Linac system. *Physica Medica* **119,** 103316 (2024).
38. Kooreman, E. S. *et al.* T1ρ for Radiotherapy Treatment Response Monitoring in Rectal Cancer Patients: A Pilot Study. *Journal of Clinical Medicine* **11** (2022).
39. Dubec, M. J. *et al.* First-in-human technique translation of oxygen-enhanced MRI to an MR Linac system in patients with head and neck cancer. *Radiotherapy and Oncology* **183,** 109592 (2023).
40. van der Heide, U. A., Houweling, A. C., Groenendaal, G., Beets-Tan, R. G. & Lambin, P. Functional MRI for radiotherapy dose painting. *Magnetic Resonance Imaging* **30.** Quantitative Imaging in Cancer, 1216–1223 (2012).
41. Jones, K. M. *et al.* Emerging Magnetic Resonance Imaging Technologies for Radiation Therapy Planning and Response Assessment. *International Journal of Radiation Oncology*Biology*Physics* **101,** 1046–1056 (2018).
42. Wong, K. L., Cheng, K. H., Lam, S. K., Liu, C. & Cai, J. Review of functional magnetic resonance imaging in the assessment of nasopharyngeal carcinoma treatment response. *Precision Radiation Oncology* **6,** 177–185 (2022).

43. Kang, H., Kwak, Y., Kim, M. & Lee, S. Application of real-time MRI-guided linear accelerator in stereotactic ablative body radiotherapy for non-small cell lung cancer: one step forward to precise targeting. *Journal of Cancer Research and Clinical Oncology* **148,** 3215–3223 (2022).
44. Vinogradskiy, Y. *et al.* Use of 4-Dimensional Computed Tomography-Based Ventilation Imaging to Correlate Lung Dose and Function With Clinical Outcomes. *International Journal of Radiation Oncology*Biology*Physics* **86,** 366–371 (2013).
45. Lucia, F. *et al.* Prediction of Acute Radiation-Induced Lung Toxicity After Stereotactic Body Radiation Therapy Using Dose-Volume Parameters From Functional Mapping on Gallium 68 Perfusion Positron Emission Tomography/Computed Tomography. *International Journal of Radiation Oncology *Biology*Physics* **118,** 952–962 (2024).
46. Dhami, G. *et al.* Framework for radiation pneumonitis risk stratification based on anatomic and perfused lung dosimetry. *Strahlentherapie und Onkologie: Organ der Deutschen Rontgengesellschaft...[et al]* **193,** 410 (2017).
47. Faught, A. M. *et al.* Evaluating which dose-function metrics are most critical for functional-guided radiation therapy. *International Journal of Radiation Oncology*Biology*Physics* **99,** 202–209 (2017).
48. Siva, S. *et al.* Ventilation/Perfusion Positron Emission Tomography—Based Assessment of Radiation Injury to Lung. *International Journal of Radiation Oncology*Biology*Physics* **93,** 408–417 (2015).
49. Lee, H. J. *et al.* Correlation of Functional Lung Heterogeneity and Dosimetry to Radiation Pneumonitis using Perfusion SPECT/CT and FDG PET/CT Imaging. *International Journal of Radiation Oncology*Biology*Physics* **102.** Imaging in Radiation Oncology, 1255–1264 (2018).
50. Bille, J. & Schlegel, W. *Medizinische Physik 1: Grundlagen* (Springer Berlin Heidelberg, 1999).
51. Brown, R., Cheng, Y., Haacke, E., Thompson, M. & Venkatesan, R. *Magnetic Resonance Imaging: Physical Principles and Sequence Design* (Wiley, 2014).
52. Levitt, M. H. *Spin dynamics: Basics of nuclear magnetic resonance* (John Wiley & Sons, 2001).
53. Schlegel, W., Karger, C., Jäkel, O. & Bachert, P. *Medizinische Physik. Grundlagen - Bildgebung - Therapie - Technik* (Springer Spektrum, 2018).
54. Koutcher, J. A. & Burt, C. T. Principles of Nuclear Magnetic Resonance. *Journal of Nuclear Medicine* **25,** 101–111 (1984).
55. Hanson, L. G. Is quantum mechanics necessary for understanding magnetic resonance? *Concepts in Magnetic Resonance Part A* **32A,** 329–340 (2008).
56. Bloch, F. Nuclear Induction. *Physical Review* **70,** 460–474 (7-8 1946).
57. Goldman, M. Formal theory of spin–lattice relaxation. *Journal of Magnetic Resonance* **149,** 160–187 (2001).

58. Chavhan, G. B., Babyn, P. S., Thomas, B., Shroff, M. M. & Haacke, E. M. Principles, Techniques, and Applications of T2*-based MR Imaging and Its Special Applications. *RadioGraphics* **29,** 1433–1449 (2009).
59. Hahn, E. L. Spin Echoes. *Physical Reviews* **80,** 580–594 (4 1950).
60. Hennig, J. Echoes—how to generate, recognize, use or avoid them in MR-imaging sequences. Part I: Fundamental and not so fundamental properties of spin echoes. *Concepts in Magnetic Resonance* **3,** 125–143 (1991).
61. Elster, A. D. Gradient-echo MR imaging: techniques and acronyms. *Radiology* **186,** 1–8 (1993).
62. Bernstein, M., King, K. & Zhou, X. *Handbook of MRI Pulse Sequences* (Elsevier Inc., 2004).
63. Akcakaya, M., Doneva, M. I. & Prieto, C. *Magnetic Resonance Image Reconstruction: Theory, Methods and Applications* (Academic Press, 2022).
64. Hansen, M. S. & Kellman, P. Image reconstruction: An overview for clinicians. *Journal of Magnetic Resonance Imaging* **41,** 573–585 (2015).
65. Jung, B. A. & Weigel, M. Spin echo magnetic resonance imaging. *Journal of Magnetic Resonance Imaging* **37,** 805–817 (2013).
66. Hutchinson, J. M. S., Sutherland, R. J. & Mallard, J. R. NMR imaging: image recovery under magnetic fields with large non-uniformities. *Journal of Physics E Scientific Instruments* **11,** 217–222 (1978).
67. Jacobs, M. A., Ibrahim, T. S. & Ouwerkerk, R. MR Imaging: Brief Overview and Emerging Applications. *RadioGraphics* **27,** 1213–1229 (2007).
68. Markl, M. & Leupold, J. Gradient echo imaging. *Journal of Magnetic Resonance Imaging* **35,** 1274–1289 (2012).
69. McRobbie, D. W., Moore, E. A., Graves, M. J. & Prince, M. R. *MRI from Picture to Proton* (Cambridge University Press, 2017).
70. Bieri, O. & Scheffler, K. Fundamentals of balanced steady state free precession MRI. *Journal of Magnetic Resonance Imaging* **38,** 2–11 (2013).
71. Chavhan, G. B., Babyn, P. S., Jankharia, B. G., Cheng, H.-L. M. & Shroff, M. M. Steady-State MR Imaging Sequences: Physics, Classification, and Clinical Applications. *RadioGraphics* **28,** 1147–1160 (2008).
72. Semelka, R. C., Kelekis, N. L., Thomasson, D., Brown, M. A. & Laub, G. A. HASTE MR imaging: Description of technique and preliminary results in the abdomen. *Journal of Magnetic Resonance Imaging* **6,** 698–699 (1996).
73. Jo, Y. *et al.* Guidelines for Cardiovascular Magnetic Resonance Imaging from Korean Society of Cardiovascular Imaging (KOSCI)-Part 1: Standardized Protocol. *Investigative Magnetic Resonance Imaging* **23,** 296–315 (2019).
74. Lujan, A. E., Larsen, E. W., Balter, J. M. & Ten Haken, R. K. A method for incorporating organ motion due to breathing into 3D dose calculations. *Medical Physics* **26,** 715–720 (1999).
75. Wehrli, F. W. Time-of-flight effects in MR imaging of flow. *Magnetic Resonance in Medicine* **14,** 187–193 (1990).

76. Lin, I., Tai, L. & Fan, S. Breathing at a rate of 5.5 breaths per minute with equal inhalation-to-exhalation ratio increases heart rate variability. *International Journal of Psychophysiology* **91,** 206–211 (2014).
77. Avram, R. *et al.* Real-world heart rate norms in the Health eHeart study. *npj Digital Medicine* **2** (2019).
78. Müller, M. *Fundamentals of Music Processing: Audio, Analysis, Algorithms, Applications* (Springer Publishing Company, Incorporated, 2015).
79. Wang, C., Ren, W.-X., Wang, Z.-C. & Zhu, H.-P. Instantaneous frequency identification of time-varying structures by continuous wavelet transform. *Engineering Structures* **52,** 17–25 (2013).
80. Jiang, Q. & Suter, B. W. Instantaneous frequency estimation based on synchrosqueezing wavelet transform. *Signal Processing* **138,** 167–181 (2017).
81. Alzola-Aldamizetxebarria, S., Fernández-Méndez, L., Padro, D., Ruíz-Cabello, J. & Ramos-Cabrer, P. A Comprehensive Introduction to Magnetic Resonance Imaging Relaxometry and Contrast Agents. *ACS Omega* **7,** 36905–36917 (2022).
82. Ghaderi, N. *et al.* A Century of Fractionated Radiotherapy: How Mathematical Oncology Can Break the Rules. *International Journal of Molecular Sciences* **23** (2022).
83. Dale, R., Plataniotis, G. & Jones, B. A generalised method for calculating repopulation-corrected tumour EQD2 values in a wide range of clinical situations, including interrupted treatments. *Physica Medica* **118,** 103294 (2024).
84. Taylor, A & Powell, M. Intensity-modulated radiotherapy—what is it? *Cancer Imaging* **4,** 68 (2004).
85. Elith, C., Dempsey, S. E., Findlay, N. & Warren-Forward, H. M. An Introduction to the Intensity-modulated Radiation Therapy (IMRT) Techniques, Tomotherapy, and VMAT. *Journal of Medical Imaging and Radiation Sciences* **42,** 37–43 (2011).
86. Tsang, M. W. K. Stereotactic body radiotherapy: current strategies and future development. *Journal of Thoracic Disease* **8** (2016).
87. Green, O. L., Henke, L. E. & Hugo, G. D. Practical Clinical Workflows for Online and Offline Adaptive Radiation Therapy. *Seminars in Radiation Oncology* **29,** 219–227 (2019).
88. Brown, A. M., Mak, R. H. & Kann, B. H. Advances in stereotactic body radiation therapy for early stage non-small cell lung cancer. *Current Challenges in Thoracic Surgery* **4** (2021).
89. Guckenberger, M. *et al.* ESTRO ACROP consensus guideline on implementation and practice of stereotactic body radiotherapy for peripherally located early stage non-small cell lung cancer. *Radiotherapy and Oncology* **124,** 11–17 (2017).
90. Yan, M. *et al.* Stereotactic body radiotherapy for Ultra-Central lung Tumors: A systematic review and Meta-Analysis and International Stereotactic Radiosurgery Society practice guidelines. *Lung Cancer* **182,** 107281 (2023).

91. Zarębska, I. & Harat, M. An optimal dose-fractionation for stereotactic body radiotherapy in peripherally, centrally and ultracentrally located early-stage non-small lung cancer. *Thoracic Cancer* **14,** 2813–2820 (2023).
92. Kong, F.-M. S. *et al.* Organs at Risk Considerations for Thoracic Stereotactic Body Radiation Therapy: What Is Safe for Lung Parenchyma? *International Journal of Radiation Oncology*Biology*Physics* **110,** 172–187 (2021).
93. Bellec, J, Arab-Ceschia, F, Castelli, J, Lafond, C & Chajon, E. ITV versus mid-ventilation for treatment planning in lung SBRT: a comparison of target coverage and PTV adequacy by using in-treatment 4D cone beam CT. *Radiation Oncology* **15,** 1–10 (2020).
94. Kaidar-Person, O. & Chen, R. *Hypofractionated and Stereotactic Radiation Therapy: A Practical Guide* (Springer Nature, 2024).
95. Caillet, V., Booth, J. T. & Keall, P. IGRT and motion management during lung SBRT delivery. *Physica Medica* **44,** 113–122 (2017).
96. Gough, J. *et al.* Institutional experience of using active breathing control for paediatric and teenage patients receiving thoraco-abdominal radiotherapy. *Clinical and Translational Radiation Oncology* **39,** 100575 (2023).
97. Otazo, R. *et al.* MRI-guided Radiation Therapy: An Emerging Paradigm in Adaptive Radiation Oncology. *Radiology* **298,** 248–260 (2021).
98. Mutic, S. & Dempsey, J. F. The ViewRay System: Magnetic Resonance–Guided and Controlled Radiotherapy. *Seminars in Radiation Oncology* **24.** Magnetic Resonance Imaging in Radiation Oncology, 196–199 (2014).
99. Klüter, S. Technical design and concept of a 0.35 T MR-Linac. *Clinical and Translational Radiation Oncology* **18,** 98–101 (2019).
100. Wen, N. *et al.* Evaluation of a magnetic resonance guided linear accelerator for stereotactic radiosurgery treatment. *Radiotherapy and Oncology* **127,** 460–466 (2018).
101. Bauman, G., Lee, N. G., Tian, Y., Bieri, O. & Nayak, K. S. Submillimeter lung MRI at 0.55 T using balanced steady-state free precession with half-radial dual-echo readout (bSTAR). *Magnetic Resonance in Medicine* **90,** 1949–1957 (2023).
102. Wild, J. M. *et al.* MRI of the lung (1/3): methods. *Insights into Imaging* **3,** 345–353 (2012).
103. Tian, Y. & Nayak, K. S. New clinical opportunities of low-field MRI: heart, lung, body, and musculoskeletal. *Magnetic Resonance Materials in Physics, Biology and Medicine* **37,** 1–14 (2024).
104. Rashid, S. *et al.* Cardiac balanced steady-state free precession MRI at 0.35 T: a comparison study with 1.5 T. *Quantitative Imaging in Medicine and Surgery* **8,** 627 (2018).
105. Shahzad, K. & Mati, W. *Advances in Medical and Surgical Engineering* 121–142 (Academic Press, 2020).
106. Panych, L. P. & Madore, B. The physics of MRI safety. *Journal of Magnetic Resonance Imaging* **47,** 28–43 (2018).

107. Scheffler, K. & Lehnhardt, S. Principles and applications of balanced SSFP techniques. *European Radiology* **13,** 2409–2418 (2003).
108. Yuan, J. *et al.* A narrative review of MRI acquisition for MR-guided-radiotherapy in prostate cancer. *Quantitative Imaging in Medicine and Surgery* **12,** 1585 (2022).
109. Arroyo-Hernández, M. *et al.* Radiation-induced lung injury: current evidence. *BMC Pulmonary Medicine* **21,** 1–12 (2021).
110. Käsmann, L. *et al.* Radiation-induced lung toxicity–cellular and molecular mechanisms of pathogenesis, management, and literature review. *Radiation Oncology* **15,** 1–16 (2020).
111. Finazzi, T. *et al.* Clinical Outcomes of Stereotactic MR-Guided Adaptive Radiation Therapy for High-Risk Lung Tumors. *International Journal of Radiation Oncology*Biology*Physics* **107,** 270–278 (2020).
112. Jain, V. & Berman, A. T. Radiation Pneumonitis: Old Problem, New Tricks. *Cancers* **10** (2018).
113. Voruganti Maddali, I. S. *et al.* Optimal management of radiation pneumonitis: Findings of an international Delphi consensus study. *Lung Cancer* **192,** 107822 (2024).
114. Strange, T. A. *et al.* Spectrum of Imaging Patterns of Lung Cancer following Radiation Therapy. *Diagnostics* **13** (2023).
115. Zhao, J. *et al.* Simple Factors Associated With Radiation-Induced Lung Toxicity After Stereotactic Body Radiation Therapy of the Thorax: A Pooled Analysis of 88 Studies. *International Journal of Radiation Oncology*Biology*Physics* **95,** 1357–1366 (2016).
116. Lind, P. A. *et al.* Receiver operating characteristic curves to assess predictors of radiation-induced symptomatic lung injury. *International Journal of Radiation Oncology*Biology*Physics* **54,** 340–347 (2002).
117. Saito, G. *et al.* Real-world survey of pneumonitis and its impact on durvalumab consolidation therapy in patients with non-small cell lung cancer who received chemoradiotherapy after durvalumab approval (HOPE-005/CRIMSON). *Lung Cancer* **161,** 86–93 (2021).
118. Wang, D. *et al.* Functional dosimetric metrics for predicting radiation-induced lung injury in non-small cell lung cancer patients treated with chemoradiotherapy. *Radiation Oncology* **7,** 1–9 (2012).
119. Gayed, I. *et al.* Lung perfusion imaging can risk stratify lung cancer patients for the development of pulmonary complications after chemoradiation. *Journal of Thoracic Oncology* **3,** 858–864 (2008).
120. Bucknell, N. W. *et al.* Functional lung imaging in radiation therapy for lung cancer: A systematic review and meta-analysis. *Radiotherapy and Oncology* **129,** 196–208 (2018).
121. Midroni, J. *et al.* Incorporation of Functional Lung Imaging Into Radiation Therapy Planning in Patients With Lung Cancer: A Systematic Review and

Meta-Analysis. *International Journal of Radiation Oncology*Biology*Physics* **120,** 370–408 (2024).
122. Marks, L. B. *et al.* The role of three dimensional functional lung imaging in radiation treatment planning: The functional dose-volume histogram. *International Journal of Radiation Oncology*Biology*Physics* **33,** 65–75 (1995).
123. O'Reilly, S. *et al.* Dose to Highly Functional Ventilation Zones Improves Prediction of Radiation Pneumonitis for Proton and Photon Lung Cancer Radiation Therapy. *International Journal of Radiation Oncology*Biology*Physics* **107,** 79–87 (2020).
124. Owen, D. R. *et al.* Investigating the SPECT Dose-Function Metrics Associated With Radiation-Induced Lung Toxicity Risk in Patients With Non-small Cell Lung Cancer Undergoing Radiation Therapy. *Advances in Radiation Oncology* **6,** 100666 (2021).
125. Vinogradskiy, Y. *et al.* Use of weekly 4DCT-based ventilation maps to quantify changes in lung function for patients undergoing radiation therapy. *Medical Physics* **39,** 289–298 (2012).
126. Castillo, E. *et al.* Robust CT ventilation from the integral formulation of the Jacobian. *Medical Physics* **46,** 2115–2125 (2019).
127. Liu, J. *et al.* Image Registration in Medical Robotics and Intelligent Systems: Fundamentals and Applications. *Advanced Intelligent Systems* **1** (2019).
128. Chen, M., Tustison, N. J., Jena, R. & Gee, J. C. in *Machine Learning for Brain Disorders* 435–458 (Springer US, 2023).
129. Maintz, J. B. A. & Viergever. *An Overview of Medical Image Registration Methods* in (1998).
130. Sotiras, A., Davatzikos, C. & Paragios, N. Deformable Medical Image Registration: A Survey. *IEEE Transactions on Medical Imaging* **32,** 1153–1190 (2013).
131. Rueckert, D. in *Medical Image Registration* 281–302 (CRC Press, 2001).
132. Shackleford, J., Kandasamy, N. & Sharp, G. in *High Performance Deformable Image Registration Algorithms for Manycore Processors* 13–43 (Morgan Kaufmann, 2013).
133. Lu, X., Zhang, S., Su, H. & Chen, Y. Mutual information-based multimodal image registration using a novel joint histogram estimation. *Computerized Medical Imaging and Graphics* **32,** 202–209 (2008).
134. Shah, K. D., Shackleford, J. A., Kandasamy, N. & Sharp, G. C. A generalized framework for analytic regularization of uniform cubic B-spline displacement fields. *Biomedical Physics & Engineering Express* **7,** 045011 (2021).
135. Rueckert, D., Aljabar, P., Heckemann, R. A., Hajnal, J. V. & Hammers, A. *Diffeomorphic Registration Using B-Splines* in *Medical Image Computing and Computer-Assisted Intervention – MICCAI 2006* (Springer Berlin Heidelberg, 2006), 702–709.
136. Avants, B. B. *et al.* A reproducible evaluation of ANTs similarity metric performance in brain image registration. *NeuroImage* **54,** 2033–2044 (2011).

137. Wang, J. *et al.* Associations between MSE and SSIM as cost functions in linear decomposition with application to bit allocation for sparse coding. *Neurocomputing* **422,** 139–149 (2021).
138. Fawcett, T. An introduction to ROC analysis. *Pattern Recognition Letters* **27.** ROC Analysis in Pattern Recognition, 861–874 (2006).
139. Youden, W. J. Index for rating diagnostic tests. *Cancer* **3,** 32–35 (1950).
140. Steyerberg, E. W. *et al.* Internal validation of predictive models: Efficiency of some procedures for logistic regression analysis. *Journal of Clinical Epidemiology* **54,** 774–781 (2001).
141. Bickel, P. J. & Freedman, D. A. Some Asymptotic Theory for the Bootstrap. *The Annals of Statistics* **9,** 1196–1217 (1981).
142. Efron, B. Bootstrap Methods: Another Look at the Jackknife. *The Annals of Statistics* **7,** 1–26 (1979).
143. Steyerberg, E. W. & Harrell, F. E. Prediction models need appropriate internal, internal–external, and external validation. *Journal of Clinical Epidemiology* **69,** 245–247 (2016).
144. Wang, Z., Wang, E. & Zhu, Y. Image segmentation evaluation: a survey of methods. **53,** 5637–5674 (2020).
145. Taha, A. A. & Hanbury, A. Metrics for evaluating 3D medical image segmentation: analysis, selection, and tool. *BMC Medical Imaging* **15,** 1–28 (2015).
146. Powers, D. M. Evaluation: from precision, recall and F-measure to ROC, informedness, markedness and correlation. *arXiv preprint arXiv:2010.16061* (2020).
147. Benlala, I. *et al.* Quantification of MRI T2-weighted High Signal Volume in Cystic Fibrosis: A Pilot Study. *Radiology* **294,** 186–196 (2020).
148. Shioya, S. *et al.* Tissue characterization of pneumonia and irradiated rat lungs with magnetic resonance relaxation times. *Magnetic Resonance Imaging* **12,** 799–803 (1994).
149. Ogasawara, N., Suga, K., Karino, Y. & Matsunaga, N. Perfusion characteristics of radiation-injured lung on Gd-DTPA-enhanced dynamic magnetic resonance imaging. *Investigative radiology* **37,** 448–457 (2002).
150. NCI. *National Cancer Institute Common Terminology Criteria for Adverse Events (CTCAE), Version 5.0* https://ctep.cancer.gov. Accessed: March 6, 2024.
151. Sharp, G. C. *et al. Plastimatch: an open source software suite for radiotherapy image processing* in *Proceedings of the XVI'th International Conference on the use of Computers in Radiotherapy (ICCR), Amsterdam, Netherlands* (2010).
152. Farr, K. P. *et al.* Loss of lung function after chemo-radiotherapy for NSCLC measured by perfusion SPECT/CT: Correlation with radiation dose and clinical morbidity. *Acta Oncologica* **54,** 1350–1354 (2015).
153. Scheenstra, A. E. *et al.* Local dose–effect relations for lung perfusion post stereotactic body radiotherapy. *Radiotherapy and Oncology* **107,** 398–402 (2013).

154. Zhang, J. *et al.* Radiation-Induced Reductions in Regional Lung Perfusion: 0.1–12 Year Data From a Prospective Clinical Study. *International Journal of Radiation Oncology*Biology*Physics* **76,** 425–432 (2010).
155. Mayo, J., McKay, A & Müller, N. *T2 relaxation time in MR imaging of normal and abnormal lung parenchyma* in *Seventy sixth scientific assembly and annual meeting of the Radiological Society of North America* (1990).
156. Ronden, M., Palma, D., Slotman, B., Senan, S. & Advanced Radiation Technology Committee of the International Association for the Study of Lung Cancer. Brief Report on Radiological Changes following Stereotactic Ablative Radiotherapy (SABR) for Early-Stage Lung Tumors: A Pictorial Essay. *Journal of Thoracic Oncology* **13,** 855–862 (2018).
157. Ruopp, M. D., Perkins, N. J., Whitcomb, B. W. & Schisterman, E. F. Youden Index and Optimal Cut-Point Estimated from Observations Affected by a Lower Limit of Detection. *Biometrical Journal* **50,** 419–430 (2008).
158. Dournes, G. *et al.* 3D ultrashort echo time MRI of the lung using stack-of-spirals and spherical k-Space coverages: Evaluation in healthy volunteers and parenchymal diseases. *Journal of Magnetic Resonance Imaging* **48,** 1489–1497 (2018).
159. David, M. *et al.* Longitudinal Evaluation of Bronchial Changes in Cystic Fibrosis Patients Undergoing Elexacaftor/Tezacaftor/Ivacaftor Therapy Using Lung MRI With Ultrashort Echo-Times. *Journal of Magnetic Resonance Imaging* **60,** 116–124 (2024).
160. Lutsik, N. *et al.* MRI Relaxometry for Glioblastoma Response Assessment during Radiation Therapy on a 0.35 T MRI Linear Accelerator. *International Journal of Radiation Oncology*Biology*Physics* **120.** ASTRO 2024: 66th Annual Meeting, e254 (2024).
161. Lin, X. *et al.* Free-breathing and instantaneous abdominal T2 mapping via single-shot multiple overlapping-echo acquisition and deep learning reconstruction. *European Radiology* **33,** 4938–4948 (2023).
162. Baschnagel, A. M. *et al.* A Phase 2 Randomized Clinical Trial Evaluating 4-Dimensional Computed Tomography Ventilation-Based Functional Lung Avoidance Radiation Therapy for Non-Small Cell Lung Cancer. *International Journal of Radiation Oncology*Biology*Physics* **119,** 1393–1402 (2024).
163. Miller, R. *et al.* Characterizing Pulmonary Function Test Changes for Patients With Lung Cancer Treated on a 2-Institution, 4-Dimensional Computed Tomography-Ventilation Functional Avoidance Prospective Clinical Trial. *Advances in Radiation Oncology* **8,** 101133 (2023).
164. Yan, Y. *et al.* Exploration of radiation-induced lung injury, from mechanism to treatment: a narrative review. *Translational Lung Cancer Research* **11** (2022).
165. Faria, S., Aslani, M., Tafazoli, F., Souhami, L. & Freeman, C. The Challenge of Scoring Radiation-induced Lung Toxicity. *Clinical Oncology* **21,** 371–375 (2009).

166. Kouloulias, V. *et al.* Suggestion for a new grading scale for radiation induced pneumonitis based on radiological findings of computerized tomography: correlation with clinical and radiotherapeutic parameters in lung cancer patients. *Asian Pacific Journal of Cancer Prevention* **14,** 2717–2722 (2013).
167. Torre-Bouscoulet, L. *et al.* Longitudinal Evaluation of Lung Function in Patients With Advanced Non-Small Cell Lung Cancer Treated With Concurrent Chemoradiation Therapy. *International Journal of Radiation Oncology*Biology *Physics* **101,** 910–918 (2018).
168. Kohno, N. *et al.* Circulating Antigen KL-6 and Lactate Dehydrogenase for Monitoring Irradiated Patients with Lung Cancer. *Chest* **102,** 117–122 (1992).
169. Rades, D. *et al.* Early Identification of Pneumonitis in Patients Irradiated for Lung Cancer—Final Results of the PARALUC Trial. *Cancers* **15** (2023).
170. Usuda, K. *et al.* Diffusion-weighted magnetic resonance imaging is useful for the response evaluation of chemotherapy and/or radiotherapy to recurrent lesions of lung cancer. *Translational Oncology* **12,** 699–704 (2019).
171. Bustin, A., Witschey, W. R., van Heeswijk, R. B., Cochet, H. & Stuber, M. Magnetic resonance myocardial T1ρ mapping: Technical overview, challenges, emerging developments, and clinical applications. *Journal of Cardiovascular Magnetic Resonance* **25,** 34 (2023).
172. Ribeiro, M. F. *et al.* Deep learning based automatic segmentation of organs-at-risk for 0.35 T MRgRT of lung tumors. *Radiation Oncology* **18,** 135 (2023).
173. Lombardo, E. *et al.* Offline and online LSTM networks for respiratory motion prediction in MR-guided radiotherapy. *Physics in Medicine & Biology* **67,** 095006 (2022).

List of Figures

List of Tables

Acknowledgements

This thesis wouldn't have come together without the help and support of so many people. I am very grateful to all of you!
First and foremost, I want to thank Prof. Guillaume Landry for not only stepping in as official supervisor of my thesis, but for including me in his group and for the constant support and guidance throughout these slightly more than 3 years. I am deeply thankful for all the meetings and scientific discussions and I strongly benefited from the structured supervision. Thank you also for making it possible for me to work with the MR-Linac at the interface of radiation oncology and radiology. This is a fascinating research field and I'm very glad that I got the chance to do my PhD in this specific area.
Prof. Julien Dinkel, thank you for hiring me and being such a great PI. I have always felt inspired after our meetings and I truly envy you for your intrinsic understanding of MRI sequences. Thank you for your trust and support and of course for allowing me to attend conferences and workshops all over the world.
A huge thank you goes to PD Dr. Christopher Kurz for the great supervision, scientific discussions, all the help with the TOSCA (and PUMA) study and all the hours you spent proofreading my thesis as well as all these abstracts and paper drafts. Thank you also for your support during one of the scariest moments at the MR-Linac....
I'm also truly thankful to Dr. Moritz Rabe, who, apart from all the scientific help and supervision, also served as a mentor and role model especially during the downs along the way.
I feel very lucky for having not only one but four exceptional supervisors during my PhD journey. Thank you all for believing in me, your kindness, commitment and all the valuable advice. I have learned so much from you and I'm running out of words to express my gratitude.
I would also like to thank everyone involved in the TOSCA study: Prof. Claus Belka for allowing me to work at the MR-Linac, Prof. Stefanie Corradini for the administration of the TOSCA study especially in ethics and financial questions and Dr. Sebastian Marschner, Dr. Dinah Konnerth, Dr. Annemarie Zinn and Dr. Svenja Hering for the medical support. A special thanks goes to Dr. Chukwuka Eze for not only taking care of all the organizational work with patient scheduling etc., but for

being my go to contact person for all lung radiotherapy related questions. I'm also deeply indebted to the MR-Linac team: Dominika Dinkel, Christina Walchhofer, Patrick Thum, Laura Lang, Anne Kolberg and Sabrina Rieder. The TOSCA study wouldn't have been possible without your support, flexibility and understanding. I would also like to thank the radiology MTA team involved in the follow-up scanning and also Dr. Kaltra Begaj for the medical support.
Over the past few years I had the pleasure of working with many great people. Thank you Dr. Thomas Gaass for your guidance and advice at the beginning of my PhD journey and even after you left academia. Dr. Ilyes Benlala, thank you for initiating and organizing my research stay in Bordeaux. I really enjoyed working with you during your stay in Munich and I'm happy that we will continue this great collaboration in the future. I also want to express my deep gratitude to Prof. Olaf Dietrich for not only allowing me to work in an office with him, but also for kindly answering all my questions. I feel very lucky that I had the chance to learn from such an MRI expert.
Many thanks go to former and present members of the radiation oncology research group and especially to: Elia Lombardo, Yuqing Xiong, Maria Kawula, Ivy Chan, Dr. Henning Schmitz, Dr. Adrian Thummerer, Nikolaos Delopoulos and Lili Huang. Thank you for all your help and for the great time we had during various conferences and group activities.
One of my personal highlights during my PhD was my stay in Bordeaux where I had the opportunity to learn a lot about sequence programming. I'm extremely grateful to the LMU-Bordeaux Research Cooperation Program for funding the stay and to Prof. Aurélien Bustin and his SMHEART team for the supervision and this great experience. I'm looking forward to continuing our collaboration.
I would like to send my sincere thanks to the German Center for Lung Research (DZL) for funding this thesis and providing such a great environment for lung research. Thank you also to Dr. Enrico Schulz and Dr. Julia Ruat for the exceptional project management.
Lastly, on a personal note, I want to thank my family and friends for all the support throughout my studies. Andi, thank you for all the advice and believing in me. Sandra Resch, I'm deeply thankful for our great friendship and that we had the opportunity to walk this road together. You are a true friend and I cannot express how much this means to me. Michaela, thank you for the encouragement, the understanding and for always having a sympathetic ear. A massive thank you also goes to Christine Schönlau for all the help over all these years.
And last but not least, I want to thank my parents. I could not have done this without your love, support and guidance. I will never be able to pay you back for what you have done for me over all these years and I'm running out of words to thank you.
Mama, you have always been my biggest fan - this one is for you.